Novel Broadband Light Sources and Pulse Generation Techniques at 1.5 μm

by

Hanfei M. Shen

B.S.E, Nuclear Engineering and Radiological Sciences
University of Michigan, 2000

S.M., Electrical Engineering and Computer Science
Massachusetts Institute of Technology, 2003

Submitted to the Department of Electrical Engineering and Computer Sciences
in partial fulfillment of the requirements for the degree of

Doctor of Philosophy

at the

MASSACHUSETTS INSTITUTE OF TECHNOLOGY

September 2009

Signature of Author.....
Department of Electrical Engineering and Computer Science
August 28, 2009

Certified by.....
Erich P. Ippen
Elihu Thomson Professor of Electrical Engineering
Professor of Physics
Thesis Supervisor

Accepted by.....
Terry P. Orlando
Chairman, Department Committee on Graduate Students
Department of Electrical Engineering and Computer Science

Studies of Novel Broadband Light Sources and Pulse Generation Techniques at 1.5 μm

by

Hanfei M. Shen

Submitted to the Department of Electrical Engineering and Computer Science
on August 28, 2009 in partial fulfillment of the requirements for
the Degree of Doctor of Philosophy

ABSTRACT

A wide diversity of applications, in both fundamental science and practical technology, has come to rely on broadband optical light sources as key enabling tools. In this thesis, we investigate three devices that contribute to the generation of broadband light at 1.5 μm. The first two fall into the same broader class of saturable absorber mirrors – one device was developed for low-repetition-rate sub-100-fs ultrafast lasers and the other for high-repetition-rate femtosecond lasers. The third device bypasses generating broadband light directly from a laser altogether through the use of extra-cavity spectral broadening in a novel highly nonlinear glass fiber. In the first category, ultra-broadband saturable absorber mirrors based on III/V and Si material systems were developed for ultrafast lasers. The III/V-based mirrors were designed, fabricated, characterized and implemented in a wide range of wavelengths, spanning the visible to the near-infrared. These mirrors exhibited high-reflectivity ranges of >300 nm. Implementation of these mirrors in Ti:sapphire, Cr^{4+}:forsterite, Cr^{4+}:YAG, and erbium-doped bismuth-oxide lasers demonstrated self-starting and stable modelocked operation. Saturable absorber mirrors were also developed for high-repetition-rate short-cavity femtosecond lasers, with modulation depths ranging from 1.7% to 11%. Post-growth proton bombardment was used to improve recovery times, and preliminary laser testing has yielded promising results, with all structures demonstrating modelocking in an erbium-doped fiber laser. Saturable absorber mirrors with integrated dispersion compensation were also designed with 750 fs^2 of anomalous group delay dispersion at 1.5 μm. Finally, a novel highly nonlinear bismuth-oxide glass fiber was used to generate smooth, controlled supercontinuum spanning 1200 to 1800 nm. With a 2-cm length and a grating pair for dispersion compensation, compression of 150-fs pulses down to 25-fs was also demonstrated.

Thesis Supervisor: Erich P. Ippen
Title: Elihu Thomson Professor of Electrical Engineering, Professor of Physics

ACKNOWLEDGEMENTS

Ah, the part of the thesis that everyone reads, perhaps the only part in many cases. I have always heard about the deep pleasure my predecessors have experienced when they are writing this at the end of their graduate careers here at MIT. It is a wonderfully sweet spot indeed! Well, unfortunately, given my last minute nature, I cannot enjoy this moment overly long, since I have but an hour before the submission deadline!

Foremost, I wish to thank Professor Ippen for his remarkable support, kindness and understanding. I am eternally grateful. Thank you for giving me the opportunity to pursue my graduate studies in your laboratory at the beginning; and thank you for letting me finish at this end. I have learned and grown a tremendous amount during my time in this group. My only and deepest regret is not engaging you earlier during my time here and learning more from you directly. It is a rare opportunity to have access to such a pioneer of an entire research field, and I was certainly intimidated in my first years to tread into the office and possibly say something idiotic. I can only hope to duplicate in lesser shades your classic style as a mentor and collaborator.

I am indebted as well to the other members of my graduate thesis committee – Professor Kolodziejski and Professor Kaertner. More so than many other committees I can recollect, the work presented in this thesis would not have been possible without their contribution. The saturable absorber mirrors grown by our collaborators in the Kolodziejski lab are a centerpiece in much of our progress in the last few years. Leslie's generosity in placing resources at our disposal has and will continue to be much appreciated. In addition to the hallmark contribution of dispersion compensating mirrors, Professor Kaertner's lab has rigorously tested many of the devices we have grown in their lasers. Franz has also invested many a conversation on laser and mirror designs with me, for which I am grateful.

Without the wonderful collaborators here at MIT, much of the work carried out in this thesis would not have been possible. To Gale Petrich, thank you for all your tireless work growing our mirror structures. For much of my time here, I had only experienced the growth of a 7-pair oxidized mirror. It was not until the last few months that I realized the excruciating amount of time required to grow a 22-pair AlGaAs/AlAs mirror! Thank you for all your toil. It was a great pleasure to work with Juliet Gopinath, with whom I had the greatest overlap in the Ippen lab. Her perseverance and dedication are remarkable, and set examples for all of us. To Sheila Tandon, I am indebted for all the post-growth oxidation work she put in to fabricate the wonderful broadband saturable absorber mirrors. In addition, numerous other collaborators have contributed to the work in this document, including Dan Ripin, Hideyuki Sotobayashi, Peter Rakich, Ali Motamedi, Thomas Schibli, Jungwon Kim, Hyunil Byun, and Felix Grawert.

Many thanks also to Dorothy Fleischer and Donna Gale, and from even earlier, Mary Aldridge and Cindy Kopf, for all their hard work behind the scenes that keep our group running smoothly. That said, I'm certain all the hard candies will contribute to large dental bills some time down road.

I am grateful as well for the financial support of a National Defense Science and Engineering Graduate Fellowship in my first years at MIT.

Finally, I thank my parents for all their love and support. Finally, another PhD for another generation. Thank you for giving me my space when I needed it and finally understanding my rationales... I think!

I'll end the acknowledgements on a more somber, almost philosophical, note, in contrast to the wisecrack in my SM thesis about lasers and losers. MIT has been, is and will continue to be an incredibly remarkable, wonderful and unique place. For all my jaded remarks otherwise, what a privilege it has been to work and wander among peers of such high intellectual caliber. Inevitably, this is not a luxury that is everlasting, as MIT exists in contrast to much of the rest of the world. Especially given the perspective of having worked in the "real world" for close to a year before finally locking down this document, as part of an institution that is actually revered for its leading thinking, the contrast is all the greater. MIT affords one the luxury to *think,* really think, through tough problems, and build creative and complete solutions. You are encouraged to think here at MIT. So enjoy it, while you still have the time.

TABLE OF CONTENTS

LIST OF FIGURES

Chapter 1

INTRODUCTION

1.1 MOTIVATION

A large and wide variety of applications have driven the development of ultrafast light sources over the past decade. The painful economic correction earlier in the decade notwithstanding, the telecommunications industry has been the most visible consumer of ultrafast optical technology. Driven by the ever expanding consumption of digital content, national backbones of communications providers and infrastructure developers around the world have experienced a swell in network traffic, which has been enabled by ultrafast optical components and sources. And it is expected to continue, with global IP traffic forecast to quadruple from 10 exabytes a month in 2008 to over 40 exabytes per month in 2012 [1, 2]. Despite sometimes questionable economics, such as the recent fiber-to-the-home and fiber-to-the-node buildouts in the United States by Verizon and AT&T, optical technology is undeniably helping people become more connected. As demand continues to climb in the coming years, the pursuit of faster, more efficient, more compact and more economical optical sources remains an important endeavor.

The widespread application of WDM technology in telecommunications has strongly motivated the search for ultrashort broadband light sources at 1.5 μm. Modelocked lasers with multi-gigahertz data rates are key enabling technologies for wavelength and time division multiplexed networks. Optical time division multiplexing systems using return-to-zero (RZ) formats, typically operating at 40 Gbps or greater, benefit greatly from the

availability of simple, compact, transform-limited optical pulse sources. The still-in-development next-generation 100 Gbps Ethernet standard might also benefit from these lasers. Data streams encoded on a laser pulse train with a modulator need only the state between two successive pulses to be changed. This approach reduces the highly stringent demands on the slopes of the modulator, as the pulse shaping is already accomplished by the laser source.

In the wavelength domain, modelocked lasers generate a stable comb-shaped optical spectrum with equally spaced longitudinal modes. As data rates grow, and along with them the number of wavelength channels, the classical dense wavelength division multiplexing (DWDM) approach of using a separate stabilized source for each channel becomes less practical. The complexity of tuning and aligning the individual cw sources with the specific wavelength grid of the system is likely unsustainable. Alternatively, a single, high repetition rate modelocked laser can be used as a more efficient solution, since it simplifies wavelength stabilization and its broad output spectrum can be partitioned into a large number of WDM channels. Increasing the pulse repetition rate leads to wider channel spacing, and this often relaxes the demands on the filter characteristics of the channel add/drop nodes, allowing for higher channel capacities. In addition, the coherence of modelocked lasers can be used to increase the channel information capacity by techniques such as those used in CDMA networks. Even higher bit rates per channel can be achieved by time multiplexing the short transform-limited pulses generated in each of the spectrally sliced channels.

The application of optical arbitrary waveform generation (OAWG), in particular, has become a focus of our work at MIT. An OAWG independently encodes and decodes via amplitude and phase modulation all the individual frequency components of an oscillator at a high rate to generate arbitrary waveforms [3, 4]. It takes advantage of many of the same properties so highly valued for telecommunications applications – the extreme bandwidth of frequency lines, the relatively large spacing between said comb lines, and the coherence of the source, to name the key characteristics. Building a stable, compact, high-repetition rate modelocked laser that would be suitable for OAWG is quite challenging and needs to overcome significant headwinds. When successful, optical arbitrary waveform generation promises to have an impact both in fundamental optical science and in technology, opening the possibility of single-shot precision spectroscopy, sub-diffraction-limited imaging, and high-performance lidar, as well as ultra-wideband low-probability-of-intercept spread-spectrum lightwave communications.

In addition to the headline application of optical communications and our focus on OAWG, a number of other disciplines and applications have come to rely on pulsed lasers as a vital tool. These range from the very fundamental, such as studies of extreme nonlinear optics in novel materials and systems, to the every practical, such as biomedical imaging. In recent years, a newly developed field, frequency metrology, has also become increasingly important [5, 6, 7]. On the practical side, the presence of water absorption lines near 1.5 μm makes ultrafast optics especially interesting for biological applications. The spectral bandwidth that accompanies ultrashort pulses creates new opportunities for optical coherence tomography (OCT), enabling unprecedented ultrahigh depth resolution on the sub-micron scale [8]. In addition, the high peak powers associated with short pulse durations enable the use of femtosecond lasers for nonlinear spectroscopic techniques, such as bio-imaging via higher harmonic generation [9, 10] and coherent anti-Stokes Raman scattering [11]. In all, it is a long list of applications for which broadband light is sought after, including time-resolved spectroscopy [12], high-harmonic generation [13], laser-driven particle accelerators [14], x-ray lasers [15], coherent control of chemical dynamics [16], optical data storage [17], and terahertz generation and imaging [18].

1.2 THESIS OUTLINE

As can be seen, the application of ultrashort broadband light sources has rapidly become widespread over the past decade. However, the utility of ultrafast lasers for many commercial applications is still limited by their ease of use, reliability, bulkiness, and high cost, necessitating novel approaches to developing stable, turnkey and inexpensive ultrashort broadband light sources. To that end, a variety of optical light sources and devices at 1.5 μm have been investigated in this thesis for the purposes of improving the aforementioned characteristics.

Chapters 2 and 3 explore the design and use of saturable absorber mirrors in ultrafast lasers. Saturable absorbers play an important role in initiating, controlling and stabilizing modelocking. In addition, they simplify and relax otherwise stringent cavity design parameters for stable laser operation. Chapter 2 focuses specifically on absorber mirrors designed for broadband operation, that is, for lasers trying to achieve the shortest possible pulse widths. After a brief review of the basic operating principles of saturable absorber mirrors in Section 2.2, we present work on oxidized large-area ultra-broadband semiconductor saturable absorber mirrors in Section 2.3, that have been designed and

implemented in a number of wavelength regimes, ranging from the near-infrared to the visible. The design, fabrication, characterization and laser implementation of these devices are discussed. A novel silicon-based ultra-broadband saturable absorber mirror is the subject of Section 2.4.

Chapter 3 moves the spotlight to absorber mirrors for operation in short-cavity high-repetition rate lasers. Section 3.2 discusses, at a high level, the particular design requirements unique to high repetition rate systems, with Sections 3.3, 3.4 and 3.5 being drilldowns on specific design parameters. Section 3.3 discusses the use of resonant coating layers to enhance the modulation depth of absorber mirrors. Section 3.4 looks at proton bombardment to reduce the recovery time of absorbers. Section 3.5 considers novel mirror designs integrating dispersion compensation with saturable absorption.

Finally, we switch gears in Chapter 4 and consider an alternative broadband light source to ultrafast lasers – supercontinuum generation. Short lengths of a novel highly nonlinear bismuth-oxide fiber are used dramatically amplify the bandwidth of coherent output from a relatively long-pulse-width seed laser. Subsequent pulse compression yielded pulse widths on par with the ultrafast laser outputs discussed in Chapter 2.

REFERENCES

1. A. Odlyzko, *Minnesota Internet Traffic Studies*, http://www.dtc.umn.edu/mints/home.php.

2. *Cisco Visual Networking Index: Global Mobile Data Traffic Forecast*, http://www.cisco.com (2009).

3. T. Yilmaz, C. M. DePriest, T. Turpin, J. H. Abeles, and P. J. Delfyett, Jr., "Toward a photonic arbitrary waveform generator using a modelocked external cavity semiconductor laser," *IEEE Photonics Technology Letters*, vol. 14, pp. 1608-10, 2002.

4. J. Chou, Y. Han, and B. Jalali, "Adaptive RF-photonic arbitrary waveform generator," *IEICE Transactions on Electronics*, vol. E86-C, pp. 1226-9, 2003.

5. D. J. Jones, S. A. Diddams, J. K. Ranka, A. Stentz, R. S. Windeler, J. L. Hall, and S. T. Cundiff, "Carrier-envelope phase control of femtosecond mode-locked lasers and direct optical frequency synthesis," Science **288**, 635 (2000).

6. B. R. Washburn, S. A. Diddams, N. R. Newbury, J. W. Nicholson, M. F. Yan, and C. G. Jorgenson, "Phase-locked, erbium-fiber-laser-based frequency comb in the near infrared," Optics Letters **29**, 250 (2004).

7. S. A. Diddams, D. J. Jones, J. Ye, S. T. Cundiff, J. L. Hall, J. K. Ranka, R. S. Windeler, R. Holzwarth, T. Udem, and T. W. Hansch, "Direct link between microwave and optical frequencies with a 300 THz femtosecond laser comb," Physical Review Letters **84**, 5102 (2000).

8. W. Drexler, U. Morgner, F. X. Kärtner, C. Pitris, S. A. Boppart, X. D. Li, E. P. Ippen and J. G. Fujimoto, "In vivo ultrahigh-resolution optical coherence tomography," Optics Letters **24**, 1221 (1999).

9. P. Campagnola, M. Wei, A. Lewis and L. Loew, "High-resolution optical imaging of live cells by second harmonic generation," Biophysical Journal **77**, 3341 (1999).

10. A. Millard, P. Wiseman, D. Fittinghoff, K. Wilson, J. Squier and M. Muller, "Third-harmonic generation microscopy by use of a compact, femtosecond fiber laser source," Applied Optics **38**, 7393 (1999).

11. A. Zumbusch, G. Holtom, and X. Xie, "Three-dimensional vibrational imaging of coherent anti-stokes Raman scattering," Physical Review Letters **82**, 4142 (1999).

12. J. Shah, *Ultrafast Spectroscopy of Semiconductors and Semiconductor Nanostructures*, Springer Series in Solid-State Sciences **115** (1996).

13. I. P. Christov, J. Zhou, J. Peatross, A. Rundquist, M. M. Murnane and H. C. Kapteyn,"Non-adiabatic effects in high-harmonic generation with ultrashort pulses," Physical Review Letters **77**, 1753 (1996).

14. D. Umstadter, S. Y. Chen, A. Maksimchuck, G. Mourou and R. Wagner, "Nonlinear optics in relativistic plasmas and laser wake field acceleration of electrons," Science **273**, 472 (1996).

15. C. P. Barty, T. Guo, C. LeBlanc, F. Raksi, C. Rose-Petruck, J. A. Squier, B. Walker, K. R. Wilson, V. V. Yakovlev and K. Yamakawa, "Sub-20-fs multiterawatt lasers," Ultrafast Phenomena Technical Digest (1996).

16. A. M. Weiner, "Femtosecond optical pulse shaping and processing," Progress in Quantum Electronics **19**, 161 (1995).

17. D. A. Akimov, A. B. Fedotov, N. I. Koroteev, E. V. Levich, S. A. Magnitskii, A. N. Naumov, D. A. Sidorov-Biryukov, N. T. Sokolyuk and A. M. Zheltikov, "Three-dimensional optical memory systems based on photochromic materials polarization control of two-color data writing and the possibility of nondestructive data reading," Optical Memory & Neural Networks **6**, 31 (1997).

18. D. M. Mittleman, R. H. Jacobsen and M. C. Nuss, "T-ray imaging," IEEE Journal of Selected Topics in Quantum Electronics **2**, 679 (1996).

Chapter 2

BROADBAND SATURABLE BRAGG REFLECTORS

2.1 INTRODUCTION

Semiconductor saturable absorbers are an important and well established technology for generating stable, self-starting pulses in solid-state lasers. These devices, known as saturable Bragg reflectors (SBR) or semiconductor saturable absorber mirrors, consist of semiconductor quantum wells or bulk absorbing layers integrated with a semiconductor mirror structure. SBRs have been very successful in modelocking a variety of solid-state lasers, covering a wide range of wavelengths in the visible and near-infrared; pulse widths from femtoseconds to nanoseconds; and power levels from milliwatts to >100 watts. For short pulse generation in particular, SBRs were used to start and stabilize ultrafast two-cycle pulses in a Ti:sapphire laser, for example [1]. In the 1.5 μm wavelength range, we demonstrated self-starting 35-fs pulses, generated directly from a Cr^{4+}:YAG laser incorporating an SBR [2].

As part of this thesis, SBRs were investigated for use in a number of femtosecond and picosecond lasers. The focus of this chapter is on broadband SBRs developed for the purpose of generating ultrashort pulses. The chapter following, Chapter 3, will explore SBRs developed for high-repetition-rate lasers. We begin in Section 2.2 with a bit of background and theory on SBRs – how they work and some broad design principles. An oxidized ultra-broadband SBR design, based on III/V-based materials, is the subject of Section 2.3. This SBR was originally designed for the 1.5 μm wavelength range and

produced the aforementioned 35-fs self-starting pulses. Subsequent improvements in the design and fabrication process led to SBRs with larger usable surface area and more favorable optical characteristics. These SBRs were then adapted and their operating wavelength range modified for implementation in a number of different laser systems, including Ti:sapphire, Cr:forsterite and bismuth-oxide erbium-doped fiber. Finally, in Section 2.4, the characterization and performance of a broadband Si-Ge SBR are discussed. This SBR design is particularly interesting due to its silicon-based material system, opening the possibility of leveraging existing integration technology and manufacturing processes for photonics applications. The device exhibited broadband reflectivity due to its high index contrast and a surprisingly fast nonlinear response.

The work presented in this chapter was a collaborative effort, a theme throughout this thesis. The work presented in Section 2.3 was the resultant output of many individuals. Throughout the effort, the mirror structures were grown in Professor Kolodziejski's lab at MIT by Gale Petrich. For the first generation SBRs, the post-growth oxidations were performed by Alexei Erchak; for the second generation, Sheila Tandon. It is primarily the latter's contributions that are discussed in this thesis. In Professor Ippen's group, Dan Ripin, Juliet Gopinath and I collaborated on the design, characterization and initial laser implementation of the SBRs. Hideyuki Sotobayashi tested the oxidized SBRs in the bismuth-oxide erbium-doped fiber laser. Demonstrations of the SBRs in the Ti:sapphire and Cr:forsterite laser systems were done by Richard Ell, Jungwon Kim and Thomas Schibli in Professor Kaertner's group. For the broadband Si-Ge SBR discussed in Section 2.4, Felix Grawert in Professor Kaertner's group drove the device design and Er:glass laser implementation. Jifeng Liu, Shoji Akiyama, and Kazumi Wada in Professor Kimerling's group at MIT fabricated the SBRs.

2.2 BACKGROUND AND THEORY

As a content note, modelocking theory will not be covered in this thesis, as it is outside the scope. Cursory, as well as in-depth reviews, of modelocking fundamentals can be found in numerous other references [3, 4, 5, 6]. However, we will provide a brief review of saturable absorbers, their application in modelocking, and device design principles in this chapter and the next.

An essential issue for real-world applications of modelocked lasers is the starting and stabilizing of pulsed operation. In general, the pulse build-up time for passively modelocked lasers takes several thousands of resonator roundtrips or more and usually lasts microseconds and longer. This can be accelerated by the use of a slow saturable absorber. With Kerr-lens modelocking, which has been the most successful technique to date in generating ultrashort pulses, modelocked operation is often not self-starting. In order to start pulse formation, a significant perturbation of cw operation may be required. KLM is often started by tapping one of the laser end mirrors by hand. With a saturable absorber mirror, the modelocking process begins with relatively long pulses. These pulses can then act as the significant perturbation needed for KLM to become effective. Once KLM takes over, the absorber becomes too slow to shape the pulses faster and the SBR functions primarily as a highly-reflecting Bragg mirror and stabilizes against instabilities [7, 8].

The use of saturable absorbers in solid-state lasers is practically as old as the solid-state laser itself [9, 10]. Initially however, it was believed that pure cw modelocking of solid-state lasers was not possible with saturable absorbers. With the advent of bandgap engineering and modern semiconductor growth technology however, it became possible to design and construct saturable absorbers with accurate control of key device parameters.

The most prevalent saturable absorber technologies today are semiconductor-based – these being saturable Bragg reflectors (SBR) [11] and semiconductor saturable absorber mirrors (SESAM) [12], both of which have been used extensively for both saturable absorber modelocking and initiation of Kerr lens modelocking. The advantages of semiconductor-based saturable absorbers are numerous: their ability to absorb light over a broad range of wavelengths, from the visible to the mid-infrared; low saturation energies; the possibility of compact design and integration, and the ability to custom engineer the absorption characteristics by altering growth parameters and device design. Specific reflectivity and dispersion profiles, the absorption wavelength, the saturation energy and the recovery time can all be tailor designed for specific applications.

2.2.1 Fundamentals of Saturable Absorbers

Fundamentally, a saturable absorber is a device that has decreasing light absorption with increasing light intensity. We need saturable absorbers to show this behavior at the intensities typically found in solid-state laser cavities, and semiconductor saturable absorbers are ideally suited for this.

A semiconductor absorbs light when the photon energy is sufficient to excite carriers from the valence band to the conduction band. Under conditions of strong excitation, the absorption is saturated because possible final states of the pump transition are depleted. Naturally, pulse formation is favored as an intensity increase passes through the absorber. High intensity signals are passed through unaffected, while low-intensity noise is absorbed and suppressed. This behavior is illustrated in Figure 2.1.

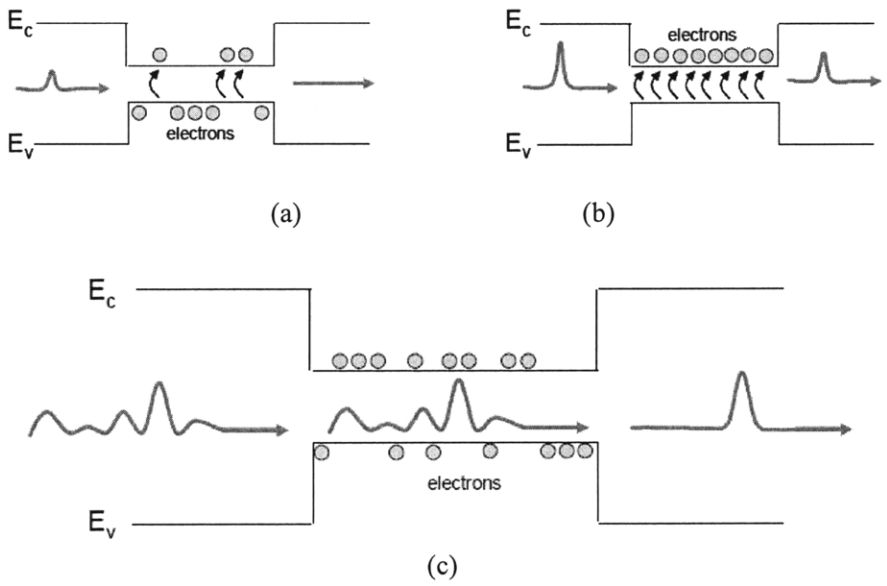

Figure 2.1 Saturable absorption illustrated with a simplified 2-level system view. (a) Incident light at low intensities is absorbed and excites carrier to the conduction band. (b) As the incident light intensity increases, the conduction band becomes saturated and no more states are available for carriers in the valence band to be excited to, leading to lower absorption. (c) With a constant stream of noise in a laser, high-intensity sections are favored and passed through unaffected, and low-intensity sections are absorbed, naturally leading to pulse formation.

Upon carrier excitation, the temporal dynamics are particularly interesting and relevant for modelocking. Semiconductor absorbers have an intrinsic bitemporal impulse response, as shown in Figure 2.2. The absorption is bleached due to band filling and then recovers with fast and slow time constants [13]. The fast time constants are due to intraband carrier-carrier scattering and thermalization processes, typically on the order of 10-100 fs and 1 ps, respectively. Interband trapping and recombination processes, typically between a few picoseconds and a few nanoseconds, lead to the slow time constant. The presence of traps can be influenced by the device growth parameters and post-growth processing.

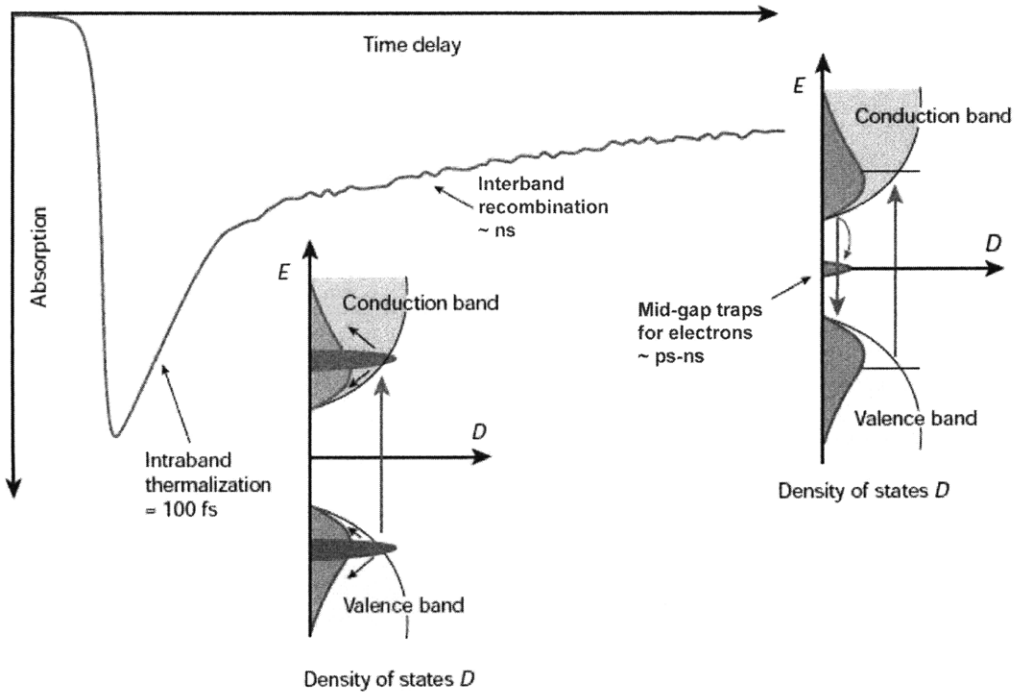

Figure 2.2 Semiconductor saturable absorber response profile. Bitemporal impulse response exhibits a fast component from intraband carrier-carrier scattering and thermalization, and a slow component due to interband trapping and recombination processes. Adapted from [12].

The presence of two different time scales proves to be rather useful for modelocking. The faster saturable absorption plays an important role in stabilizing femtosecond lasers by suppressing noise instabilities, while the slower response is important for starting the pulse formation process and for pulse forming in lasers with pulse widths of picoseconds or longer. In particular, the longer time constant results in a reduced saturation intensity for the part of the absorption that facilitates self-starting modelocking [14]. Therefore, SBRs allow us to obtain self-starting modelocking more easily.

2.2.2 KEY PARAMETERS OF SATURABLE ABSORBERS

The key parameters of a saturable absorber for laser modelocking are its modulation depth, non-saturable losses, saturation behavior, absorber recovery time, and operational bandwidth. Ease of fabrication, device damage threshold and physical configuration and

their implication on laser cavity design are additional practical considerations that need to be accounted for.

The ideal saturable absorber would have a high modulation depth; no non-saturable losses; adaptable saturation behavior that allows cw modelocking but inhibits Q-switching; a fast recovery time with respect to pulse shortening and a slow recovery time with respect to self-starting modelocking; and a large operational bandwidth with no wavelength dependency.

The modulation depth is the amount of loss of the absorber that can be bleached by a pulse of sufficient energy. A large modulation depth is desirable because, according to all modelocking theories, we find that the pulse width is typically inversely proportional to the modulation depth of the saturable absorber. The greater the modulation depth, the shorter the pulses.

Non-saturable losses, on the other hand, need to be minimized as much as possible. These generally result from material and device defects, and contribute two negative effects. They increase the lasing threshold, and reduce the lasing efficiency.

The saturation behavior of the absorber needs to designed to expected intra-cavity pulse energies. With SBRs, the saturation behavior can be adjusted by changing the incident mode area. The saturation intensity or fluence of the absorber should be sufficiently high so that the absorption is not bleached at cw intracavity intensities. If the absorber were fully bleached by the cw intensity, it would not be able to provide further absorption modulation needed to support short pulse formation. Additionally, if the saturation fluence is too low, lasers often tend to exhibit multiple pulsing. On the other hand, if the saturation fluence is too high relative to the lasers operating fluence, there is the risk of Q-switching.

Another important parameter, already discussed, is the absorber recovery time. The saturable absorber's temporal response to an excitation pulse determines the minimum achievable pulse duration and the modelocking build-up characteristics of the laser.

Finally, an ideal saturable absorber would be wavelength-independent and, in the case of SBRs, ultra-broadband. The latter characteristic is desirable given that the SBR ultimately acts as a high reflector end mirror in the laser cavity and one wants to avoid wavelength filtering by that element, which would reduce the net gain bandwidth and be detrimental for ultrashort pulse generation. The wavelength independence is desirable for the

modulation depth, the saturation behavior, and the dispersion parameters, so that one can exploit the full gain bandwidth of the laser and maximize the operational wavelength range.

Modulation depth, recovery time and dispersion will be discussed in more depth in the next chapter.

2.2.3 Basic Structure of Saturable Bragg Reflectors

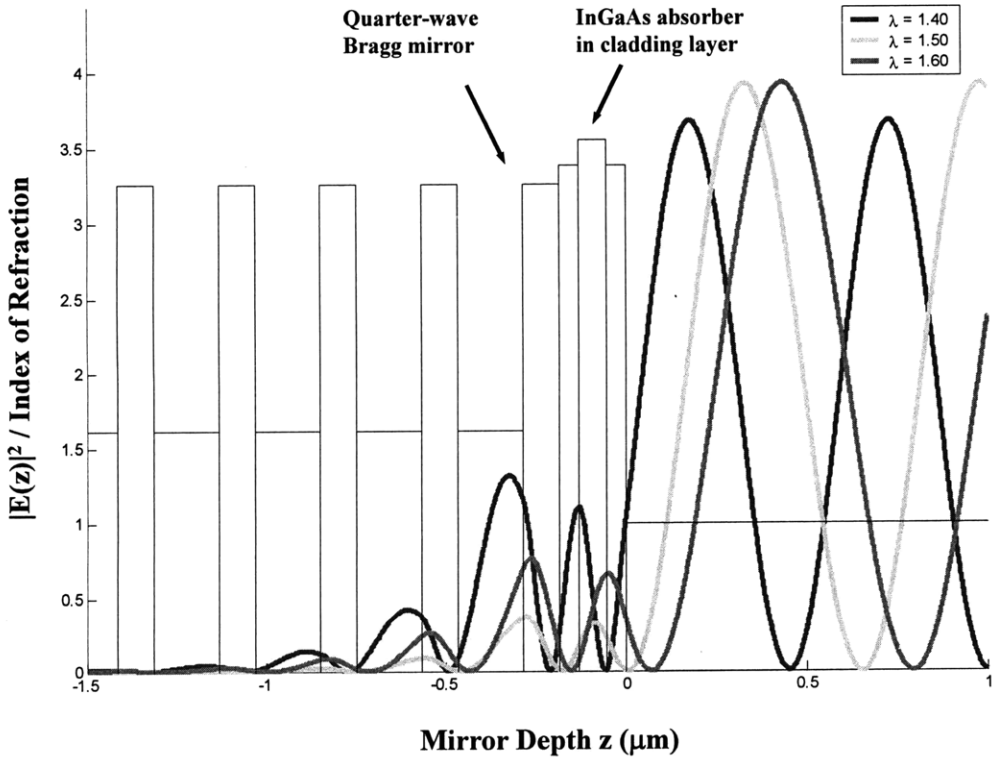

Figure 2.3 Configuration of a typical saturable Bragg reflector, consisting of a λ/2-thick absorber-cladding layer structure integrated on top of a quarter-wave Bragg stack. Index profile of the structure and the square of the electric field standing wave pattern for 3 wavelengths are shown. Light is incident from the right.

The basic structure of a saturable Bragg reflector is an epitaxially grown bulk or quantum well absorber integrated on a high-reflectivity base mirror. A sample structure is shown in

Figure 2.3. The base mirror is typically the standard Bragg mirror, with alternative high- and low-index layers of quarter-wave thickness. The absorber is placed within a cladding layer meant to minimize distortion of the electric field profile in the structure. Typically, the absorber-cladding layer section of the SBR has a total thickness of $\lambda/2$. In addition, the profiles of the square of the electric field for 3 different wavelengths are shown. The device was designed for a center wavelength of 1.5 μm, with the absorber placed at the peak of the standing wave pattern. As you can see, the longer and shorter wavelengths have different standing wave patterns in the structure, hence their resulting reflectivity, modulation depth, and dispersion will be different. As will be discussed, analysis of the electric field in SBR structures can provide considerable insight for design.

Through the choice of materials, the placement of the absorber, and additional coatings, the designer can manipulate a variety of design parameters to alter the response of the SBR. The amount and distribution of strain, which affects device recovery time, can be adjusted with the choice of mirror and absorber materials. The placement of the absorber layers in the electric field standing wave pattern affects the modulation depth and saturation fluence. Various coatings on the structures can be added to enhance reflectivity, modulation depth, and saturation fluence. Additionally, the latter two parameters can be altered by the number of quantum wells or the thickness of absorbing layers used.

2.3 Broadband Oxidized Saturable Bragg Reflectors

We have designed, fabricated and characterized a number of novel broadband oxidized III/V-based SBR structures here at MIT, in a collaborative effort with Professor Leslie Kolodziejski's group. The novelty of these structures lies in the large bandwidth of their Bragg mirrors, as well as their large surface areas. The otherwise low index contrast of GaAs/AlAs quarter-wavelength Bragg mirrors was significantly amplified through the addition of a novel steam oxidation process, which converted the AlAs layers into Al_xO_y. As a result of the higher index contrast, the high-reflectivity bandwidth expanded, allowing for the generation of shorter pulses. Continued exploration of the oxidation process resulted in larger-surface-area SBRs, which improved the ease of laser alignment and modelocking; and, subsequently, the SBR design was extended to cover a broad range of operating wavelengths. These efforts are the focus of discussion in this section.

2.3.1 First-Generation Oxidized Saturable Bragg Reflectors for the Cr^{4+}:YAG Laser

Broadband oxidized III/V SBRs were originally developed for the Cr^{4+}:YAG laser at 1.5 μm. The laser material Cr^{4+}:YAG has an emission spectrum spanning 1.2 to 1.6 μm, giving it considerable potential for sub-10-fs pulse generation. In addition, this spectral range just covers the entire low-loss window of low-water-peak optical fiber. Such wideband characteristics offer one-for-all convenience, flexibility, and simplicity to multi-band component manufacturers.

Free-space Cr^{4+}:YAG lasers had been extensively investigated previously. With the use of highly-reflective, broadband dispersion-compensating chirped mirrors (DCMs), pulses as short as 20 fs were generated directly from a Cr^{4+}:YAG laser via Kerr lens modelocking [15]. These pulses had a corresponding spectrum centered at 1450 nm, with a FWHM bandwidth of 190 nm. However, as mentioned before, KLM was not typically self-starting, and an SBR was needed to relax the otherwise precise cavity alignment conditions necessary for modelocking.

Semiconductor saturable absorber mirrors have frequently been used to overcome this difficulty and have initiated modelocking without critical alignment in several solid-state lasers [11, 12, 16]. Previously, in Cr^{4+}:YAG lasers, modelocking was demonstrated with saturable absorber mirrors consisting of InGaAs/InP [17], InGaAs/GaAs [18], and InGaAs/InAlAs [19, 20] quantum wells. In all of these devices, GaAs/AlAs quarter-wavelength Bragg stacks were used as the substrate mirror. As a consequence of the relatively low index contrast between GaAs (3.39) and AlAs (2.87), the maximum achievable bandwidth was ~150 nm, thereby limiting ultrashort pulse generation.

Zhang et al. designed a workaround solution by using a gold mirror substrate bonded with an InGaAs/InAlAs quantum well absorber [21, 22]. The broadband gold mirror reflectivity was enhanced with $SiO_2/TiO_2/SiO_2$ dielectric layers to offset some of its high intrinsic loss. With this configuration, Zhang was able to generate 44 fs pulses directly from his Cr^{4+}:YAG laser. Rather than the mirror bandwidth limiting performance in this case, higher order dispersion was ultimately the culprit.

In our alternative approach, we developed a novel oxidized high-index-contrast SBR, which resulted in 36 fs pulses generated directly from a Cr^{4+}:YAG laser [2]. The SBR started and stabilized the modelocking, and the subsequent pulses that were formed initiated Kerr lens modelocking. Such broadband oxidized mirrors had previously been

used only in VCSELs and not for generating sub-50-fs pulses. Their low intrinsic loss combined with bandwidths as large or larger than enhanced metallic mirrors made these devices quite favorable for ultrashort pulse generation.

The SBR structure is shown below in Figure 2.4. The refractive index and the electric field standing wave pattern are shown as a function of position. The SBR consisted of a 7-pair GaAs/Al_xO_y quarter-wave Bragg stack and a 10 nm InGaAs quantum well in a $\lambda/2$-thick InP cladding layer. The layer thicknesses were chosen for a center wavelength of 1440 nm, corresponding to the Cr^{4+}:YAG gain peak. The refractive indices of the GaAs and Al_xO_y layers were 3.39 and 1.61 at 1.5 μm, respectively. In comparison to AlAs with a refractive index of 2.87, the Al_xO_y layers contributed to a much greater index contrast. This large index contrast was the key to designing a mirror with only 7 layer pairs that exhibited high reflectivity over such a broad bandwidth.

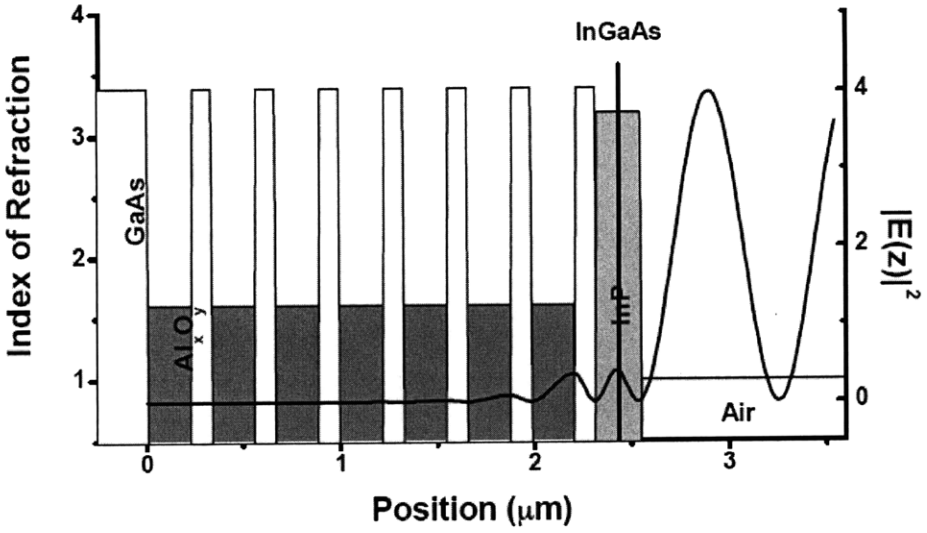

Figure 2.4 Refractive index profile (left axis) and standing wave intensity distribution (right axis) of the R885 saturable Bragg reflector structure, designed for use in the Cr^{4+}:YAG laser [2].

The impact from the high index contrast between GaAs and Al_xO_y is illustrated in Figure 2.5, which shows calculated reflectivity profiles of oxidized and un-oxidized mirror structures. The narrower bandwidth, blue dotted curve represents mirrors previously used in Cr^{4+}:YAG lasers that consisted of GaAs and AlAs. These mirrors typically contained 30

layer pairs and exhibited >99.5% reflectivity from 1380 to 1520 nm. In contrast, 7-layer-pair GaAs/Al_xO_y mirrors (solid line) have >99.5% reflectivity from ~1200 to 1850 nm – a significant disparity and improvement over their GaAs/AlAs counterparts. Additional advantages of the high index contrast are compactness with fewer layers, short epitaxial growth times, and a relaxed requirement on the thickness control. Even a ±10% thickness error can be tolerated with the bandwidth of the mirror still covering the entire Cr^{4+}:YAG gain spectrum.

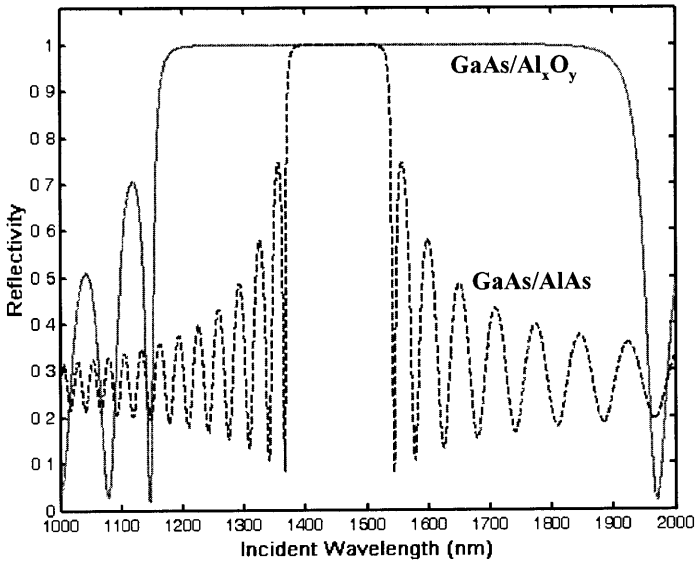

Figure 2.5 Calculated reflectivity profiles for oxidized (GaAs/Al_xO_y, solid) and un-oxidized (GaAs/AlAs, dashed) III-V-based Bragg mirrors. The effect of the higher index contrast is clearly demonstrated by the larger stopband of the oxidized mirror.

The reflectivity curves shown above were calculated using a comprehensive model built for the purpose of designing our SBR structures, as well as for comparing measured results to their intended design. The model is based on the propagation matrix formalism outlined in Kong [23]. A summary of the formalism and guiding equations is given in Appendix A. A copy of the program code is attached in Appendix B. Bulk absorption characteristics for a number of semiconductor materials, built in with complex refractive indices, are also included in the code in order to account for the different materials contained in our structures. For the purposes of comparing measured to designed reflectivity profiles, the model can also take into account the angle of incidence and polarization state, as the FTIR reflectivity measurement uses light incident at 35 degrees. Significant amounts of time were spent during the development of the oxidized SBRs discussed here and in the next

section, 2.3.1, characterizing SBRs, using the program to compare measured results to their theoretical expectations, and then iterating on improved designs and growths.

In addition to the reflectivity profile, the model also calculates the standing wave electric field patterns inside the structure, which guides the saturable absorption design of the SBR. The placement of absorbing layers can determine the modulation depth and the two photon absorption in a given structure. The exact positions and thicknesses of the absorber layers were numerically optimized using the program, especially so for the SBRs discussed in the next chapter. Altogether, the model can calculate reflectivity, dispersion, modulation depth, two-photon absorption, and the electric field distribution inside the structure.

Device Fabrication

The structure shown above in Figure 2.4 was fabricated using III-V semiconductor growth techniques. The process is summarized below in Figure 2.6. First, SBR layers were grown using gas source molecular beam epitaxy (GSMBE) on GaAs substrates. The initial layers grown on the substrate were the GaAs/AlAs Bragg mirror layers, followed by the InGaAs quantum well within an InP cladding layer. Following this growth, the AlAs layers were then converted to Al_xO_y through a wet oxidation process [24, 25]. In the wet oxidation setup depicted in Figure 2.7, nitrogen gas carried water vapor from a heated bath to the furnace tube. A cleaved SBR sample was then placed in the wet oxidation furnace at 400 °C. The oxidation process converts the high-refractive-index AlAs to low-refractive-index Al_xO_y laterally from the edge of the structure. Consequently, only material near exposed edges was oxidized, resulting in a region 200 μm wide around the outer boundary of the SBRs that could be used for laser modelocking. Un-oxidized regions had too much loss for modelocking to be a possibility.

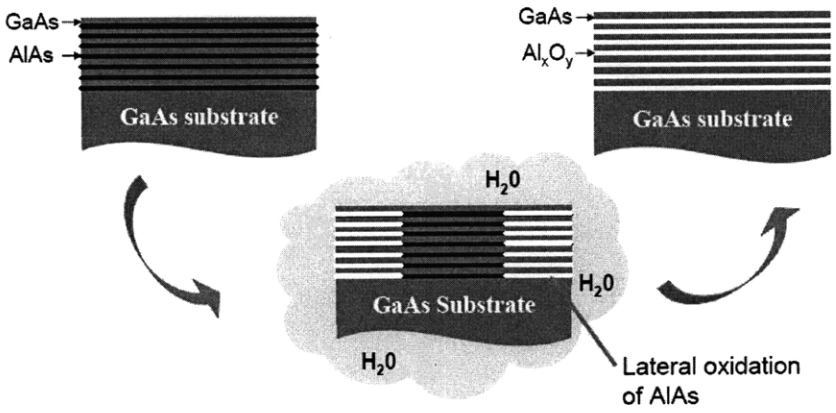

Figure 2.6 Overview of the oxidized SBR fabrication process, from the left to the right. The SBR layers are first deposited epitaxially by GSMBE. The AlAs layers are then laterally oxidized and converted into Al_xO_y.

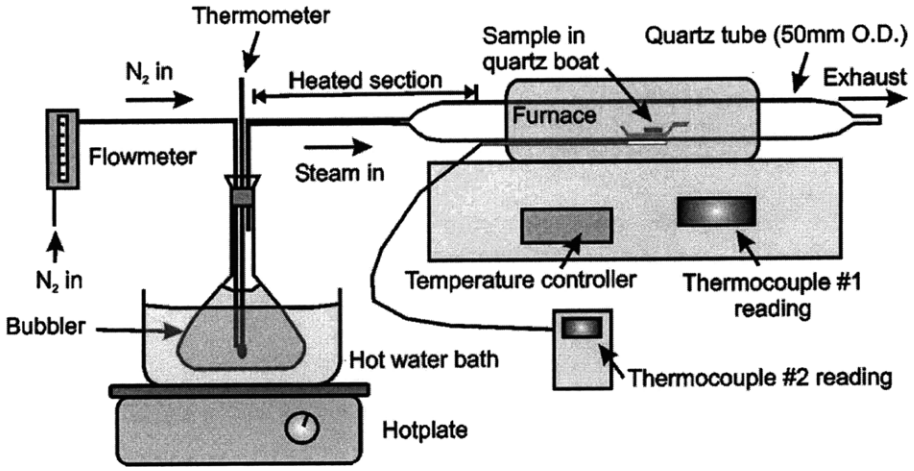

Figure 2.7 Schematic of the steam oxidation setup used to convert AlAs to lower-index Al_xO_y. The sample is located on the right side in the furnace [24]. Courtesy of A. Erchak.

Conversion of the AlAs to Al_xO_y via oxidation leads to a shrinkage in the original AlAs layer thickness of approximately 10%. As the InP/InGaAs section is not lattice-matched to the GaAs layer on which it is grown, significant strain is introduced to the interface between the absorber region and the Bragg mirror. This strain can have both beneficial and detrimental effects. On the positive side, the strain can lead to a higher number of

defects that increases the non-radiative recombination rates in the absorber. This means faster recovery times and shorter modelocked pulse widths. On the negative side, too much strain can lead to non-saturable absorber loss and, more importantly, mechanical instability of the structure. High laser pulse intensities can also exacerbate these instabilities and lead to overheating and device failure. Accordingly, consideration for strain in the structure is a major factor in the device design, and needs to be accounted for when choosing the material composition of the cladding layers around the absorber. There is a fundamental trade-off between fast recovery times and non-saturable losses with this design parameter.

In our structures, InP cladding layers distributed strain throughout the InGaAs absorber layer, while GaAs cladding layers would concentrate strain at the InGaAs interface. The 35-fs pulse width generation result discussed in this section utilized an SBR with InP cladding layers.

Device Characterization

The optical properties of the SBR were studied with several characterization techniques.

The mirror reflectivity was measured using Fourier transform infrared spectroscopy (FTIR), and is shown in Figure 2.8(a) below. In analogy to the calculated reflectivities shown earlier in Figure 2.5, Figure 2.8 also shows the measured reflectivity of an un-oxidized 22-pair GaAs/AlAs mirror to illustrate the impact of the higher index contrast. The oxidized SBR had a stopband from 1300 to 1800 nm and a maximum reflectivity of >99.2%. The band edge of the InGaAs absorber, at 1540 nm, was determined through photoluminescence of the device.

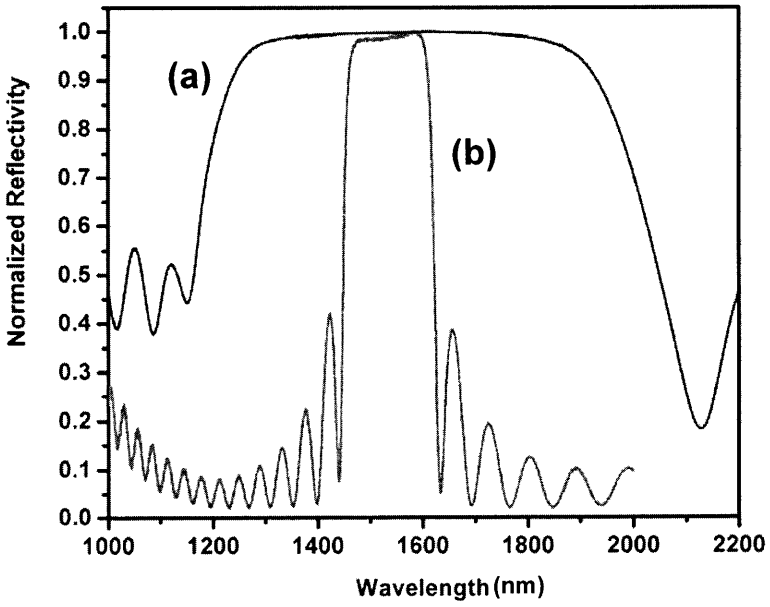

Figure 2.8 Measured reflectivity profiles of (a) an oxidized GaAs/Al_xO_y mirror and (b) an un-oxidized GaAs/AlAs mirror. Measurement counterpart to Figure 2.5.

To determine the saturation fluence and recovery time of the SBR, pump-probe spectroscopy was performed using the setup shown in Figure 2.9. The pump-probe technique reveals time-dependent responses of the SBR with a temporal resolution equal to the cross-correlation width of the pump and probe pulses. In our experiments, 110- to 150-fs pulses from a Spectra-Physics optical parametric oscillator (OPO), tunable between 1.4 and 1.6 μm, were used as the source. These pulses pass through an isolator and are then split into pump and probe paths with a beamsplitter. The pump pulses pass through a mechanical chopper, a half-wave plate and a delay stage; and are recombined with the probe pulses at a polarizing beamsplitter. An aspheric lens is used to focus the light onto a sample, and a small portion of the reflected probe light is focused onto a detector. The setup is collinear and cross-polarized, with a time resolution of approximately 150-200 fs.

Pump-probe results presented throughout this thesis were obtained by several investigators. Juliet Gopinath measured the initial SBRs used for the Cr^{4+}:YAG laser, discussed in this section. Juliet and I worked together in adjusting the experimental setup and measuring the second-generation oxidized SBRs (Section 2.3.2), as well as the Si-Ge SBRs (Section 2.4). Finally, Ali Motamedi measured the resonantly-coated and proton-bombarded SBRs discussed in Chapter 3.

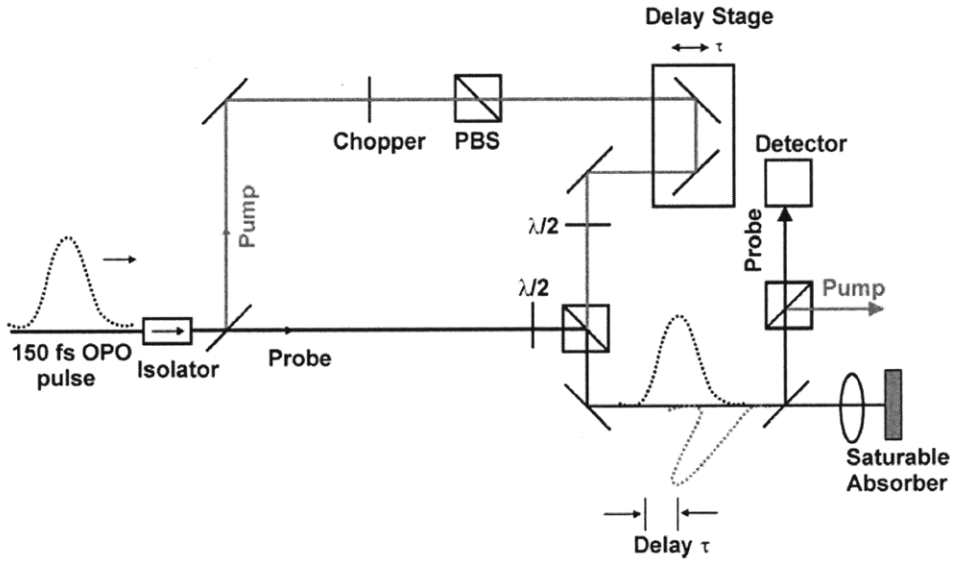

Figure 2.9 Pump-probe spectroscopy setup for SBR characterization. Courtesy of J. Gopinath.

Several pump-probe measurements for varying pump powers are shown in Figure 2.10. At low fluences, the SBR response showed a fast saturation due to intraband thermalization and a long recovery time of about 40 ps due to recombination. The saturation fluence was estimated to be on the order of ~10 $\mu J/cm^2$, and the maximum saturable loss was 0.3%. As the pump fluence was increased, significant two-photon absorption (TPA) increased the total loss of the SBR, making it an inverse saturable absorber. In general, TPA is harmful, as it ultimately limits the power of the laser pulses and adversely affects KLM action at high incident light intensities.

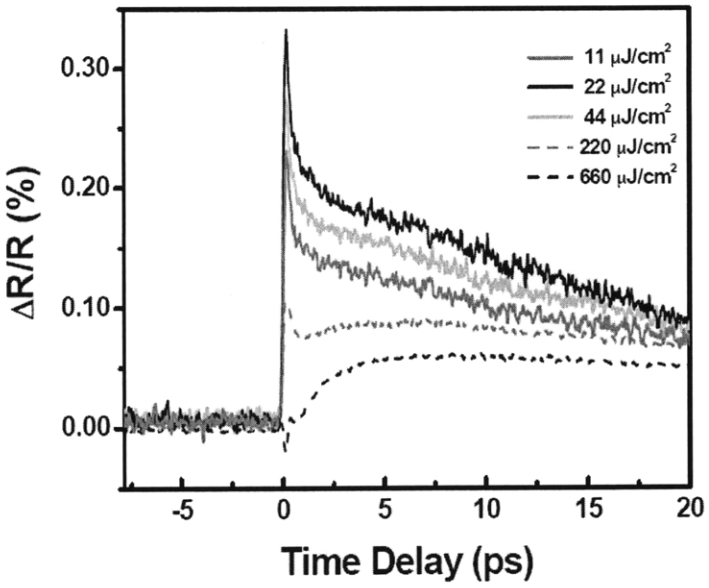

Figure 2.10 Pump-probe traces for Cr^{4+}:YAG SBR (sample R885), performed at 1540 nm at a variety of fluences [2]. Data courtesy of J. Gopinath.

Laser Results

The broadband oxidized SBR was incorporated into a z-fold Cr^{4+}:YAG laser cavity to initiate and stabilize modelocking. A schematic of the laser cavity is shown in Figure 2.11. A 2-cm Brewster-Brewster-cut Cr^{4+}:YAG laser crystal was pumped at 1064 nm by a Spectra-Physics 11-W Nd:YVO_4 laser. Light exits the cavity from the output coupler (OC), which transmits 0.7% at 1515 nm and <1.4% from 1420 to 1630 nm. Three dispersion-compensating mirrors (DCM) were used in the cavity – 2 10-cm radius-of-curvature DCMs (M1 and M2) flank the laser crystal and an additional 10-cm ROC DCM (M3) focused light onto the SBR (M4). Details of the dispersion compensation by DCMs are described in depth in [15] and [26].

By adjusting the radius of curvature of mirror M3, the spot size, and hence the fluence, on the SBR could be adjusted. In our experimental configuration, the spot size incident on the SBR was calculated to have a radius of ~50 μm. However, this degree of freedom was ultimately limited by the size of the usable SBR surface area.

Finally, the angles of incidence for all 3 mirrors needed to be taken into account to compensate the astigmatism introduced by the laser crystal and maximize the stability range of the laser. The initial cavity design did not take this into consideration and cw lasing was not optimized until subsequent correction. Mirrors M1 and M2 had angles of incidence set at 14 degrees, and M3 at 8 degrees. These values were calculated using a spatial beam profile program based on the ABCD matrix formalism, and by comparison of sagittal and tangential spot sizes in the laser crystal and at the output coupler.

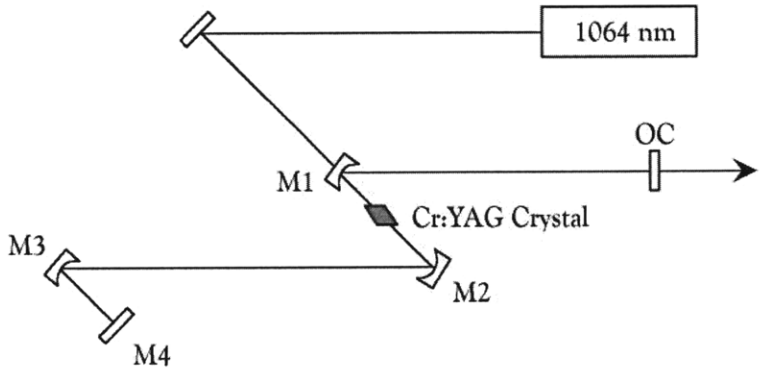

Figure 2.11 Diagram of z-fold Cr^{4+}:YAG laser incorporating the broadband oxidized SBR.

The laser had an output power of 300 mW with the SBR for 9 W of absorbed pump. No damage to the SBR was observed during modelocked operation, and performance was stable over long durations. With the SBR, modelocked operation was self-starting and the laser could be tuned from 1400 to 1525 nm with an intracavity birefringent filter. KLM operation initiated by the SBR produced pulses with a FWHM of 68 nm centered about 1490 nm. The measured modelocked spectrum is shown in Figure 2.12, together with an interferometric autocorrelation. Assuming a sech-shaped pulse yielded a pulse width of 32 fs. However, given the uncertainty of the actual pulse shape, we determined the pulse width from the Fourier transform of the measured spectrum, resulting in 35 fs.

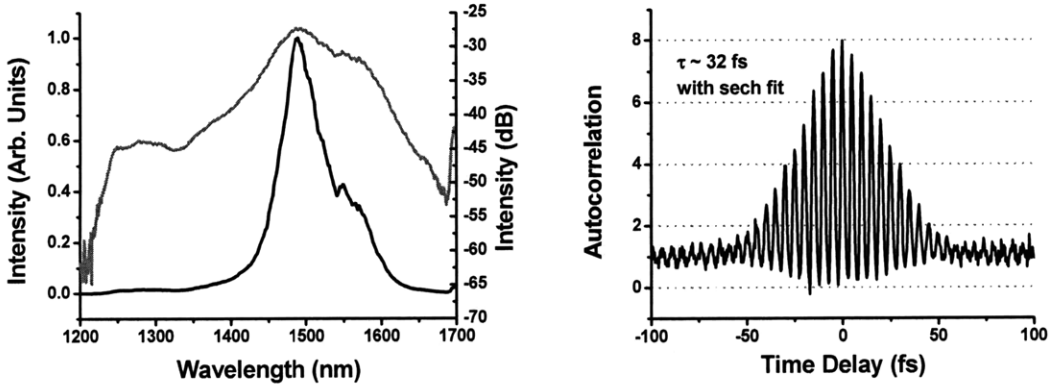

Figure 2.12 (a) Modelocked spectrum of the self-starting Cr^{4+}:YAG laser incorporating the broadband oxidized R885 SBR. (b) Interferometric autocorrelation of pulses from the self-starting Cr^{4+}:YAG laser. From [2].

A previous pure-KLM version of the Cr^{4+}:YAG laser achieved 20 fs pulses and a spectral bandwidth of 190 nm FWHM [15]. Ideally, the self-starting Cr^{4+}:YAG laser with the SBR should have equaled or even bettered that performance level. There was no fundamental reason preventing it. Ultimately, when comparing against the pump-probe measurements, it was determined that two-photon absorption (TPA) played the limiting role in the self-starting Cr^{4+}:YAG laser. Under the operating conditions of the laser, we calculated an intracavity fluence of 1 mJ/cm^2 incident on the SBR. In Figure 2.10 above, 1 mJ/cm^2 would correspond to a curve even lower than the lowest curve shown – essentially turning the SBR into an inverse saturable absorber. The challenge for the next iteration of SBR development was to mitigate the undesired TPA effect through the fabrication of larger-surface-area SBRs. A larger surface area would allow for a larger spot size incident on the SBR, which would result in reduced fluence and less TPA.

2.3.2 Next-Generation Development of Large-Area Oxidized Saturable Bragg Reflectors for Multiple Operating Wavelengths

Expanding upon the first-generation SBR development, larger-area, more mechanically stable SBRs were developed, and extended to additional operating wavelength ranges [27, 28, 29]. Improvements in the fabrication process, achieved by Sheila Tandon in Professor Kolodziejski's group, were key in progressing the implementation of this material platform to wider operating ranges and additional wavelengths.

Fabrication of SBRs with larger surface areas was enabled by three significant process design improvements by S. Tandon. First, patterning of a mesa structure through photolithography and wet etching led a larger surface area. Second, aluminum was added to the high-index GaAs layer to strengthen the bonding between layers. Third, a controlled temperature ramp was implemented. The final two initiatives targeted minimizing delamination.

For the first change, recall that the oxidation process moves laterally from the edge of the mirror sample inwards. By defining a circular mesa shape, the usable "width" was effectively doubled, compared to the rectangular surface areas before, creating a larger SBR surface area for incident light. The modified fabrication process is shown below in Figure 2.13. Mesas are defined with photolithography, and then, wet etchants are used to expose the cross section of the SBR structure for oxidation. A (1:8:40) H_2SO_4:H_2O_2:H_2O etch was used for arsenic-based SBRs and a (1:1:2) HCl:H_2NO_3:H_2O was used for InP or InGaAlP layers. Exposed layers were then laterally oxidized in the wet tube furnace as before.

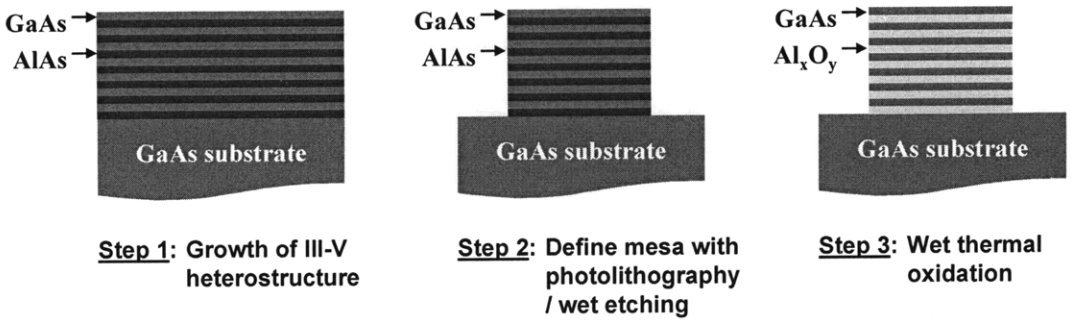

Figure 2.13 Overview of the modified oxidized SBR fabrication process, from the left to the right. The SBR layers are first deposited epitaxially by GSMBE. Mesas are then defined through photolithography and wet etching to optimize the useable surface area of the mirror. Then, finally, the AlAs layers are laterally oxidized and converted into Al_xO_y.

The introduction of mesas by themselves, however, was insufficient – delamination remained a persistent obstacle to achieving large-area SBRs. The 10% contraction of the AlAs when converted to Al_xO_y and the subsequent weak bond between GaAs and Al_xO_y still led to delaminated structures. An example of a mechanical device failure is shown in Figure 2.14. A second example is shown in Figure 2.15.

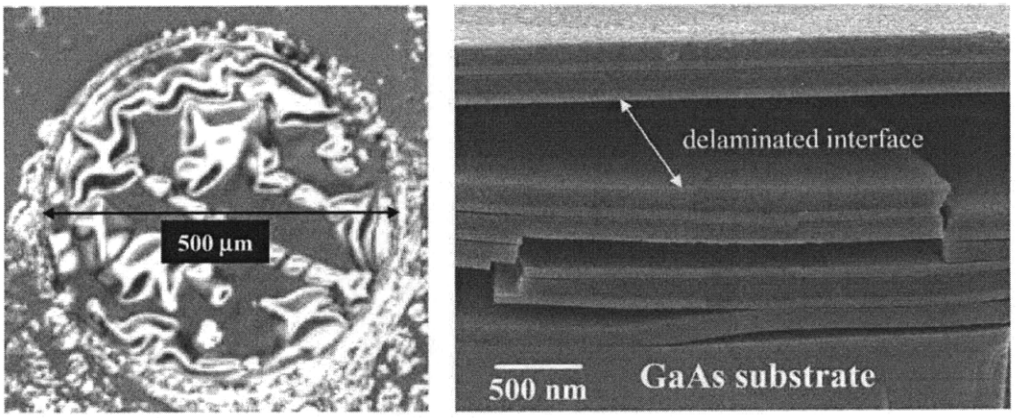

(a) (b)

Figure 2.14 (a) Top-down view of a delaminated SBR mesa structure. (b) Side cross-sectional view of a delaminated oxidized SBR [27]. Courtesy of S. Tandon.

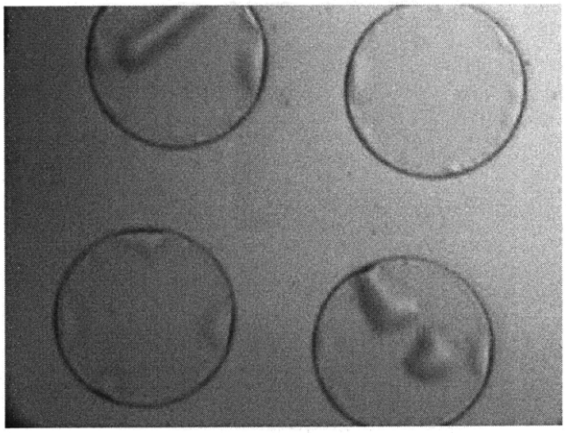

Figure 2.15 Top-down view of a delaminated SBR mesa structure. Courtesy of S. Tandon.

Low-temperature oxidation techniques could potentially stabilize the mirror layers; however, they would have also limited the extent of the oxidation progress, and hence the device dimensions. Instead, this led to the next set of process improvements. First, by replacing the high-index GaAs layers with $Al_{0.3}Ga_{0.7}As$ layers, the bond at the interface with Al_xO_y was strengthened. This greatly extended the achievable oxidation dimensions. Care had to be taken the aluminum content in the AlGaAs layer was not too high, otherwise, that layer would oxidize as well in the wet furnace process step. Second, by using a more gradual temperature ramp-up and ramp-down during the oxidation process, delamination was also reduced. This effect is illustrated in Figure 2.16. In the top panel

(a), a step change in the oxidation temperature led to delamination of the structure, as evidenced by the vertical bars in the top-down view. When a gradual change in the furnace temperature profile was implemented in (b), the result was production of stable structures.

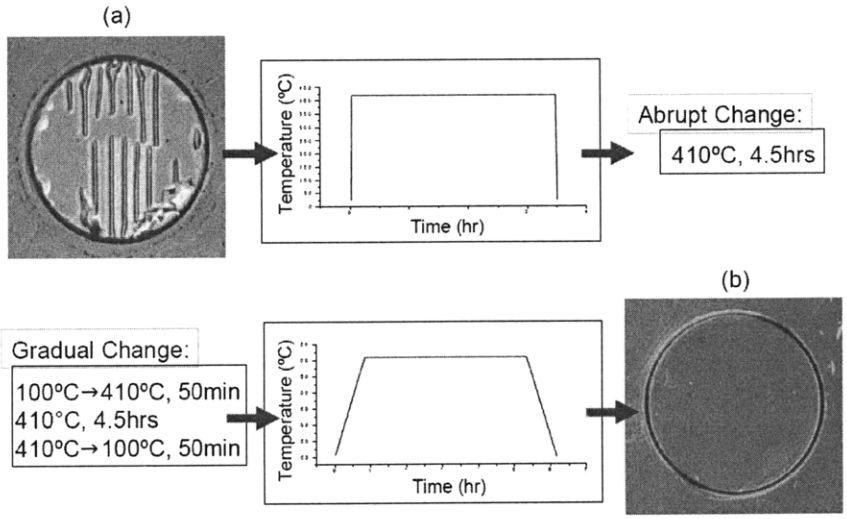

Figure 2.16 Oxidation results illustrating the effect of a gradual temperature ramp in the oxidation process. (a) Without a temperature ramp, the sudden change in temperature causes the structure to delaminate and fail. (b) With a temperature ramp, the resulting structure is stable. Courtesy of S. Tandon [28].

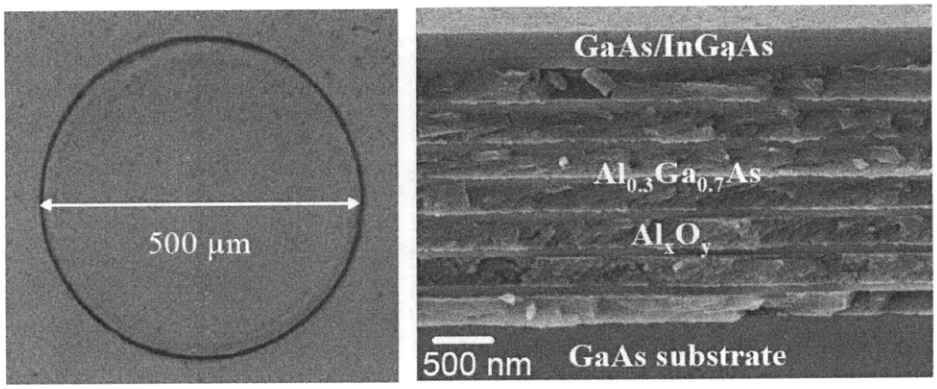

(a) (b)

Figure 2.17 (a) Top-down view of a fully oxidized 500 μm mesa of an $Al_{0.3}Ga_{0.7}As/Al_xO_y$ SBR for the Cr:forsterite laser. (b) Side cross-sectional view of the same fully-oxidized Cr:forsterite SBR [27].

With these fabrication process improvements in place – mesas to maximize oxidation area, AlGaAs rather than GaAs to reduce strain, and a gradual oxidation temperature ramp-up and ramp-down, complete oxidation of mesas of 500 μm diameter was achieved. Figure 2.17 shows top-down and side views of a fully-oxidized 500-μm-diameter SBR designed for a Cr:forsterite laser at 1300 nm. Expanding on this work, 500-μm-diameter mesas were developed for lasers operating at wavelengths spanning the visible to the near-infrared, at 800 nm, 1300 nm, and 1500 nm. Figure 2.18 demonstrates this broad span of wavelengths covered by the base design, with sample SBR reflectivity profiles for each wavelength range.

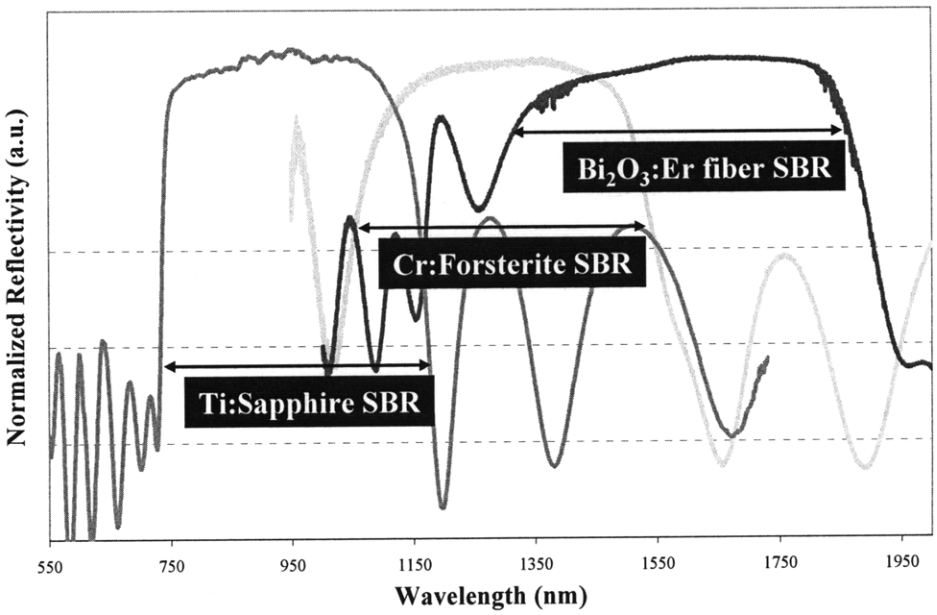

Figure 2.18 Measured reflectivity profiles of oxidized Al_xO_y-based SBRs spanning the visible to the near-infrared.

Saturable Bragg Reflectors at 1500 nm

At 1500 nm, several SBRs with different modulation depths were developed, for the Cr^{4+}:YAG laser and the erbium-doped bismuth-oxide fiber laser.

An SBR with a relatively low modulation depth was developed for the Cr^{4+}:YAG – growth number R968. The structure consisted of the 7-pair $Al_{0.3}Ga_{0.7}As/Al_xO_y$ base mirror, with quarter-wave thicknesses designed for operation at 1440 nm (111 nm / 216 nm). For

R968, a 10 nm $In_{0.5}Ga_{0.5}As$ quantum well absorber was centered in a λ/2-thick GaAs cladding layer. The R968 structure is shown in Figure 2.19, together with the electric field profile in the device. The measured reflectivity of the R968 SBR is shown in Figure 2.20.

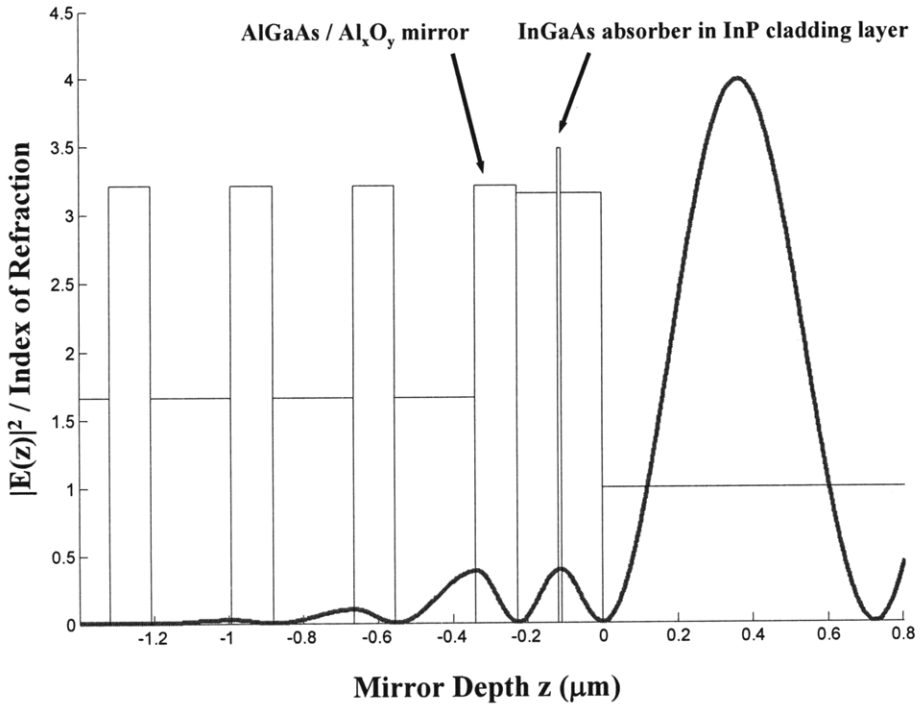

Figure 2.19 Refractive index profile and electric field standing wave pattern of the R968 SBR, designed for use in the Cr^{4+}:YAG laser.

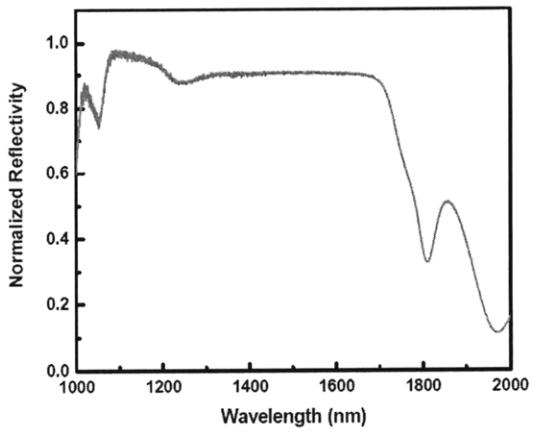

Figure 2.20 Measured reflectivity of the R968 Cr^{4+}:YAG SBR.

Pump-probe measurements of the device, performed at 1550 nm, revealed a modulation depth of 0.3% and a recovery time of 12 ps. Pump-probe traces are shown in Figure 2.21. In comparison, the original Cr^{4+}:YAG SBR discussed in Section 4.3.1 had a recovery time of 40 ps. As mentioned earlier, because of the GaAs cladding layers, strain was concentrated at the absorber interface leading to more defects and faster recombination rates. Pump-probe studies also showed the fluence behavior to be similar to the original Cr^{4+}:YAG SBR. With the greater surface area of the mesas, negative two-photon absorption effects could be avoided by de-focusing incident light to a larger spot size. The second-generation SBRs had a usable surface area of 19.6×10^4 μm^2 compared to the 3.1×10^4 μm^2 of the first-generation reflectors. In addition, the GaAs cladding layers had a lower TPA coefficient than the earlier InP material – 10 cm/GW versus 90 cm/GW. Simulations of the structures yield a TPA loss of ~0.3% for the new GaAs-cladding layer SBR and 1.7% for the older InP-based SBR.

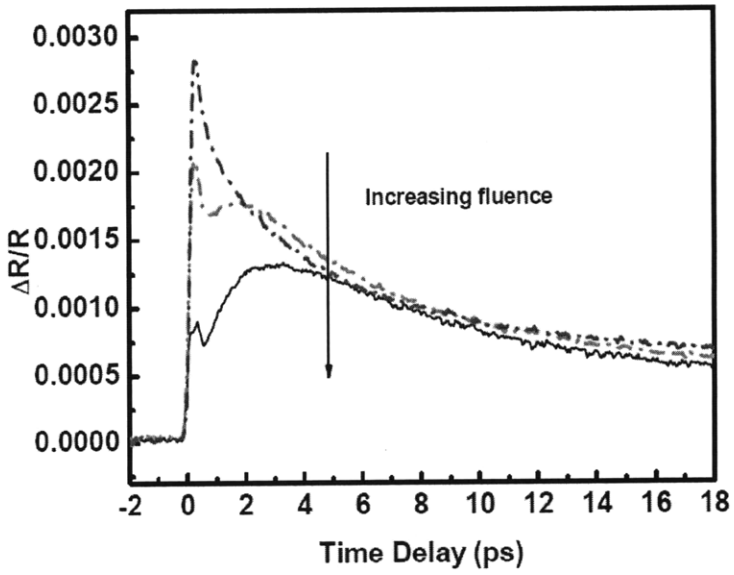

Figure 2.21 Pump-probe traces of the R968 oxidized Cr^{4+}:YAG SBR measured at 1540 nm. Data courtesy of J. Gopinath.

Unfortunately, we were not able to investigate the implementation of this SBR in a Cr^{4+}:YAG laser, as our gain crystal had degraded over time and even cw lasing was erratic. However, from its optical characterization, its potential laser performance appears promising, and the R968 design and SBR samples are an option for modelocking other broadband low-gain lasers in the 1500 nm wavelength range.

A larger modulation depth SBR was also developed at 1500 nm for a bismuth-oxide-based erbium-doped fiber laser. This structure – growth number R981 – consisted of the same 7-pair $Al_{0.3}Ga_{0.7}As/Al_xO_y$ base mirror, with thicknesses designed for a center wavelength of 1565 nm. The absorbing layers were 6 $In_{0.5}Ga_{0.5}As$ quantum wells evenly distributed near the center of a $\lambda/2$-thick InP cladding layer. The placement of the quantum wells at the center of the cladding layer maximized the overlap of the absorbers with the peak of the electric field profile. The R981 structure is shown in Figure 2.22, together with the square of the electric field inside the device. The measured reflectivity of the R968 SBR is shown in Figure 2.23, along with the theoretical design. The bandgap of the device was 1550 nm, as determined by photoluminescence measurements.

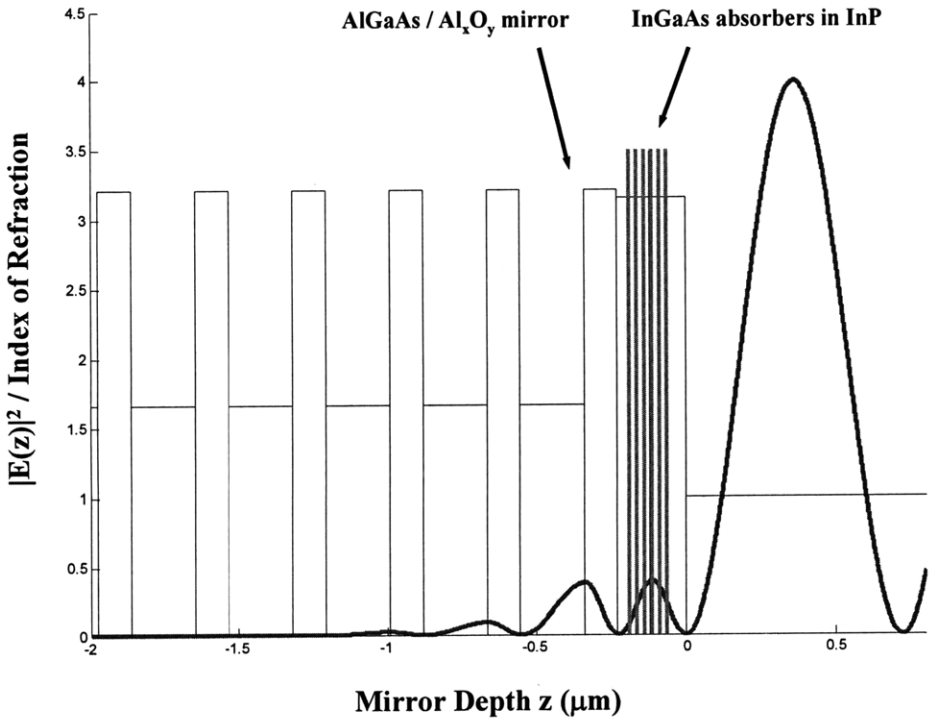

Figure 2.22 Refractive index profile and electric field standing wave pattern of the R981 SBR, designed for use in the Er-doped bismuth-oxide fiber laser.

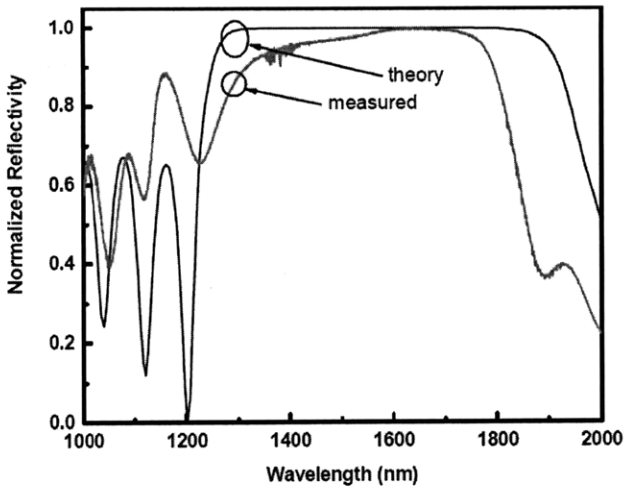

Figure 2.23 Calculated and measured reflectivity profiles of the R981 SBR for the bismuth-oxide fiber laser. The calculated reflectivity does not include absorption.

Pump-probe measurements reveal a modulation depth of 1.3% at 1540 nm and a recovery time of 40 ps. Pump-probe traces are shown in Figure 2.24.

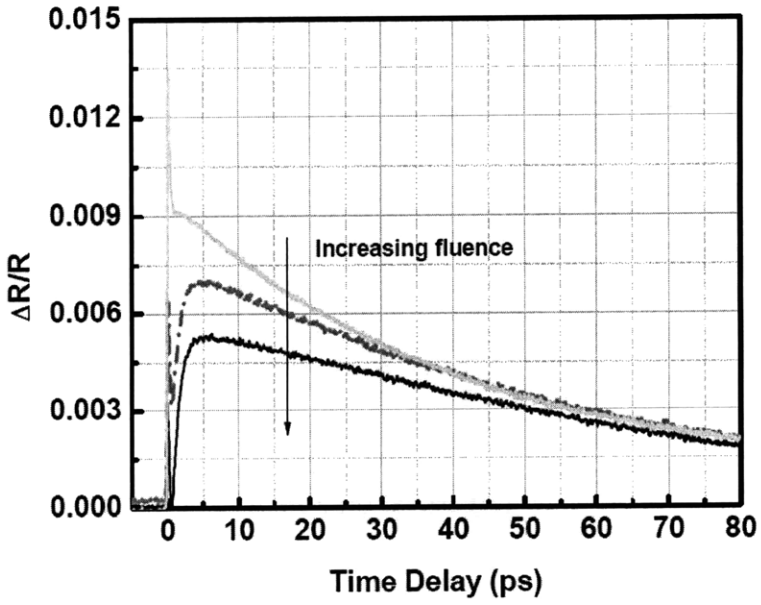

Figure 2.24 Pump-probe traces of the R981 oxidized bismuth-oxide fiber laser SBR measured at 1540 nm

The structures were subsequently anti-reflection coated with a quarter-wave-thick layer of Al_2O_3 and proton bombarded, reducing the recovery time to ~6 ps. When incorporated into the erbium-doped bismuth-oxide fiber laser, 155 fs pulses were generated [30].

Saturable Bragg Reflectors at 1300 nm

At 1300 nm, SBRs were developed for the broadband Cr:forsterite laser. With the same 7-pair $Al_{0.3}Ga_{0.7}As/Al_xO_y$ base mirror designed for a center wavelength of 1300 nm, the device contained a 40 nm $In_{0.5}Ga_{0.5}As$ absorbing layer, placed in a $\lambda/2$-thick GaAs cladding layer. The R946 structure is shown in Figure 2.25, together with the square of the electric field.

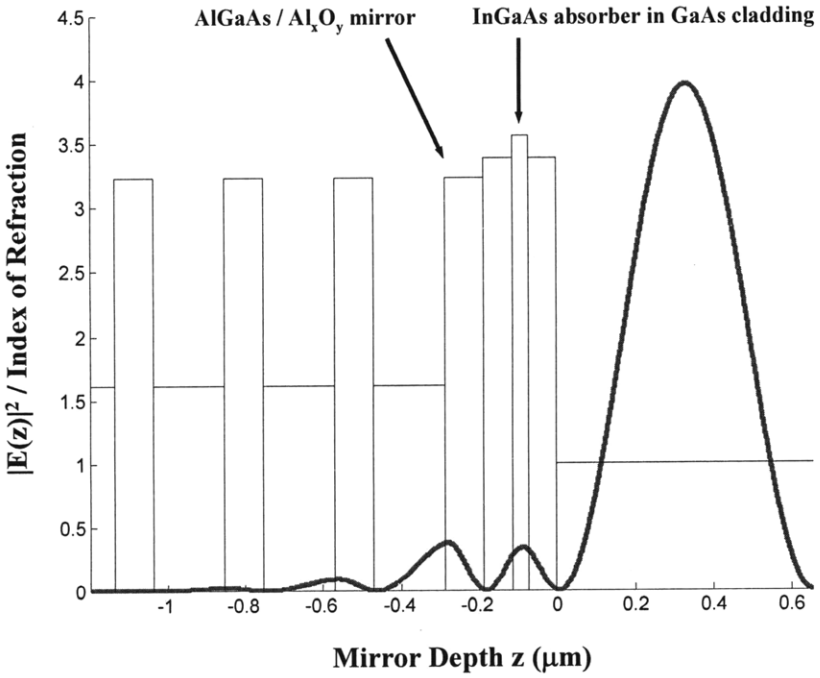

Figure 2.25 Refractive index profile and electric field standing wave pattern of the R946 SBR, designed for use in the Cr:forsterite laser.

The device demonstrated broadband reflectivity, as shown in Figure 2.26. When incorporated in a Cr:forsterite laser, self-starting 30 fs modelocked pulses were generated, for use in a frequency metrology experiment [31, 32]. The modelocked Cr:forsterite spectrum is shown together with the SBR reflectivity in Figure 2.26.

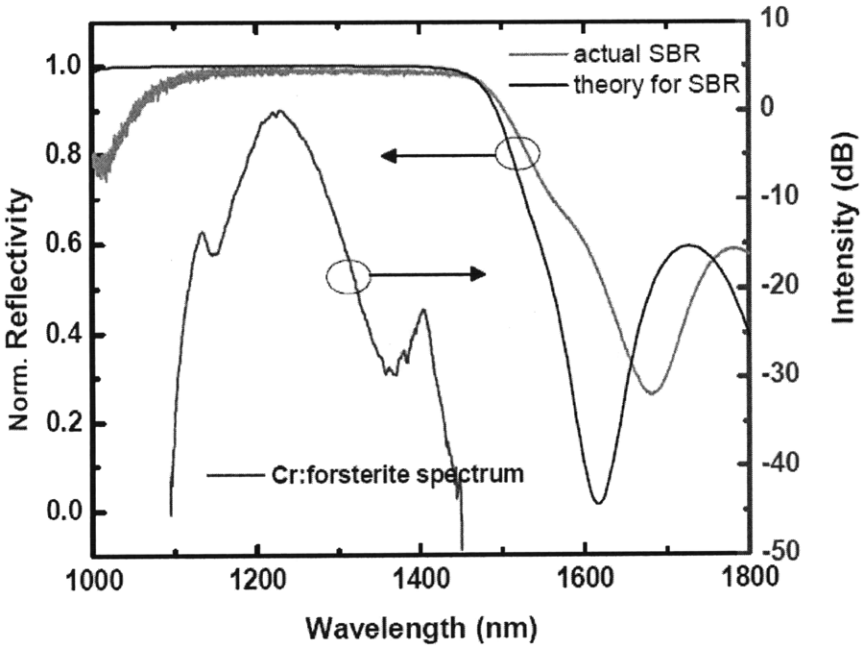

Figure 2.26 Measured and calculated reflectivity spectra for the R946 SBR for the Cr:forsterite laser. A modelocked spectrum achieved with the device is also shown. Data courtesy of J.W. Kim.

Saturable Bragg Reflectors at 800 nm

For Ti:sapphire lasers at 800 nm, the material composition of the SBR structure needed modification in order to absorb and transmit the appropriate wavelengths. The high-index layer of the base mirror was changed from AlGaAs to InGaAlP for 800-nm operation; the absorber layer was changed from InGaAs to GaAs; and the absorber cladding layers were changed from GaAs to InGaAlP. Altogether, the structure consisted of a 7-pair $In_{0.15}Ga_{0.15}Al_{0.35}P/Al_xO_y$ Bragg mirror integrated with a 10-nm GaAs layer centered in a $\lambda/2$-thick InGaAlP cladding layer, as illustrated in Figure 2.27. The square of the electric field profile is also shown in Figure 2.27.

Although InGaAlP with a refractive index of 3.1 resulted in a lower index contrast for the mirror, the Ti:sapphire SBR still had >99% reflectivity over a broad 294-nm bandwidth, as shown in Figure 2.18 earlier. Figure 2.28 shows top-down and side views of a fully-oxidized 500-μm-diameter Ti:sapphire SBR. The mesas were not circular due to the particular wet etch that was used. The structure oxidized in 2.5 hours at 435 °C with no observable delamination.

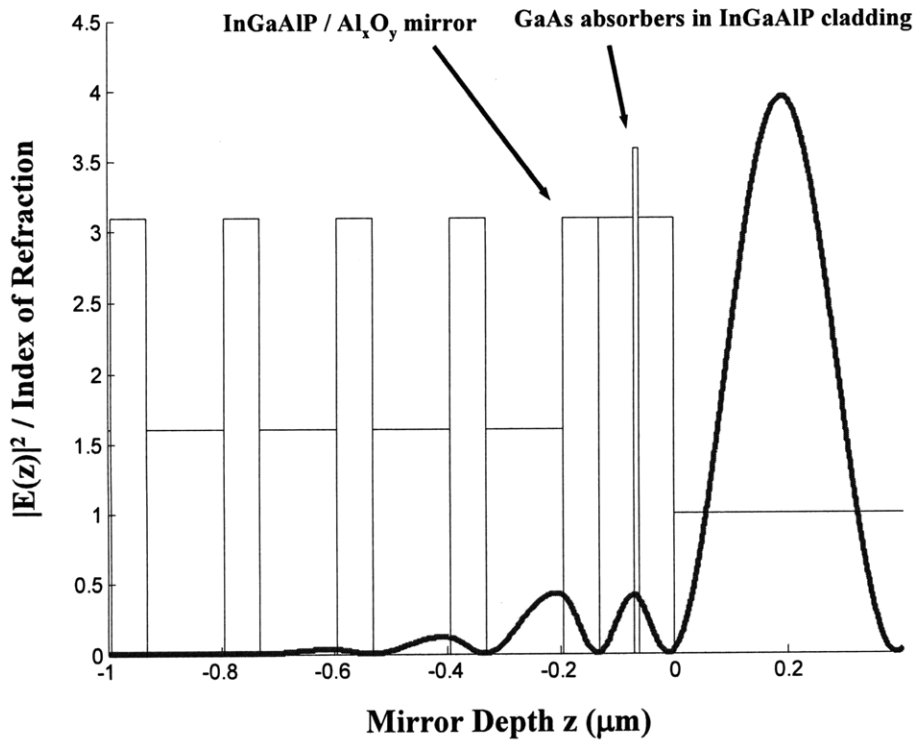

Figure 2.27 Refractive index profile and electric field standing wave pattern of the R1000 SBR, designed for use in the Ti:sapphire laser.

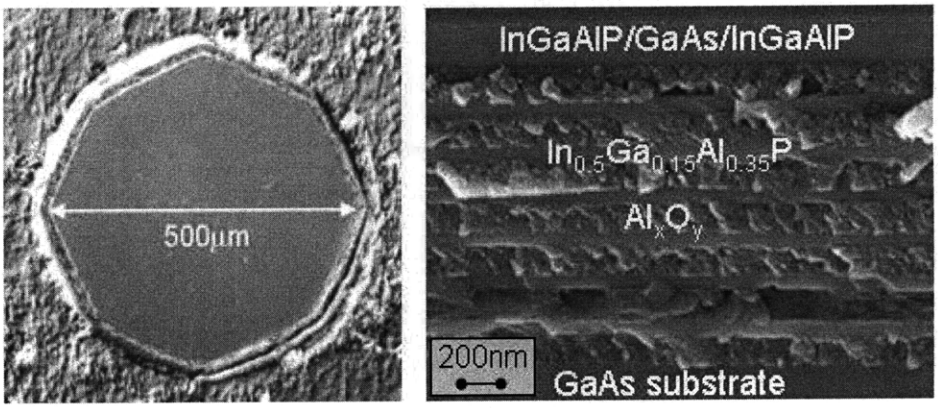

(a) (b)

Figure 2.28 (a) Top-down view of a fully oxidized 500 μm mesa of a InGaAlP/Al_xO_y SBR for the Ti:sapphire laser. (b) Side cross-sectional view of the same fully-oxidized Ti:sapphire SBR [27].

With the SBR, modelocked operation was achieved with a bandwidth suggesting 15-30 fs Fourier-transform-limited pulses. The modelocked Ti:sapphire spectrum is shown below in Figure 2.29(d), together with the other broadband oxidized SBR laser results in the near-infrared.

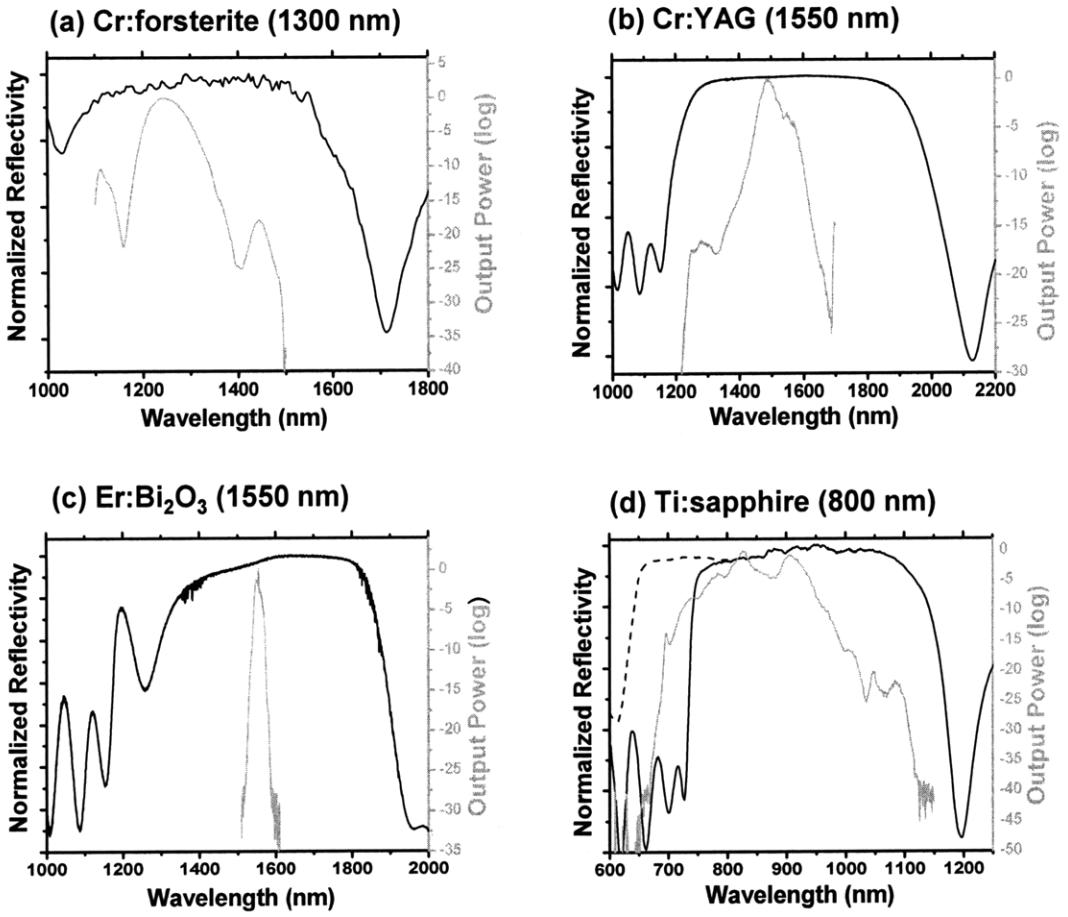

Figure 2.29 SBR modelocked spectra enabled by the oxidized Al_xO_y base mirror design, spanning the visible to the near-infrared [27]. In (d), reflectivities of two SBRs from the same wafer are shown. One measurement (dotted curve) was limited in range by the spectrometer used.

In summary, ultra-broadband monolithically integrated oxidized saturable Bragg reflectors were developed for ultrafast solid-state and fiber lasers spanning the visible to near-infrared wavelengths. All the SBRs tested in lasers generated self-starting ultrashort

modelocked pulses. Sustained operation was possible for several days without observable degradation, illustrating the SBR's durability and high damage threshold.

2.4 Broadband Silicon-Germanium Saturable Bragg Reflectors

In addition to III-V-based broadband semiconductor absorber mirrors, absorbers based on silicon/silicon-dioxide (Si/SiO_2) mirrors were also investigated [33].

Silicon is the material of choice in large-scale integrated electronics. The maturity of existing integration technology and the high-index contrast of silicon and silicon dioxide make it attractive for photonics applications. Until recently, SBRs fabricated as both bulk and quantum-well devices from III-V compound semiconductor materials were not compatible with the silicon material system. A new SBR consisting of a germanium saturable absorber integrated directly on a Si/SiO_2 Bragg mirror however has changed that. The silicon-germanium (Si-Ge) SBR was manufactured in a fully CMOS-compatible process, and it was incorporated into an Er-Yb:glass laser to enable modelocking. We performed pump-probe spectroscopy on these SBRs with 150-fs pulses at 1550 nm. These and the laser results are discussed below.

A schematic of the SBR device structure, along with the field intensity profile, is shown in Figure 2.30(a). The high index contrast of Si ($n = 3.5$) and SiO_2 ($n = 1.45$) makes possible both a high maximum reflectivity and a large stopband with only a few quarter-wave pairs. For this structure, only 6 layer pairs in the Bragg mirror were needed to achieve a maximum reflectivity of 99.8%. A germanium saturable absorber layer, embedded in a $3\lambda/4$-thick Si layer, resides on top of the Bragg stack. The absorber was designed to be at a peak of the field intensity to maximize modulation depth and minimize the saturation intensity. The center wavelength of the structure was designed to be 1400 nm.

A major accomplishment was the fabrication of the device by Felix Grawert and his collaborators in the Kimerling group. The Si-Ge SBR was constructed by repeated poly-Si deposition and thermal oxidation, using a silicon-on-insulator (SOI) wafer as the starting material. The Si and SiO_2 layer thicknesses were 100 nm and 244 nm, respectively. As growth progressed and the structure became thicker, the roughness in the top-most layers increased – an effect that degrades the mirror quality. To circumvent this harmful effect, the top-most layer was bonded to a Si wafer, and the original silicon handle, along with the

buried oxide of the SOI substrate, etched off, reversing the Si/SiO_2 layer sequence of the reflector with respect to layer growth. Essentially, the device was 'flipped.' As a result, the layers with the lowest roughness were now closer to the surface, or the top, of the structure, rather than the other way around. Because of the high index contrast, light incident on the SBR does not penetrate deep into the structure. Consequently, the reflectivity and bandwidth of the mirror were primarily determined by the quality of the top-most layers. A 40-nm-thick germanium absorber layer was then deposited to the top of the structure through the application of the ultrahigh-vacuum chemical-vapor deposition technique developed here at MIT [34]. Finally, a thin oxide was grown on the germanium as a passivation layer and a poly-Si cap layer was deposited. This ensures the germanium layer is crystalline and of high quality. An illustrative summary of this process is shown in Figure 2.30(b).

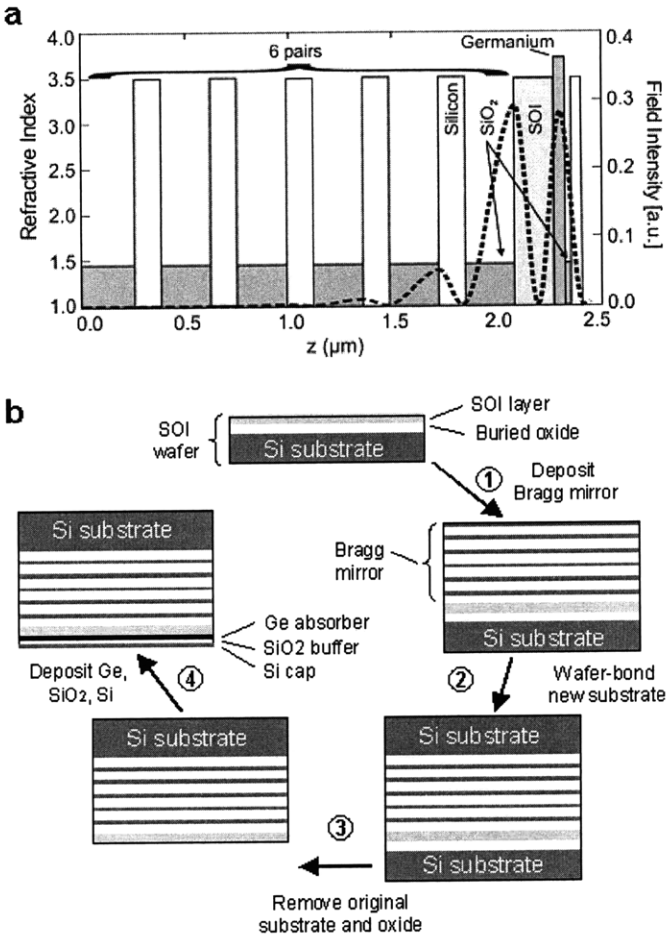

Figure 2.30 Structure and fabrication process of the Si-Ge SBR. (a) Device structure and field intensity profile. (b) Device manufacturing steps. Courtesy of F. Grawert [33].

2.4.1 PUMP-PROBE MEASUREMENTS OF THE SI-GE SBR

The nonlinear response of the device was characterized in a series of pump-probe measurements with 150 fs pulses centered at 1540 nm using the setup shown in Figure 2.9 above. Pump probe traces are shown below in Figure 2.31. A pump-to-probe fluence ratio of 3 to 1 was used. For low to medium fluence values (<40 $\mu J/cm^2$), the germanium layer acted as a fast saturable absorber with a modulation depth of up to 0.13%. Sub-picosecond recovery of the bleaching was observed, with the temporal resolution of the measurement being limited by the pulse durations of our pump-probe setup. We attribute the fast relaxation process to inter-valley scattering within the conduction band. It may also be the result of mid-gap states. From our pump-probe measurements, we estimate the saturation fluence of the Si-Ge SBR to be 34 $\mu J/cm^2$.

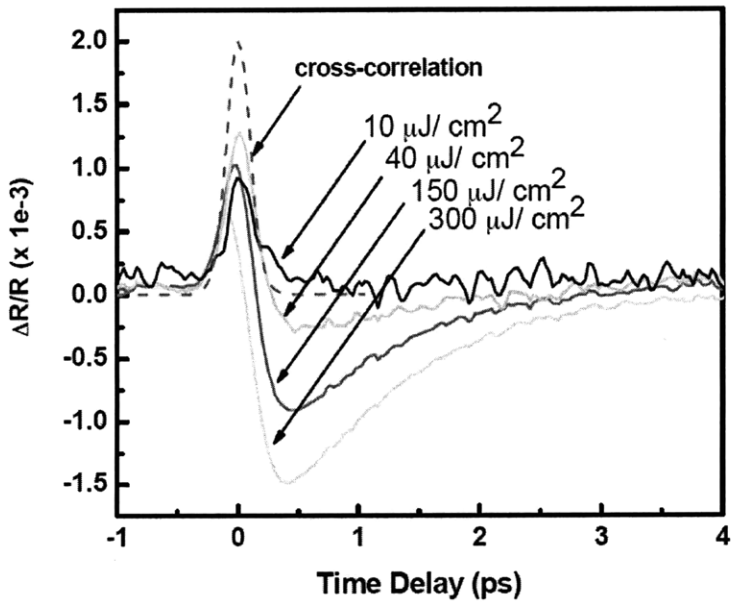

Figure 2.31 Pump-probe traces at low to moderate fluences of the Si-Ge SBR [33]. The dashed line is the cross-correlation of the pump and probe pulse.

At high incident fluences on the order of 300 $\mu J/cm^2$ and above, carriers generated by two-photon absorption induced free-carrier absorption. The germanium layer effectively became an inverse saturable absorber. Figure 2.32 shows pump-probe traces taken at

higher fluence. The probe fluence was kept constant for these measurements. The strong inverse saturable absorber behavior of the Si-Ge SBR can be attributed to the two-photon absorption in the germanium layer, where β_{Ge} = 300 cm/GW, a value much greater than that of silicon or GaAs.

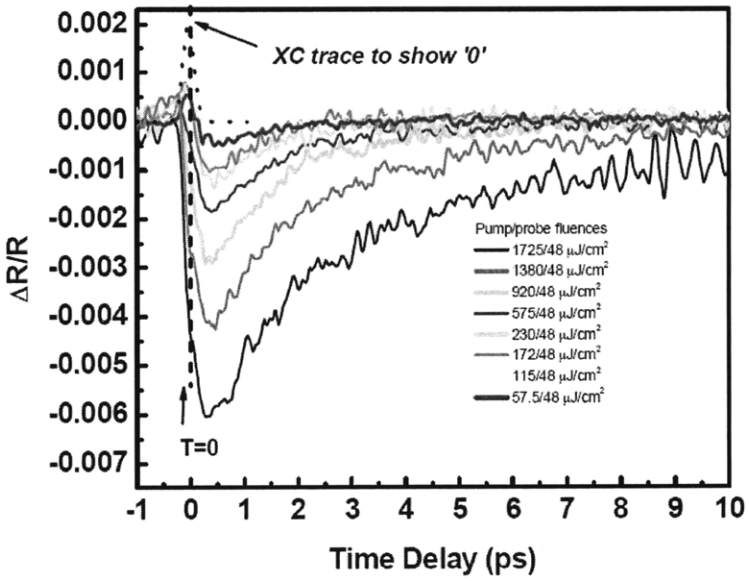

Figure 2.32 Pump-probe traces at high fluences of the Si-Ge SBR. The dashed line is the cross-correlation of the pump and probe pulse.

To verify that the signals observed were mainly from the 40 nm germanium layer, and not from the silicon cladding, measurements were taken on an identical mirror structure that lacked the germanium absorber. These traces are shown in Figure 2.33. Two-photon absorption and free carrier absorption were significantly less in this structure – an order of magnitude lower than that observed in the Si-Ge SBR. Therefore, we concluded that the dynamics of the Si-Ge SBR were dominated by the absorption and bleaching dynamics occurring in the 40-nm Ge absorber.

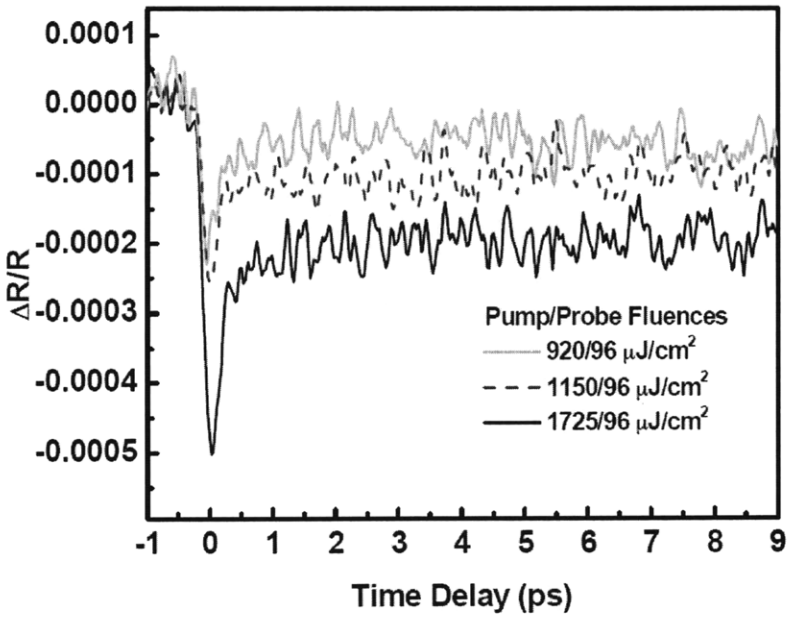

Figure 2.33 Pump-probe traces of a structure similar to the Si-Ge SBR but without the germanium absorbing layer. The pump-probe signals are about an order of magnitude less than for the Si-Ge SBR.

2.4.2 4-Level Model for Describing Si-Ge SBR Dynamics

We posit that a 4-level band structure in germanium is the origin of the dynamics seen in our pump-probe experiments. We modeled and simulated pump-probe experiments in such a 4-level system to see if we could replicate our measurements, as well as to estimate some relative cross sections and lifetimes of these hypothetical energy levels.

The proposed band diagram is shown in Figure 2.34. Energy level L_1 is the state that bleaches, giving rise to positive pump-probe signals. Photons excite carriers up from the ground level L_0 to L_1, and from there, they relax to L_2. From L_2, carriers are either excited to L_3 or they decay back to L_0. The transition from L_2 to L_3 cannot be bleached, so L_3 is a very short-lived state. This transition does contribute to photon loss, however, and the carriers that are excited to L_3 do not immediately decay back down to any of the defined energy levels.

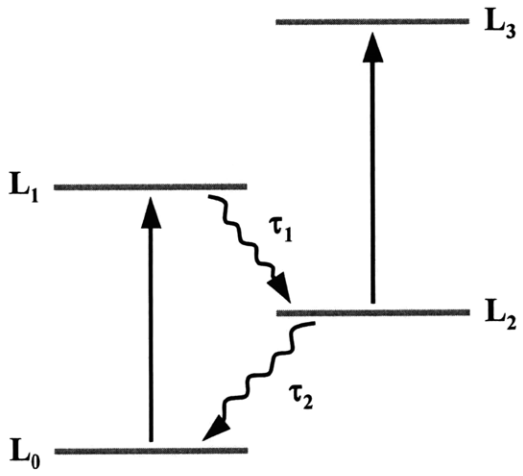

Figure 2.34 Proposed band diagram for describing the origin of the pump-probe dynamics observed in the Si-Ge saturable Bragg reflectors.

The dynamics of this system are governed by the rate equations shown below:

$$\frac{\partial N_0}{\partial t} = -(N_0 - N_1)\sigma_{01}\Phi + \frac{N_2}{\tau_2} \tag{2.1}$$

$$\frac{\partial N_1}{\partial t} = (N_0 - N_1)\sigma_{01}\Phi - \frac{N_1}{\tau_1} \tag{2.2}$$

$$\frac{\partial N_2}{\partial t} = \frac{N_1}{\tau_1} - \frac{N_2}{\tau_2} \tag{2.3}$$

$$\frac{\partial \Phi}{\partial t} = -(N_0 - N_1)\sigma_{01}\Phi - N_2\sigma_{23}\Phi - N_0\beta_{TPA}\Phi^2 \tag{2.4}$$

These equations describe how the population in each energy level evolves with an incident photon flux. Here, N_i denotes the population of each energy level *i*; φ_{xy} is the absorption cross section between levels *i* and *j*; τ_i represents the carrier lifetime of each level *i*; Φ is the photon flux; and β_{TPA} is the two-photon absorption coefficient. It was assumed that τ_3 was equal to zero.

Using this model, we were able to replicate our measured pump probe traces, so it appears that a 4-level band structure is a viable explanation for the pump-probe dynamics we

observed. Figure 2.35 below shows an example fit of the model to measured data. In this case, the measured data was taken at a pump and probe fluence of 306 and 94 $\mu J/cm^2$, respectively. The model suggests a fast recovery time of 200 fs and a slow recovery time of 900 fs, on par with what the laser results in the next section suggest.

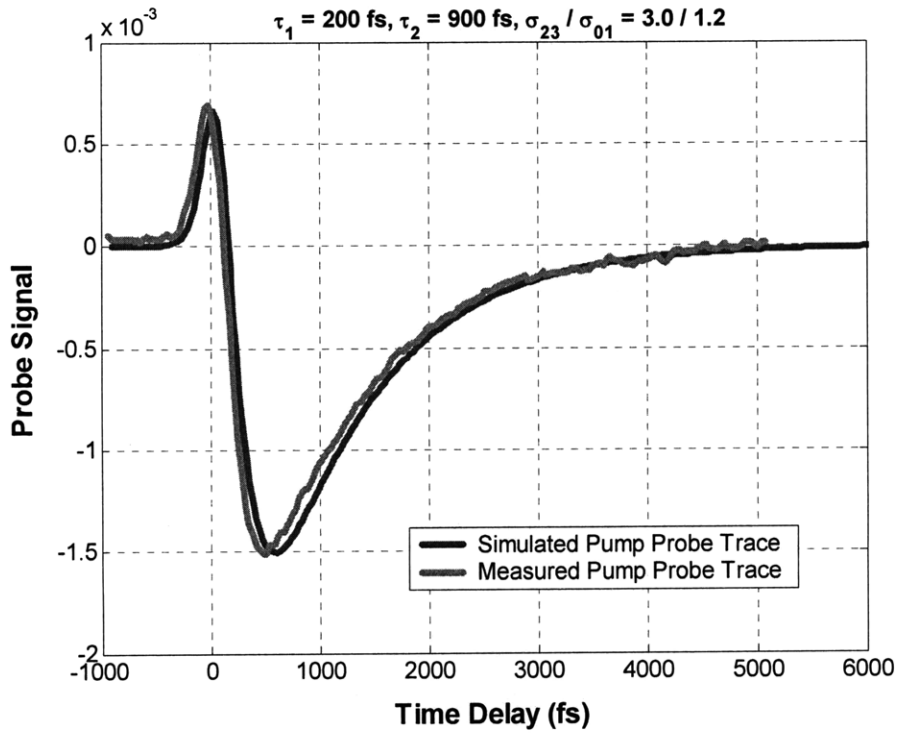

Figure 2.35 Comparison of measured pump-probe trace at pump/probe fluence of 306/94 $\mu J/cm^2$ to simulations results of a 4-level model. Fit suggests a fast recovery time of 200 fs, and a slow recovery time of 900 fs.

2.4.3 Er-Yb:glass Laser Results with the Si-Ge SBR

The observed temporal behavior of the germanium leads to two beneficial effects when the SBR is incorporated into a modelocked laser. First, the fast recovery time permits ultrashort pulse shaping; and, secondly, the onset of the inverse saturable absorber behavior at high fluences helps stabilize high-repetition-rate lasers against the tendency to Q-switch by limiting the maximum intra-cavity power [7, 8].

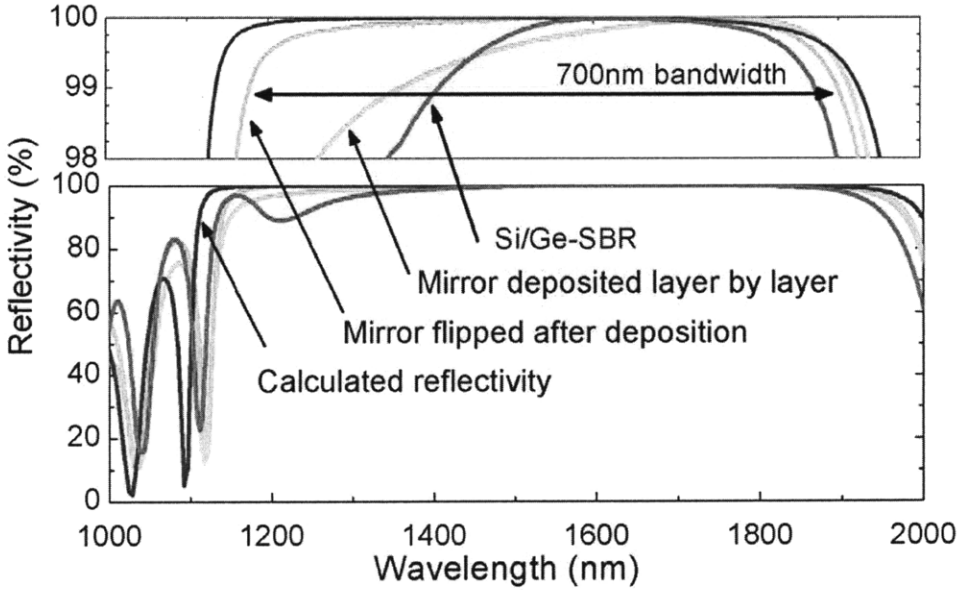

Figure 2.36 Measured and calculated reflectivity of the Si-Ge SBR and the base Si/SiO_2 mirror. Measured reflectivities of the mirror include those for structures fabricated two ways – as-grown and 'flipped' [33]. Data courtesy of F. Grawert.

The measured reflectivity of the Si-Ge SBR is shown in Figure 2.36. In addition, the calculated reflectivity and the measured reflectivities of the base Si/SiO_2 mirrors are also shown. Coming back to the device manufacturing process, one can clearly see there is indeed a significant difference in mirror performance between the as-grown structure, with the roughest layers closer to the surface, and the flipped mirrors structure, with the roughest layers deeper in the structure.

Also from the figure, we see the effect of the germanium absorber. The thin germanium layer grown on silicon was compressively strained, which lead to a shift of the bandgap by 38 nm to shorter wavelengths. As a result, absorption of the germanium only set in at 1580 nm. This resulted in a total loss of 0.3% and a non-saturable loss of 0.17% at the lasing wavelength. In addition, another cause of the low modulation depth was the slight misplacement of the germanium absorber layer away from the peak of the field intensity profile. A larger modulation depth of the SBR could be expected from better positioning of the germanium layer, as well as with the use of a larger thickness.

The fast recovery time of the Si-Ge SBR combined with its high reflectivity led to excellent bandwidth and pulse width performance in a modelocked bulk Er-Yb:glass laser. A schematic of the laser is shown in Figure 2.37(a). The gain crystal was a flat-Brewster

polished Kigre QX/Er phosphate glass. The flat side served as an output coupler with 99.8% reflectivity. The laser was pumped with a Bookham 450-mW fiber-coupled diode laser. The overall intra-cavity loss was minimized with the use of highly reflecting mirrors, low output coupling, and the high reflectivity Si-Ge SBR, leading to an intra-cavity power of 8.7 W. The 4-element laser cavity had a total dispersion of -0.02 ps^2. Finally, the laser was operated with a highly saturated gain, which resulted in a flat gain profile to support a broad optical spectrum.

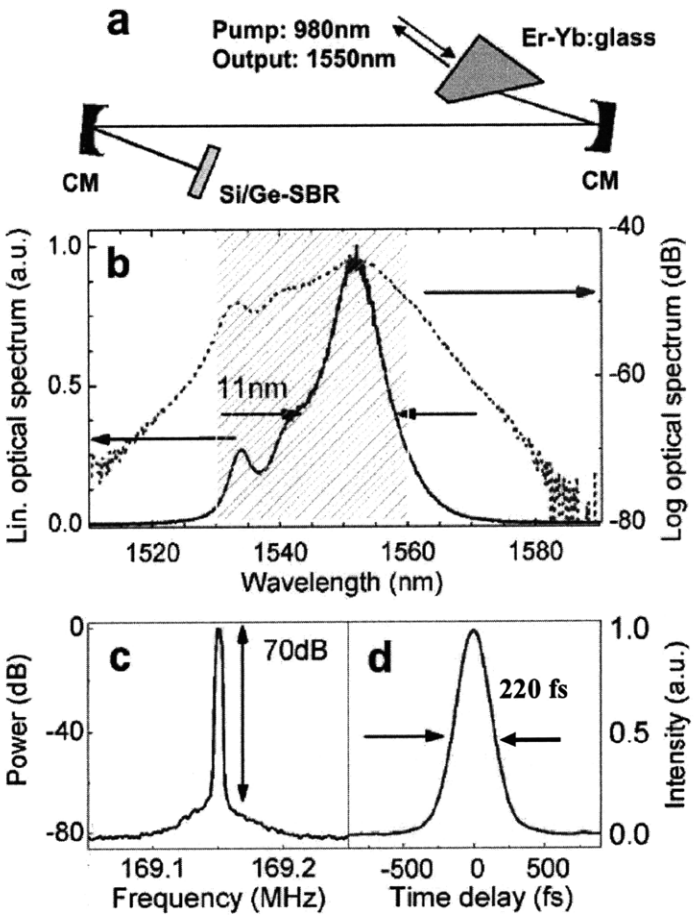

Figure 2.37 Setup and performance of the Er-Yb:glass laser with the Si-Ge SBR. (a) Schematic of the laser cavity. (b) Optical spectrum of the Si-Ge SBR-modelocked Er-Yb:glass laser. (c) Sample RF spectrum of the laser. (d) Background-free intensity autocorrelation measurement of the pulses. Graphic courtesy of F. Grawert [33].

Pulses corresponding to an optical spectrum centered at 1550 nm with a FWHM bandwidth of 11 nm, covering the entire C-band of optical communications at approximately –10 dB level, were generated. The spectrum is shown in Figure 2.37(b). The laser operated at a repetition rate of 169 MHz, and no evidence of Q-switching was observed, irregardless of the pump power used. This can be attributed to the aforementioned inverse saturable absorber behavior. A typical RF spectrum is shown in Figure 2.37(c). And finally, after extra-cavity dispersion compensation with 1 m of single-mode fiber, the pulses were measured to be 220 fs. The intensity autocorrelation is shown in Figure 2.37(d).

To our knowledge, these are the shortest pulses generated from a bulk Er-Yb:glass laser to date, and about an order of magnitude shorter than those obtained solely from mode-locking of an Er-Yb:glass laser with an SBR. The prior pulse width records were 380 fs and 2.5 ps, respectively [35, 36].

REFERENCES

1. D. H. Sutter, G. Steinmeyer, L. Gallman, N. Matuschek, F. Morier-Genoud, U. Keller, V. Scheuer, G. Angelow, and T. Tschudi, "Semiconductor saturable-absorber mirror-assisted Kerr-lens modelocked Ti:sapphire laser producing pulses in the two-cycle regime," Optics Letters **24**, 631 (1999).

2. D. J. Ripin, J. T. Gopinath, H. M. Shen, A. A. Erchak, G. S. Petrich, L. A. Kolodziejski, F. X. Kaertner, and E. P. Ippen, "Oxidized GaAs/AlAs mirror with a quantum-well saturable absorber for ultrashort-pulse Cr^{4+}:YAG laser," Optics Communications **214**, 285 (2002).

3. E. P. Ippen, "Principles of passive mode locking," Applied Physics B **58**, 159 (1994).

4. H. A. Haus, "Theory of mode locking with a slow saturable absorber," IEEE Journal of Quantum Electronics **11**, 736 (1975).

5. H. A. Haus, "Theory of mode locking with a fast saturable absorber," IEEE Journal of Quantum Electronics **46**, 3049 (1975).

6. J. C. Diels and W. Rudolph, *Ultrashort Laser Pulse Phenomena*, Academic Press (1996).

7. T. R. Schibli, E. R. Thoen, F. X. Kaertner, "Suppression of modelocked Q-switching and break-up into multiple pulses by inverse saturable absorption," Applied Physics B **70**, S41 (2000).

8. E. R. Thoen, E. M. Koontz, M. Joschko, P. Langlois, T. R. Schibli, F. X. Kaertner, E. P. Ippen, and L. A. Kolodziejski, "Two-photon absorption in semiconductor saturable absorber mirrors," Applied Physics Letters **74**, 3927 (1999).

9. H. W. Mocker and R. J. Collins, "Mode competition and self-locking effects in a Q-switched ruby laser," Applied Physics Letters **7**, 270 (1965).

10. A. J. DeMaria, D. A. Stetser, and H. Heynau, "Self mode-locking of lasers with saturable absorbers," Applied Physics Letters **8**, 174 (1966).

11. S. Tsuda, W. H. Knox, S. T. Cundiff, W. Y. Jan, J. E. Cunningham, "Mode-locking of ultrafast solid-state lasers with saturable Bragg reflectors," IEEE J. Selected Topics in Quantum Electronics **2**, 454 (1996).

12. U. Keller, K. J. Weingarten, F. X. Kaertner, D. Kopf, B. Braun, I. D. Jung, R. Fluck, C. Honninger, N. Matuschek, and J. Aus der Au, "Semiconductor saturable absorber mirrors (SESAMs) for femtosecond to nanosecond pulse generation in solid-state lasers," IEEE J. Selected Topics in Quantum Electronics **2**, 435 (1996).

13. K. L. Hall, E. R. Thoen and E. P. Ippen, "Nonlinearities in active media," *Semiconductors and Semimetals Volume 59*, Academic Press (1998).

14. I. D. Jung, F. X. Kaertner, N. Matuschek, D. H. Sutter, F. Morier-Genoud, G. Zhang, U. Keller, V. Scheuer, M. Tilsch and T. Tschudi, "Semiconductor saturable absorber mirrors supporting sub-10 fs pulses," Applied Physics B **65**, 137 (1997).

15. D. J. Ripin, C. Chudoba, J. T. Gopinath, J. G. Fujimoto, E. P. Ippen, U. Morgner, F. X. Kärtner, V. Scheuer, G. Angelow and T. Tschudi, "Generation of 20-fs pulses by a prismless Cr^{4+}:YAG laser," Optics Letters **27**, 61 (2002).

16. S. Schon, L. Gallmann, M. Haiml, U. Keller, "Fluoride SESAM for ultrabroadband pulse generation," Proceedings of CLEO **CWB2**, 314 (2001).

17. B. C. Collings, J. B. Stark, S. Tsuda, W. H. Knox, J. E. Cunningham, W. Y. Jan, R. Pathak, and K. Bergman, Optics Letters **21**, 1171 (1996).

18. S. Spalter, M. Bohm, M. Burk, B. Mikulla, R. Fluck, I. D. Jung, G. Zhang, U. Keller, A. Sizmann, and G. Leuchs, Applied Physics B **65**, 335 (1997).

19. M. J. Hayduk, S. T. Johns, M. F. Krol, C. R. Pollock, and R. P. Leavitt, Optics Communications **137**, 55 (1997).

20. Y. Chang, R. Maciejko, R. Leonelli, and A. S. Thorpe, Applied Physics Letters **73**, 2098 (1998).

21. Z. Zhang, T. Nakagawa, K. Torizuka, T. Sugaya, and K. Kobayashi, Optics Letters **24**, 1768 (1999).

22. Z. Zhang, T. Nakagawa, K. Torizuka, T. Sugaya, and K. Kobayashi, Applied Physics B **70**, S59 (2000).

23. J. A. Kong, *Electromagnetic Wave Theory*, EMW Publishing (2000).

24. A. Erchak, *Enhanced Performance of Optical Sources in III-V Materials Using Photonic Crystals*, MIT Doctoral Thesis (2002).

25. K. D. Choquette, K. M. Geib, C. I. H. Ashby, R. D. Twesten, O. Blum, H. Q. Hou, D. M. Follstaedt, B. E. Hammons, D. Mathes and R. Hull, "Advances in selective wet oxidation of AlGaAs alloys," IEEE J. Selected Topics Quantum Electronics **3**, 916 (1997).

26. F. X. Kaertner, N. Matuschek, T. Schibli, U. Keller, H. A. Haus, C. Heine, R. Morf, V. Scheuer, M. Tilsch, and T. Tschudi, "Design and fabrication of double-chirped mirrors," Optics Letters **22**, 831 (1997).

27. S. N. Tandon, J. T. Gopinath, H. M. Shen, G. S. Petrich, L. A. Kolodziejski, F. X. Kaertner, and E. P. Ippen, "Large-area broadband saturable Bragg reflectors by use of oxidized AlAs," Optics Letters **29**, 2551 (2004).

28. S. N. Tandon, *Engineering Light using Large Area Photonic Crystal Devices*, MIT Doctoral Thesis (2005).

29. S. N. Tandon, J. T. Gopinath, A. A. Erchak, G. S. Petrich, L. A. Kolodziejski, and E. P. Ippen. "Large Area Oxidation of AlAs Layers for Dielectric Stacks and Thick Buried Oxides," Journal of Electronic Materials **33**, 774 (2004).

30. J. W. Sickler, J. T. Gopinath, S. N. Tandon, H. Sotobayashi, G. S. Petrich, E. P. Ippen and L. A. Kolodziejski, "Femtosecond laser using broadband erbium-doped bismuth-oxide gain fiber," CLEO **CThK6** (2004).

31. T. R. Schibli, J. Kim, O. Kuzucu, J. T. Gopinath, S. N. Tandon, G. S. Petrich, L. A. Kolodziejski, J. G. Fujimoto, E. P. Ippen, and F. X. Kaertner, "Attosecond active synchronization of passively mode-locked lasers by balanced cross correlation," Optics Letters **28**, 947 (2003).

32. J. -W. Kim, "Toward single-cycle optical pulses," MIT SM Thesis (2004).

33. F. J. Grawert, J. T. Gopinath, H. M. Shen, E. P. Ippen, F. X. Kartner, S. Akiyama, J. Liu, K. Wada, and L. C. Kimerling, "220-fs erbium-ytterbium:glass laser mode locked by a broadband low-loss silicon/germanium saturable absorber," Optics Letters **30**, 329 (2005).

34. H.-C. Luan, D. R. Lim, K. K. Lee, K. M. Chen, J. G. Sandland, K. Wada, L. C. Kimmerling, "High-quality Ge epilayers on Si with low threading-dislocation densities," Applied Physics Letters **75**, 2909 (1999).

35. G. Wasik, F. W. Helbing, F. Koenig, A. Sizmann, G. Leuchs, "Bulk Er:Yb:glass soliton femtosecond laser," CLEO proceedings **56**, CMA4 (2001).

36. G. J. Spuehler, L. Gallman, R. Fluck, G. Zhang, L. R. Brovelli, C. Harder, P. Laporta, U. Keller, "Passively modelocked diode-pumped erbium-ytterbium glass laser using a semiconductor saturable absorber mirror," *Electronics Letters* 35, 567-569 (1999).

Chapter 3

SATURABLE BRAGG REFLECTORS FOR HIGH-REPETITION-RATE LASERS

3.1 INTRODUCTION

Compact high repetition rate fiber and waveguide lasers present a challenging and promising application for semiconductor saturable absorber mirrors. As mentioned before, high repetition rate modelocked lasers may be of very practical interest to optical communications systems. As data transmission rates continue to increase, pulsed lasers are becoming increasingly important for telecom applications. High-data-rate communications systems and high-speed photonic digital-to-analog conversion can benefit greatly from a pulsed laser source [1, 2]. In addition, the mode spacing in the spectral comb generated by the laser increases with higher repetition rates, and the resultant spectral and spatial resolution of these individual frequency modes may be leveraged for optical arbitrary waveform applications.

There are many compelling reasons to use a pulsed laser directly as an optical source in telecommunications systems. First, this approach eliminates the need for a modulator to shape the pulses, as shaping is already done by the laser. The modulator need only change the state between two successive pulses to encode data streams onto the pulse train. This approach simplifies system architecture, increases efficiency, and reduces cost. Furthermore, the extinction ratio of pulsed lasers is typically very good and much higher than for modulated cw sources. This improves the signal-to-noise ratio of the system and

allows further scaling to higher repetition rates through optical time-division multiplexing. Finally, pulsed lasers can have a transform-limited output, which occupies the minimum optical bandwidth for a given pulse duration and thus bit rate – an important practical consideration given the limited availability of spectrum.

Many of these properties also make high-repetition-rate femtosecond lasers attractive for optical arbitrary waveform generation, as discussed in the Introduction chapter. The high laser repetition rate yields a frequency comb with sufficient spacing to enable manipulation by optical filter banks and modulators. And the wide bandwidth provides many frequency lines, and hence greater freedom, in generating arbitrary waveforms.

Different approaches have been used to achieve these pulsed optical sources. Actively mode-locked fiber lasers can generate multi-GHz pulse repetition rates, but only with harmonic modelocking. And even then, good pulse stability is only achieved by using complex stabilization techniques. Edge-emitting semiconductor lasers, passively or actively mode-locked, can generate repetition rates of more than 1 THz [3], but with fairly limited average output power due to the small mode area. Optically pumped vertical-cavity surface emitting lasers (VCSELs), which can be passively modelocked with semiconductor saturable absorber mirrors, do not suffer from this power limitation and have generated pulses with significantly higher average power in the multi-gigahertz regime (e.g. 950 mW, 15 ps pulse width, 6-GHz repetition rate) [4]. Here, in this thesis, we concentrate on developing saturable absorber mirrors for use in passively modelocked ion-doped solid-state lasers, with the purpose of achieving high repetition rates *and* femtosecond pulses, rather than the aforementioned approaches, which generated picosecond pulses.

Diode-pumped ion-doped solid-state lasers are well known for their potential to deliver high-power mode-locked pulse trains in diffraction-limited beams. They feature efficient, robust, and compact operation. Because of their relatively low emission cross sections, however, these lasers exhibit a strong tendency for Q-switched modelocking (QML) in short cavity configurations designed for high repetition rates. In the QML regime, the modelocked pulse train is amplitude-modulated with a long Q-switched envelope. As a result, cavity and absorber designs must be carefully adjusted to counter the Q-switching tendencies of these gain media.

Note that harmonic modelocking, with multiple pulses circulating in the laser resonator, could also be used to increase the repetition rate of a solid-state laser [5]. The advantage of

this approach is that the Q-switched modelocking tendency, which depends on the cavity length, is then weaker compared to the case of a short fundamentally modelocked laser with the same repetition rate. However, a stable inter-pulse spacing is challenging to achieve. For this work, we concentrate on the more straightforward approach of fundamental modelocking, with only a single pulse circulating in the laser resonator.

Passively modelocked, optically pumped lasers have been demonstrated with repetition rates up to 77 GHz in the 1 μm wavelength range [6]. The availability of gain media with large emission cross sections in the 1 μm wavelength range strongly reduces the tendency for Q-switching instabilities [7]. Earlier attempts to replicate similar repetition rates at 1.5 μm had met with limited success, due to the relatively lower cross sections of laser gain media there, until the recent demonstration of a 100-GHz passively modelocked Er:Yb:glass laser [8]. This laser incorporated a semiconductor saturable absorber mirror optimized for low saturation fluence and a moderate modulation depth. The short cavity was also optimized to minimize mode areas in the gain medium as well as on the saturable absorber mirror.

Semiconductor saturable absorbers are a logical choice for ultrashort pulse generation with short cavities. As seen in the previous chapter, SBRs play a key role in achieving stable, self-starting cw modelocking in ultrafast lasers, in a wide variety of laser systems. In general, however, the lasers described in Chapter 2 had relatively low repetition rates, on the order of 100 MHz. The SBRs for those lasers were optimized for broadband operation. As we ramp up the repetition rate, the fluence incident on the SBR decreases in two ways. First, if we assume that the average intra-cavity power remains the same, the higher repetition rate reduces the individual pulse energies, which reduces the incident fluence. Second, the cavity length, which is inversely proportional to the repetition rate for a fundamentally modelocked laser, shortens; and, if intra-cavity mirrors have the same radii of curvature as before, the intra-cavity lasing modes are larger. As a result, the spot size incident on the SBR increases, and a larger spot size translates into a lower fluence. If the fluence incident on the saturable absorber in the SBR structure is not high enough, Q-switched modelocking will be favored over cw modelocked operation. Therefore, for higher repetition rate systems, we must re-visit the SBR design in order to support multi-GHz operation.

Three key SBR device parameters come to the forefront and are explored in more depth in this chapter – the modulation depth of the SBR, the recovery time, and the dispersion

profile. The saturation fluence, which is highly relevant in this discussion, is essentially the outcome of the first two of these parameters.

Section 3.2 gives a brief overview of the challenges of building high-repetition-rate, short-cavity laser systems. Section 3.3 will be a drilldown around the modulation depth of saturable absorbers and will examine the use of resonant coatings to enhance the modulation depth of an SBR design. The resonant coating layers effectively reduce the saturation fluence by amplifying the fluence 'seen' by the absorber deeper in the structure. Section 3.4 covers the recovery time of saturable absorbers designed for high-repetition-rate systems – specifically, the technique of proton bombardment. Finally, Section 3.5 covers the role of dispersion in modelocking and the integration of dispersion compensation into SBR designs.

As in Chapter 2, the results presented here were possible only through a collaborative effort. Gale Petrich tirelessly grew the SBR structures layer by layer for us in Professor Leslie Kolodziejski's lab. Appreciation is all the greater considering the structures fabricated were not oxidized but had a full 22-layer-pair base mirror, which prolonged the structure growth to an entire day. Ali Motamedi performed pump-probe characterization on the SBRs in the Ippen lab, and generously provided many of the charts shown in Section 3.4. Laser testing of the SBR samples were done by Hyunil Byun, and later on Michelle Sander. Hyunil kindly provided the data and results presented in Section 3.5.

3.2 Challenges of Building High-Repetition-Rate Systems

Passive modelocking of a solid-state laser with saturable absorbers is a well-established technique. As mentioned, however, saturable absorbers introduce a Q-switching tendency that can drive the laser into the Q-switched modelocked operation [9]. This is an undesirable operating mode for most applications, given the output pulse train no longer consists of pulses of constant power/energy. The complications of building high-repetition-rate short-cavity lasers all manifest themselves primarily in the form of Q-switching instabilities. As a result, one can arrive at this same undesirable result from a number of different paths.

3.2.1 Q-SWITCHED MODELOCKING

To start, insufficient modulation depth can be the culprit. The modulation depth of the SBR must be large enough to obtain stable and self-starting modelocking. A larger modulation depth is desirable for generating shorter pulses. However, this also tends to increase the nonsaturable losses, which decreases the intracavity power, which lowers the fluence incident on the absorber relative to its saturation point and increases the tendency for Q-switched modelocking.

Recovery time is another possible cause of QML. For the lasers discussed in this chapter, the repetition rate is on the order of GHz. The recovery time of the SBR becomes important when it is comparable to the resonator roundtrip time or even larger. For example, the roundtrip time for a 50 GHz laser is 20 ps. SBRs typically optimized for low nonsaturable losses tend to have relatively long recovery times, on the order of 50 ps for MOCVD-grown devices. In this case, the SBR's ability to recover between pulses becomes limited. With low-temperature MBE growth, significantly faster recovery could be achieved, but at the cost of higher nonsaturable loss, which again leads us back to QML.

Finally, multi-GHz lasers have low pulse energies compared to the 100-MHz repetition-rate lasers discussed in Chapter 2, since the same amount of energy that can be extracted from the gain media is now divvied up into many more pulses in a given time window. Again, this leads to a low fluence operating point relative to the saturation fluence and increases the tendency to QML.

The physical picture of the Q-switched modelocking dynamics can be understood as follows. If, for some reason, the pulse energy rises slightly above its steady state value, this pulse energy fluctuation can initially grow because the stronger bleaching of the absorber increases the net roundtrip gain. Essentially, the saturable absorber 'rewards' higher energy pulses with lower resonator losses, thereby enhancing the relaxation oscillations. However, eventually, the increased pulse energy will saturate the gain. If the gain saturation is strong enough, this will lead to a dampening of the pulse energy, which soon returns to its steady state. If this gain saturation does not occur and there is additional preferential bleaching by the saturable absorber, the relaxation oscillations are undamped or even growing in amplitude, and we obtain QML operation.

3.2.2 Design Guidelines for High-Repetition-Rate Lasers

Basically, three different aspects need to be taken into consideration when designing high repetition-rate solid-state lasers – (1) choice of gain medium, (2) laser cavity design, and (3) saturable absorber parameters. The last point on the saturable absorber design is the focus of our work; however, we will briefly review all three points below.

Choice of Gain Medium

Gain media with large laser emission cross sections are desirable. The larger the cross section the lower the gain saturation fluence. And for a given fluence, this means stronger gain saturation behavior to clamp down on relaxation oscillations and prevent QML.

Cavity Design

The cavity design of high repetition rate lasers is important because the mode sizes in the gain medium and on the saturable Bragg reflector both influence the QML threshold. Smaller mode areas translate to higher incident fluence relative to the gain and absorption saturation points.

The cramped confines of multi-gigahertz cavities limit the number of cavity components and exclude the use of bulky optics. For a standing-wave cavity, a 100-GHz repetition rate corresponds to only 1.48 mm of separation between the end mirrors in air or even less with a gain medium in the cavity. It is paramount with such limited space to optimize the lasing modes as much as possible.

Additionally, the beam quality of the pump source becomes ever more important for the highest repetition rates, as the mode size in the gain medium should be minimized as much as possible. The pump beam must stay within the laser mode throughout the gain medium. It is important to realize that an increased pump mode size is unacceptable even after propagation by several absorption lengths because these lasers are typically operated far above threshold, and higher-order transverse modes can easily start lasing and destabilize the modelocking process.

SBR Design

The parameters of the saturable absorber mirror play a key role in obtaining stable self-starting cw modelocked operation at a high repetition rate.

Q-switching can be reduced by operating the absorber far above the saturation fluence, in principle. Absorber damage, multiple pulsing, and other instabilities set limits to this approach. In practice, the general rule of thumb is operating 2-3 times above the saturation fluence. With the small pulse energies present in multi-gigahertz lasers, this requires fairly small mode areas, which are difficult to achieve due to geometrical restrictions. Therefore, SBR designs with low saturation fluence are desirable.

A low saturation fluence can be achieved in multiple ways. The most pragmatic would be to place the absorber at a peak in the electric field standing wave pattern in the SBR. This placement maximizes the modulation depth. Moreover, if said peak could be enhanced with the addition of resonant coating layers, which would increase the modulation depth as well, the saturation fluence would be lowered even more. In a high-repetition-rate laser, this becomes a necessary design extension as the intra-cavity powers are much lower. A happy byproduct of the increased modulation depth is a stronger modelocking force, which reduces the output pulse widths.

As mentioned already, the recovery time of the SBR becomes important when it is comparable to the cavity round-trip time or even larger. In that case, the SBR recovery after one roundtrip is incomplete. The effective reflectivity change is decreased, which would decrease QML tendency and seemingly indicate that incomplete recovery would be advantageous for high repetition rate lasers. However, a fast recovery time is still desirable for pulse shaping, so ideally, it would be optimal to have a faster absorber with lower saturation fluence and lower non-saturable losses for high-repetition-rate lasers.

The final parameter to consider in designing SBRs, not only for high-repetition-rate lasers but for all ultrafast lasers, is the integration of dispersion compensation. Given the premium placed on space, this is especially important for short-cavity lasers. The positive dispersion accumulated in traversing the gain medium needs to be compensated in the laser cavity somewhere, in order to achieve ultrashort pulses in addition to the high repetition rate. Integrating this component into the SBR structure represents an elegant and compact solution, and can be a crucial step to achieving multi-gigahertz repetition rate *and* femtosecond pulses. As always in optics, the manipulation of phase holds the key, and the addition of coating layers of specific thicknesses can achieve the necessary dispersion

compensation profile. Dispersion-compensating SBRs can play a key role in achieving multi-gigahertz operation and femtosecond pulses.

3.3 Resonant Layers for Modulation Depth Enhancement

A large modulation depth is desirable for generating short pulse widths. Generally, the greater the modulation depth, the shorter the pulse widths that can be generated by an SBR. For high-repetition-rate laser systems, which oftentimes have high intra-cavity losses, a large modulation depth relative to the non-saturable losses is also needed for the absorber to be effective in starting and stabilizing modelocked operation. Having a large modulation depth can prevent the laser from entering into Q-switched modelocking operation.

In order to enable modelocking, in some cases, and, more importantly for us, to stave off Q-switched modelocking, the effective fluence 'seen' by the saturable absorber needs to be increased. The solution is the application of additional resonant coatings on top of the standard quarter-wavelength SBR structure. For a given fluence incident on the surface of the SBR, resonant coatings enhance the field inside the structure, specifically at the location of the absorber. In the case of a high-repetition-rate system, a low incident fluence on the SBR surface can translate into a much higher effective fluence at the absorber location, and hence a higher modulation depth, with the use of resonant coatings.

3.3.1 Resonant Coating Theory

A brief explanation of how resonant coatings work follows.

Figure 3.1 shows the configuration that we will use as the basis for our discussion of resonant coatings. (Incidentally enough, we'll be revisiting a similar schematic when we discuss Gire-Tournois dispersion compensating SBRs later in this chapter.) The structure in Figure 3.1 is effectively a Fabry-Perot cavity, with two mirrors, or more correctly, mirror structures, flanking a spacer layer on both sides. Light is incident from the left side with field amplitude *a*. The mirror on the left represents the resonant coating layers, and the mirror on the right the high-reflectivity base mirror of the SBR. Recall that a standard SBR is comprised of a highly reflective quarter-wave Bragg stack integrated with an absorber inside a cladding layer. This cladding layer corresponds to the spacer layer

depicted above, so the absorber is located between the two mirrors. The reflectivity of the highly reflecting base mirror is assumed to be 1, so the field reflection coefficient r_2 is taken to be unity. The field reflection coefficient of the resonant layers relative to the spacer layer (and absorber) is r_1. The spacer layer has a thickness of l.

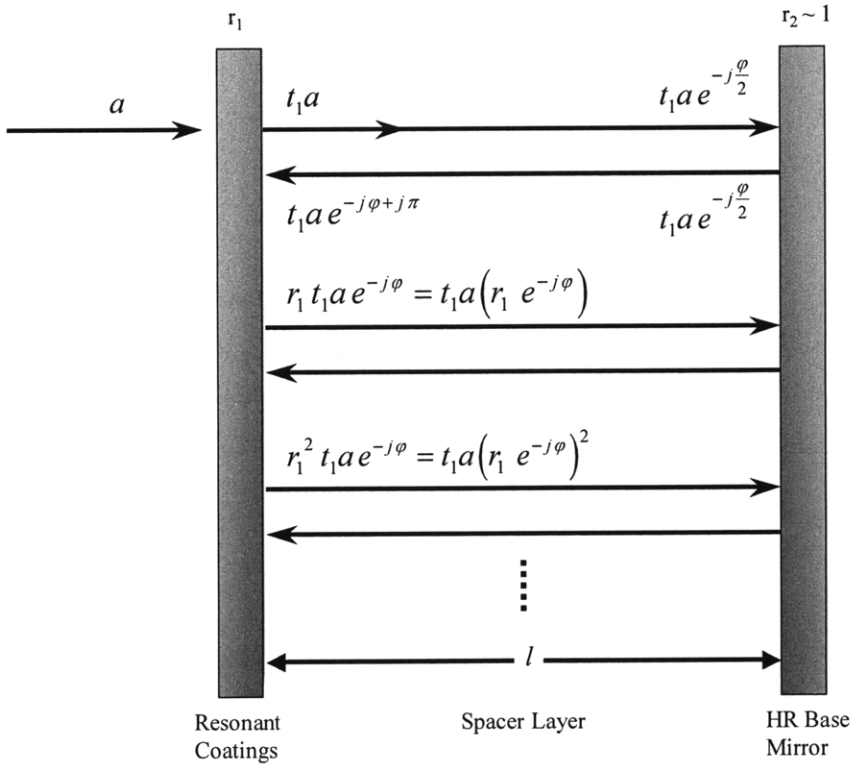

Figure 3.1 Schematic of a resonantly-coated SBR structure. Traveling waves inside the cavity and their equations are depicted to illustrate the basic physics of the structure.

The incident pulse transmits through the resonant coating layers on the left and is then split into a series of pulses multiply reflected between the two mirrors with different delays. The field distribution inside is obtained by the superposition of this infinite series of beams. It is clear this field distribution strongly depends on the relative phase between the successive reflections, and specifically it depends on the thickness of the spacer layer. The roundtrip transit time t_{RT} in the spacer layer corresponding to the thickness is

$$t_{RT} = \frac{2nl}{c} \tag{3.2}$$

where c is the speed of light and n is the index of refraction of the spacer layer. This assumes normal incidence light.

There is a subtle point to be made here before we proceed with the calculation. When used in a laser, the light incident upon this structure is pulsed, not continuous. Hence, the simplifying assumption of using cw plane waves for our analysis is not automatic. If the pulse width $t_p << t_{RT}$, the fields of successive pulses in the interferometer do not interfere due to the lack of temporal overlap, and there would be no intensification of the field in the spacer layer. Field enhancement therefore implies effective interference between the partial fields. This requires the spacer layer to be a thin interferometer such that $t_p >> t_{RT}$. Application of this technique to optical pulses with durations of 100 fs or less thus necessitates interferometers with roundtrip transit times of 10-20 fs or less, or 3-6 μm or less, which is indeed the case in our structures. With the condition $t_p >> t_{RT}$ satisfied, the response of the interferometer can be well approximated by investigating the response of a cw field.

The enhanced field amplitude $a_{enhanced}$ at the left side of the spacer layer is simply a summation of the main pulse and all the satellite pulses from subsequent reflections inside the cavity. The math is shown in the figure, and we get:

$$a_{enhanced} = t_1 a + t_1 a\left(r_1\, e^{-j\varphi}\right) + t_1 a\left(r_1\, e^{-j\varphi}\right)^2 + \cdots \tag{3.2}$$

, where t_1 is the field transmission coefficient of the resonant coatings and $\varphi = 2\pi n/\lambda \times 2l$ is the roundtrip phase change in the spacer layer. Recognizing the expression as a geometric sum, we get:

$$a_{enhanced} = \frac{t_1 a}{1 - r_1\, e^{-j\varphi}} \tag{3.3}$$

The field intensity enhancement factor is defined as:

$$F_{enhanced} \equiv \frac{\left|a_{enhanced}\right|^2}{\left|a\right|^2} = \frac{t_1^{\,2}}{1 + r_1^{\,2} - r_1(2\cos\varphi)} \tag{3.4}$$

In order to maximize the field enhancement, the thickness l of the spacer layer is set so that the term cos φ is unity, or

$$\varphi = m\,2\pi$$

where m is an integer equal to one or greater. For m = 1, this corresponds to a spacer layer of thickness λ/2, which just so happens to be the thickness of the SBR cladding layer in which the absorber resides. The maximized field intensity enhancement is

$$\left(F_{enhanced}\right)_{\max} = \frac{t_1^{\,2}}{1+r_1^{\,2}-2r_1} = \frac{1-r_1^{\,2}}{(1-r_1)^2} \tag{3.5}$$

A plot of the field enhancement as a function of the reflectivity of the resonant coating is shown in Figure 3.2. As you can see, the higher the reflectivity of the resonant coatings, the greater the field enhancement becomes.

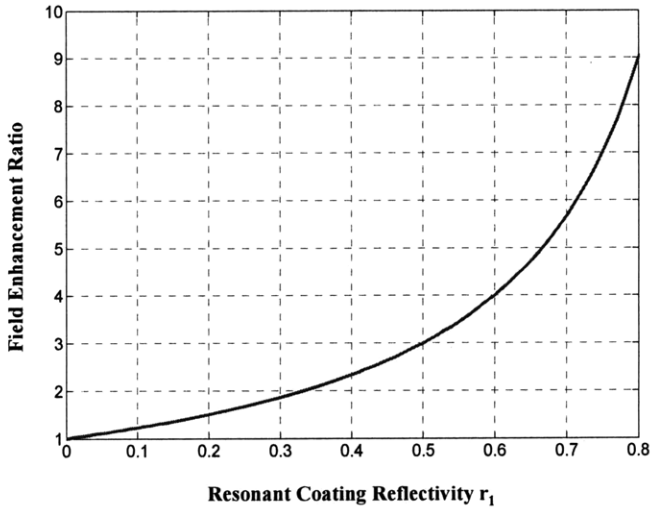

Figure 3.2 Field enhancement ratio as a function of the resonant coating reflectivity for the configuration shown in Figure 3.1.

3.3.2 STRUCTURE DESIGNS

An example of a resonantly coated SBR structure is shown in Figure 3.3. This is, in fact, growth VA88, which was one of four samples we designed and fabricated for laser implementation. Note that the orientation of Figure 3.3 has been flipped from the configuration shown above in Figure 3.1. Light is incident from the right hand side now. The standard SBR structure with the absorber-cladding section on top of a quarter-wave Bragg stack is shown on the left and the resonant layers

are the additional coatings to the right. The base Bragg mirror of the SBR is a 22-pair GaAs/$Al_{0.95}Ga_{0.05}As$ quarter-wave stack designed for a center wavelength of 1550 nm. The thicknesses of the GaAs and $Al_{0.95}Ga_{0.05}As$ layers are 155 nm and 133 nm, respectively. The spacer/cladding layer is λ/2-thick, with a 60-nm $In_{0.537}Ga_{0.463}As$ absorber, highlighted in red, centered in GaAs. The flanking GaAs layers are both 83 nm thick. The InGaAs composition was chosen so that band edge would be at 1580 nm.

The resonant coating layers are simply quarter-wave pairs, oriented so that the high-index layer faces the absorber. The orientation does in fact matter – with only a few quarter-wave pairs, the reflectivity is dependent on the order of the layers in the Bragg stack. The resonant layers are also GaAs/$Al_{0.95}Ga_{0.05}As$ quarter-wave pairs with the same dimensions as before. However, the top-most AlGaAs layer has 50% aluminum composition, in order to avoid oxidation. This $Al_{0.50}Ga_{0.50}As$ layer is 124 nm thick.

Figure 3.3 shows the structure of the VA88 SBR, as well as the electric field standing wave pattern. In contrast to uncoated SBRs, the intensity inside the structure does not rapidly decay down and is relatively high, as expected.

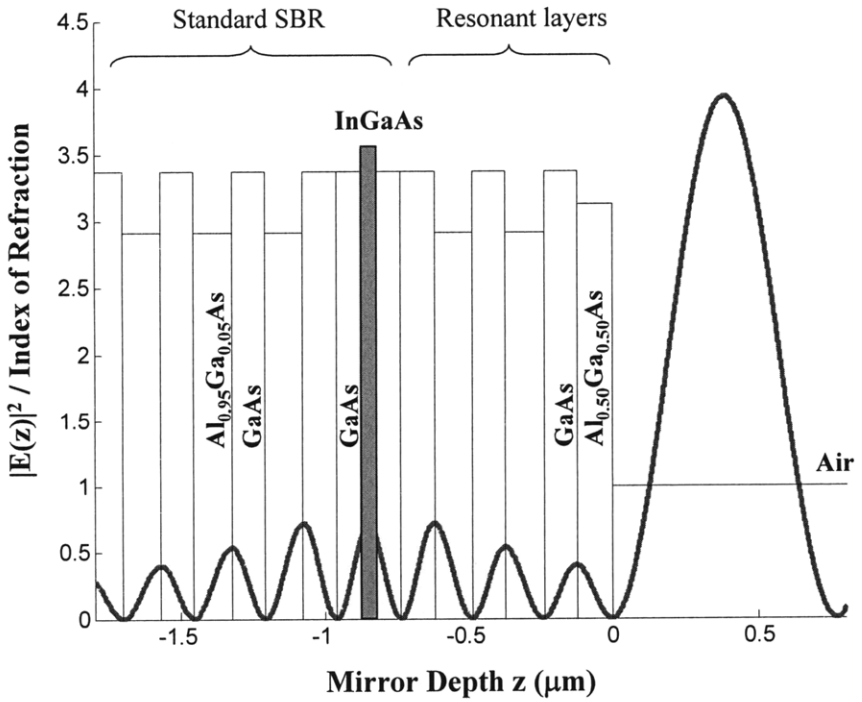

Figure 3.3 Structure and field intensity profile of growth number VA88, a resonantly coated SBR designed for use in high repetition rate lasers. A 60-nm InGaAs absorbing layer on top of a 22-pair GaAs/AlGaAs Bragg mirror is overgrown with a 3-pair GaAs/AlGaAs resonant coating for enhanced modulation depth.

As additional quarter-wave layer pairs are added to the resonant layer, the reflectivity of the resonant coating r_1 in Equation (3.4) increases, thereby increasing the field enhancement. That is, in fact, what we see from designs with more resonant pairs. Figure 3.4 shows how the reflectivity of the SBR changes as you add more pairs to the resonant coating. The structure used for the calculation is of the same form as VA88, as shown in Figure 3.3, except the number of layer pairs in the overgrowth is changed. The profile corresponding to N=3 is the actual calculated reflectivity for the VA88 SBR. Figure 3.5 summarizes the increase in modulation depth as a function of the number of layer pairs in the resonant coating structure. With a 3-pair resonant coating layers, as you see above in Figure 3.3 for VA88, the field enhancement ratio is approximately 2x. As the field inside the SBR is enhanced, the modulation depth increases and the saturation fluence decreases.

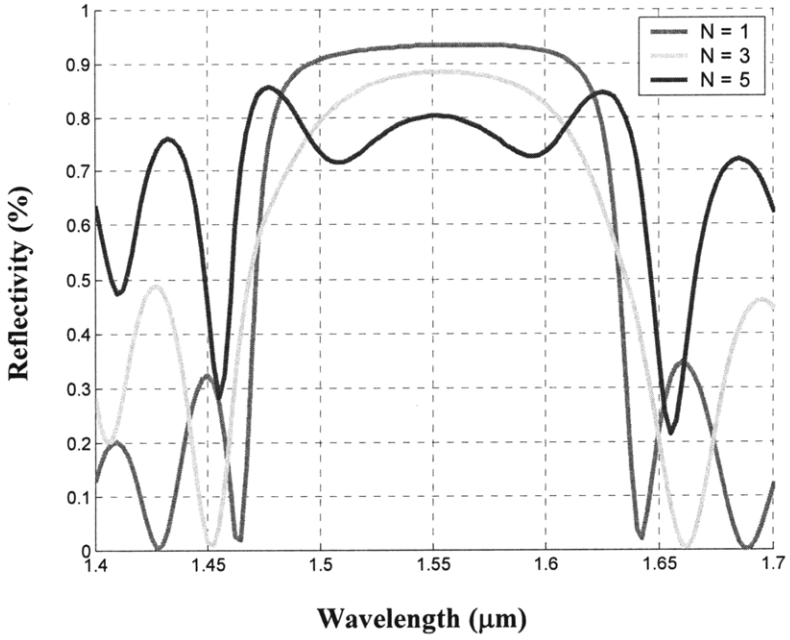

Figure 3.4 Unbleached reflectivity profiles for different resonant coating reflectivities r_1, demonstrating the effect of additional layer pairs. As layer pairs are added, the reflectivity of the top-mirror increases, which increases the field enhancement at the absorber, thereby increasing the modulation depth of the SBR. The profile for N = 3 (middle) is the calculated reflectivity for SBR growth number VA88.

Number of resonant coating layer pairs	Modulation depth at 1550 nm %	Peak $\|E\|^2$ in absorber % of N = 1 field
1	7	100
3	12	209
5	20	389

Figure 3.5 Summary of different resonant orders and their corresponding modulation depths for the VA88-like SBR structures.

The sister structure to VA88 – growth number VA89 – was also grown and fabricated for laser implementation, and its schematic is shown in Figure 3.6. The base mirror remains the same as for VA88, however, rather than place the absorber in the cladding/spacer layer, it is located in the first high-index quarter-wave layer of the base mirror. VA89 is also overgrown with a 3-pair GaAs/AlGaAs resonant coating for enhanced modulation depth. As with VA88, the top-most layer was $Al_{0.50}Ga_{0.50}As$ in order to avoid oxidation. The structure design with layer thicknesses for both VA88 and VA89 are summarized below in Figure 3.7.

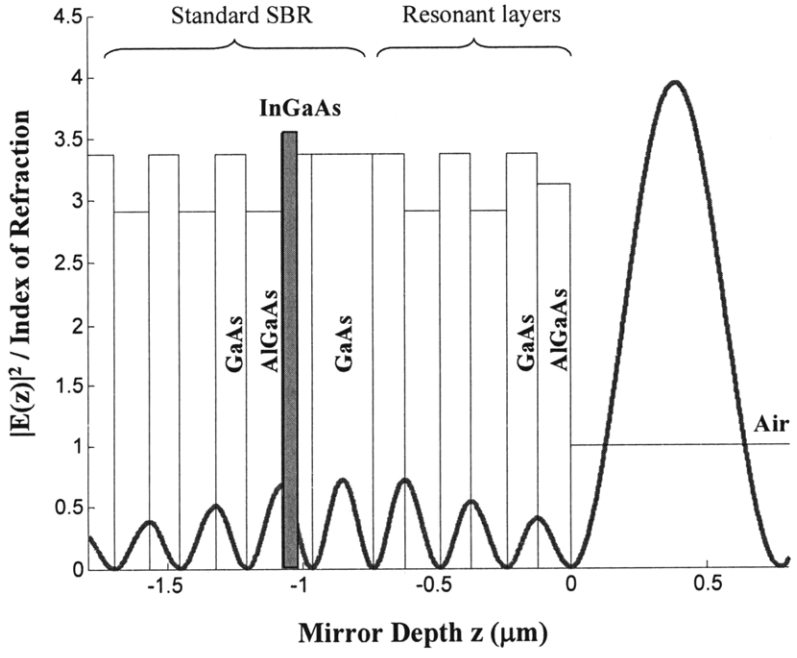

Figure 3.6 Structure and field intensity profile of growth number VA89. The 60-nm InGaAs absorbing layer has been shifted into the first high-index quarter-wavelength-thick layer of the Bragg mirror. The structure is also overgrown with a 3-pair GaAs/AlGaAs resonant coating for enhanced modulation depth.

VA88		VA89	
Material	**Thickness (nm)**	**Material**	**Thickness (nm)**
$Al_{0.50}Ga_{0.50}As$ / GaAs	124 / 115	$Al_{0.50}Ga_{0.50}As$ / GaAs	124 / 115
$Al_{0.95}Ga_{0.05}As$ / GaAs × 2	133 / 115	$Al_{0.95}Ga_{0.05}As$ / GaAs × 2	133 / 115
GaAs	83	GaAs	230
$In_{0.54}Ga_{0.46}As$	60	GaAs	52
GaAs	83	$In_{0.54}Ga_{0.46}As$	60
GaAs / $Al_{0.95}Ga_{0.05}As$ × 22	115 / 133	$Al_{0.95}Ga_{0.05}As$	133
GaAs	substrate	GaAs / $Al_{0.95}Ga_{0.05}As$ × 21	115 / 133
		GaAs	substrate

Figure 3.7 Summary of VA88 and VA89 SBR designs. Corresponds to Figures 3.3 and 3.6.

The calculated reflectivity for VA89 is shown in Figure 3.8. As expected, given the location of the InGaAs absorber in the electric field standing wave pattern in Figure 3.6, the modulation for VA89 is slightly lower. Overall, the general magnitude, bandwidth and modulation depth of the reflectivity profile are similar to those for VA88.

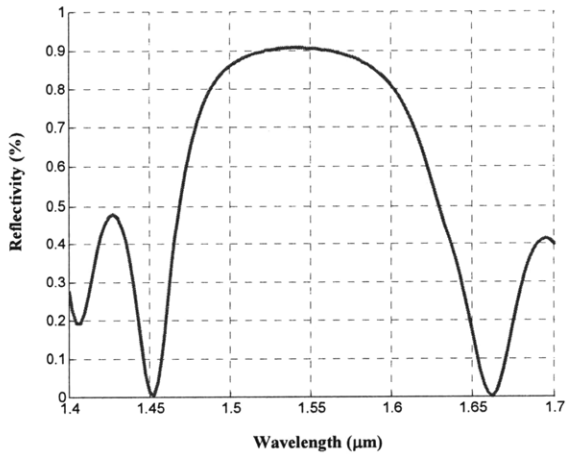

Figure 3.8 Calculated reflectivity of the VA89 SBR.

At the time of this writing, initial laser testing of VA88 and VA89 is still underway by Hyunil Byun and Michelle Sander. However, reflectivity measurements have been done

and are shown below in Figures 3.9 and 3.10 for VA88 and VA89, respectively. They match relatively well with the simulated results.

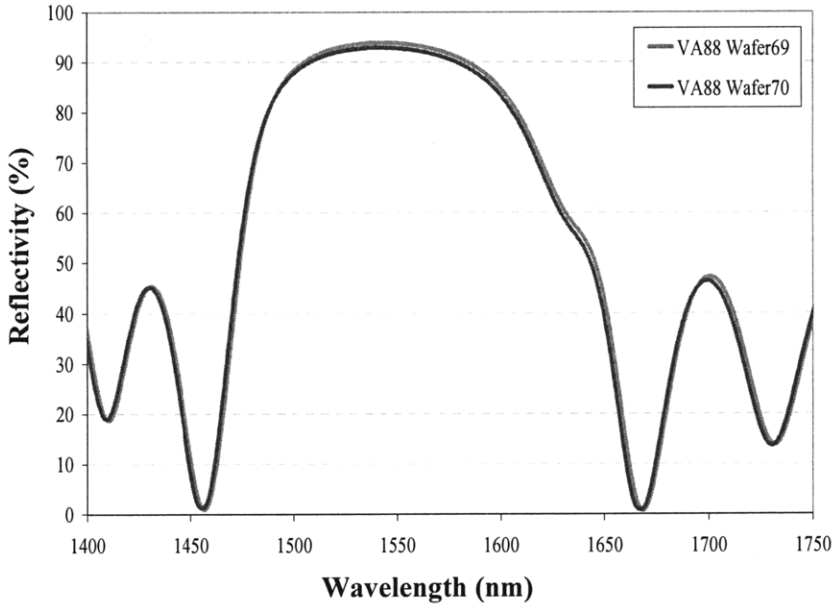

Figure 3.9 Measured reflectivity profiles of the VA88. Measurements of different wafers yield the same result.

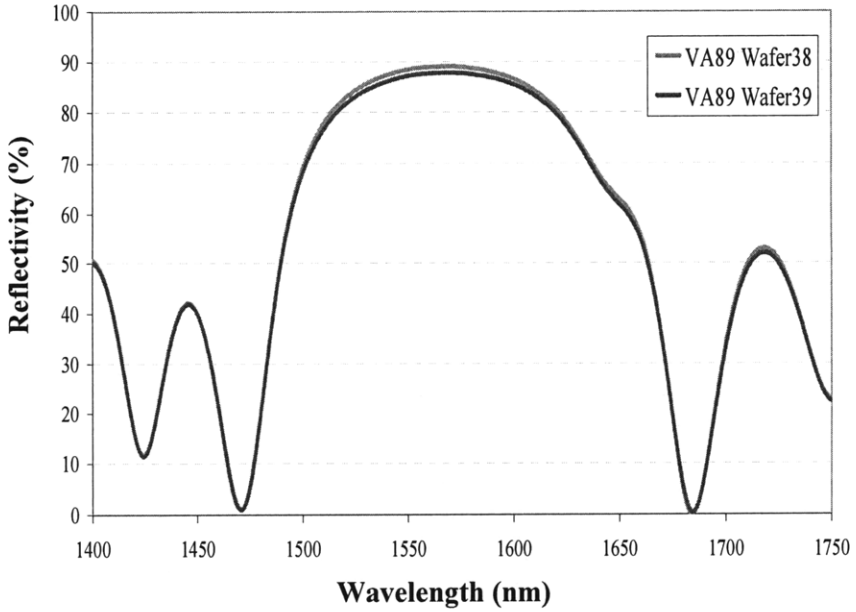

Figure 3.10 Measured reflectivity profiles of the VA89. Measurements of different wafers yield the same result.

Although resonant coatings provide enhanced modulation depths, they can bring undesirable side effects as well. With the resonant coatings, the field intensity increases not only in the absorber layers, but its neighboring layers as well. You can see this in Figures 3.3 and 3.6. The increased intensity causes larger non-saturable loss, and, just as importantly, opens the possibility that two-photon absorption in those non-absorbing layers becomes more of a factor, both in terms of loss and the recovery time. For the former, low-loss materials need to be used if possible. For the latter, proton bombardment is a potential solution, and is the subject of the next section.

3.4 Reducing Saturable Absorber Recovery Time

The importance of carrier lifetime has already been discussed in Chapter 2 for the shaping of short pulses. For optimal operation of a saturable absorber, the absorption recovery time should be shorter than the time between successive pulses in the train. Considering that 10 GHz operation translates to a roundtrip transit time of 100 ps, SBRs for such lasers should recover fully in less than 100 ps. Although full recovery would be optimal, high-repetition-rate lasers with SBRs that do not fully recover within one cavity roundtrip have also been demonstrated.

Semiconductor recovery times can be reduced via defect introduction, an approach that has a long history. Defect states can be introduced in a material through strain, low-temperature molecular beam-epitaxy (LT-MBE) growth, or through post-growth ion or neutron bombardment. Both LT-MBE growth and ion bombardment have been used in demonstrations of passive modelocking [10, 11]. In contrast to LT-MBE growth, ion implantation is a relatively simple post-growth process step and is a more mature technology [12]. A variety of ions have been used for lifetime reduction in semiconductor saturable absorbers, including protons, alpha particles, gold, and arsenic [13, 14, 15, 16, 17].

As defects are created during ion implantation, carrier recombination is enhanced at these sites, thereby reducing the lifetime of the material [18, 13, 19, 20]. Generally, as the implanted ion dosage is increased, recovery lifetimes decrease. The relationship between ion dose and damage, though, is nonlinear; and the penetration depth depends on many factors, such as the target material(s), the ion species used for bombardment, and the ion velocity [21].

It has been shown that heavier ions create more stable defect centers, however, heavy ions at high energies can create unwelcome amorphous layers, which can saturate lifetime reduction, and, in some cases, even increase the lifetime with higher bombardment levels [17, 14, 22, 23]. Lighter ions avoid this problem, so higher energies can be used, which allows deeper penetration depth without sacrificing device nonlinearity [14]. Lifetimes of 200 fs have been achieved in As-implanted GaAs, and lifetimes of ~100 fs have been achieved in proton-bombarded InP [12, 24]. For these reasons, we decided to use proton bombardment to shorten saturable absorber recovery times in our experiments.

Disadvantages of proton bombardment include increased non-saturable loss and reduced modulation depth, which can potentially disrupt laser modelocking. This is also the case with LT-MBE growth. The increased non-saturable loss and reduced non-linearity of the devices, however, can be mitigated with a post-process anneal.

3.4.1 BACKGROUND

The study of the penetration of charged particles into matter has a long history, dating back to the discovery of radioactive particles in 1895. It is a rich field and a subject unto itself, and outside the scope of this thesis. We briefly cover the basic ideas here.

Upon entering any absorbing medium, the incident charged particle used for ion implantation immediately interacts simultaneously with many electrons. In any one such encounter, the electron feels an impulse from the attractive Coulomb force as the incident particle passes its vicinity. Depending on the proximity of the encounter, this impulse may be sufficient either to raise the electron to a higher-lying shell within the absorber atom (excitation) or to remove completely the electron from the atom (ionization). The energy that is transferred to the electron must come at the expense of the charged particle, and its velocity is therefore decreased as a result of the encounter. A very small portion of the particle's energy is transferred in each single interaction. Thus, the incident particle loses its energy over the course of many such interactions during its passage through the absorbing medium. At any given time, the particle is interacting with many electrons, so the net effect is to decrease its velocity continuously. As the energy of the penetrating charged particle falls, the rate of energy loss increases according to the Bethe-Bloch formula [25].

$$-\frac{dE}{dx} = \frac{4\pi e^4 z^2}{m_0 v^2} NB \tag{3.6}$$

where

$$B \equiv Z\left[\ln\frac{2m_0v^2}{I} - \ln\left(1-\frac{v^2}{c^2}\right) - \frac{v^2}{c^2}\right]$$

In these expressions, v and ze are the velocity and charge of the incident charged particle, N and Z are the number density and atomic number of the absorbing atoms, m_0 is the electron rest mass, and e is the electronic charge [26]. The parameter P represents the average excitation and ionization potential of the absorber. For non-relativistic charged particles, which is the case for us, only the first term in B is significant.

There are two primary implications from the Bethe-Bloch formula. First, the rate of energy loss is inversely proportional to the energy, or velocity of the incident charged particle. As the energy decreases, more interactions occur, thereby increasing the energy loss. When the energy eventually falls below a certain threshold, an electron (or electrons, depending on the ion) will attach to the charged particle, dramatically reducing its effective charge, and lowering the energy loss caused by the collisions, until the particles comes to a stop in the absorbing medium. Second, the higher the atomic number Z of the absorbing atom, the greater the rate of energy loss.

For the most part, the paths taken by these charged particles tend to be quite straight because the particle is not greatly deflected by any one encounter, and interactions occur in all directions simultaneously. Charged particles are therefore characterized by a definite range in a given absorber material. This range represents a distance beyond which no particles will penetrate. Energy loss in a material however is a stochastic process. Therefore, a spread of penetration depths always results when an initially mono-energetic beam of particles is implanted in an absorbing material. Many particles lose their energy at an "average depth," although some will lose all their energy earlier, and some later. This results in a finite width to the penetration depth known as "range straggling." The shape of the particle deposition concentration as a function of the penetration depth, known as a Bragg curve or Bragg peak, is illustrated in Figure 3.11.

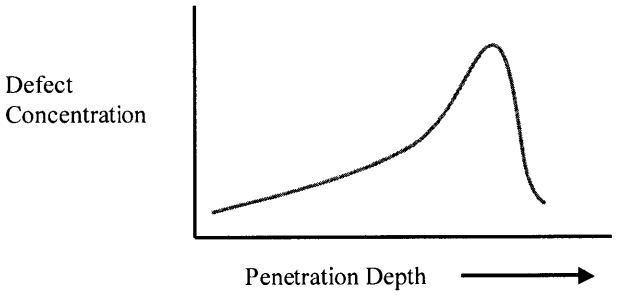

Figure 3.11 An example of a Bragg curve, showing the concentration of ion implantation as a function of penetration depth into the target material.

The Bragg curve is approximately Gaussian-shaped, with the peak defined as the *range*. This Gaussian shape is a result of the rate-of-energy-loss-to-energy relationship outlined above. In addition, the higher the atomic number Z of the target material, the lower is the range, and the entire distribution is closer to the surface. Higher Z corresponds to a greater stopping force, which also leads to a narrower width of the Bragg curve.

Calculating these Bragg curves, for the purposes of designing proton bombardment parameters, would require the application of quantum mechanics and radiation transport principles. SRIM (the Stopping and Range of Ions in Matter) and TRIM (the Transport of Ions in Matter) are two simulation packages for that purpose. They can simulate the stopping range and distribution of ions into matter for up to 2 GeV in energy. These codes use a quantum mechanics treatment of the ion-atom collisions and can perform quick calculations, through the use of efficient Monte Carlo methods [25]. Specifically, TRIM can accept complex targets made of compound materials with up to eight layers, each of different materials, making it the most relevant for our structures. TRIM calculates both the final 3-dimensional distribution of the ions, as well as all the kinetic phenomena associated with the ion's energy loss, such as target damage, sputtering, ionization, and phonon production.

For the purposes of designing the proton bombardment for our experiments, we performed some quick calculations in SRIM with single layers of the III-V semiconductor materials that comprise our SBRs. These results, together with guidance from empirical data from past devices, allowed us to develop some broad design parameters [27], as discussed below. The practical takeaways were rules of thumb regarding proton energies and how they relate to the width and depth of the depositions in our experiments.

3.4.2 EXPERIMENTAL SETUP

In our SBR structures, we use protons to bombard GaAs, AlGaAs, and InGaAs material layers. The base case for the proton energy level is 40 keV. At this energy, the protons can penetrate approximately 400 nm deep into a structure and create defects along its entire path, as described by the Bragg curve. For every additional 50 keV in proton energy, roughly 300 nm of incremental semiconductor material can be penetrated. Keep in mind these are approximations and the damage profile is nonlinear. The peak widths for these protons are typically 100-150 nm, and even more for low energies. Therefore, for a single quantum well, or absorber layer, one proton energy level is sufficient. For depositions in thicknesses greater than 500 nm, a more complex dosing schedule would be required, as we will discuss and provide later.

In addition to the VA88 and VA89 structures described earlier in Section 3.3, two other SBR structures were fabricated for proton bombardment and subsequent implementation in a high-repetition-rate laser – VA86 and VA87. These are versions of VA88 and VA89 without the resonant coatings. The material composition and layer thicknesses of VA86 are the same as the base mirror in VA88. VA87 has a 20-nm InGaAs absorber layer, rather than the 60-nm absorber in VA89, hence the thickness of the first GaAs quarter-wave layer in the base mirror is different – 94 nm rather than 52 nm. The remainder of the two mirrors are the same. The VA86 and VA87 SBR structures are shown below in Figures 3.12 and 3.13. Without the resonant coating layers, the reasoning behind the VA87 design becomes clearer – to reduce the amount of material in the SBR structure. By eliminating the GaAs cladding section, the idea was to reduce potential TPA losses and non-saturable losses, given the light penetration into VA87 is similar to VA86.

The reflectivity profiles of VA86 and VA87 are shown in Figures 3.14 and 3.15, respectively. Compared to their respective simulated results, VA86 has slightly less modulation depth at 4% than the designed value at 5%, and VA87 has a measured stopband that is shifted towards longer wavelengths. The misalignment may be due to a number of reasons. For one, the absolute value of the measured FTIR reflectivity may have an offset. In addition, the material composition of the absorber may be different from the expected values and slight differences in growth may contribute to differing linear absorption values. The refractive indices, which contain the linear loss information, of the materials in the SBR were taken from Gale Petrich and were specific for the MBE machine. Finally, the layer thicknesses may not have been grown to their original designed values. For instance, VA87 had a slight misstep in its growth about 7 layer pairs from the top that is the likely cause of the shift to longer wavelengths. (It was a long day.)

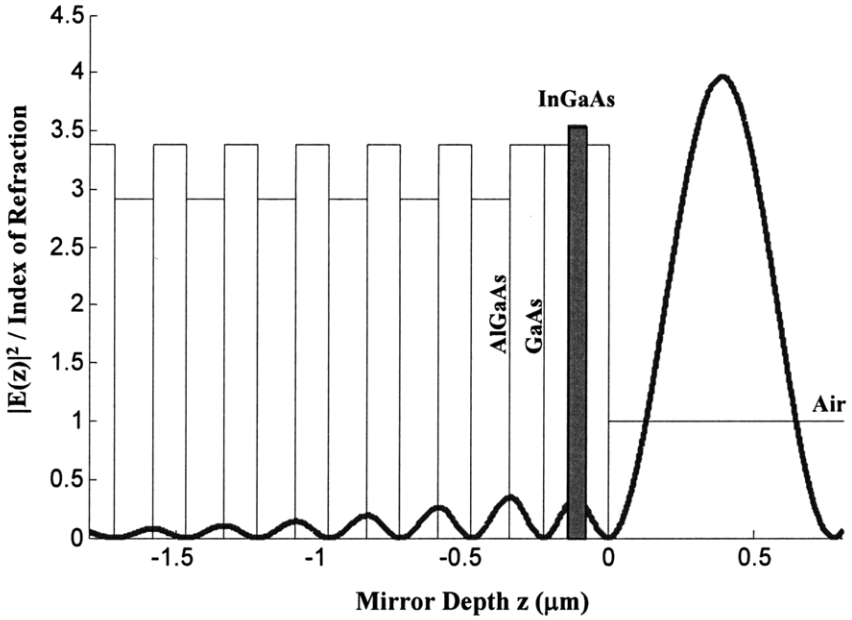

Figure 3.12 Device structure and field intensity profile of growth number VA86, a standard SBR designed for use in high repetition rate lasers with the assistance of proton bombardment. The 60-nm InGaAs absorbing layer is centered in the GaAs cladding layer to maximize field overlap and reduce the saturation fluence.

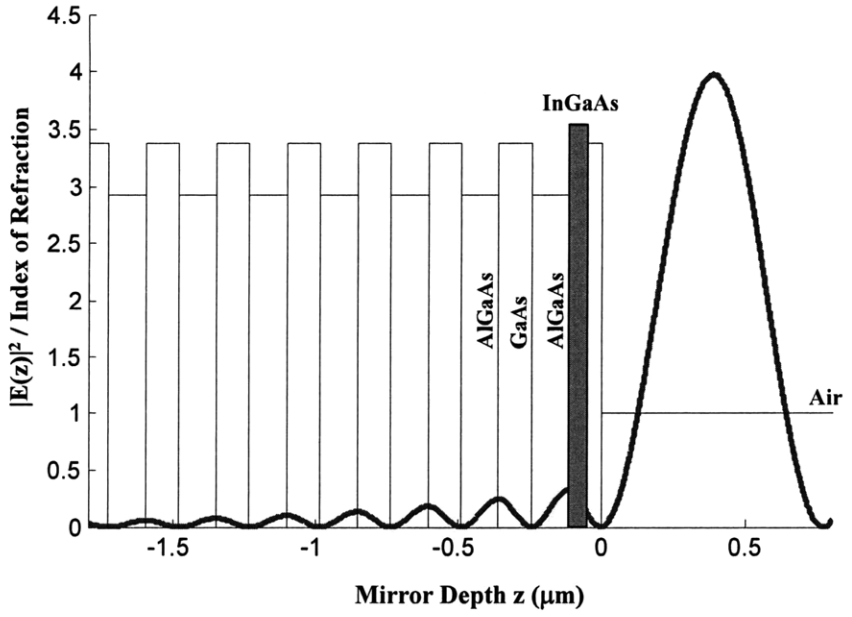

Figure 3.13 Device structure and field intensity profile of growth number VA87, a standard SBR designed for use in high repetition rate lasers with the assistance of proton bombardment. A 20-nm InGaAs absorbing layer has been shifted into the first high-index quarter-wavelength-thick layer of the Bragg mirror.

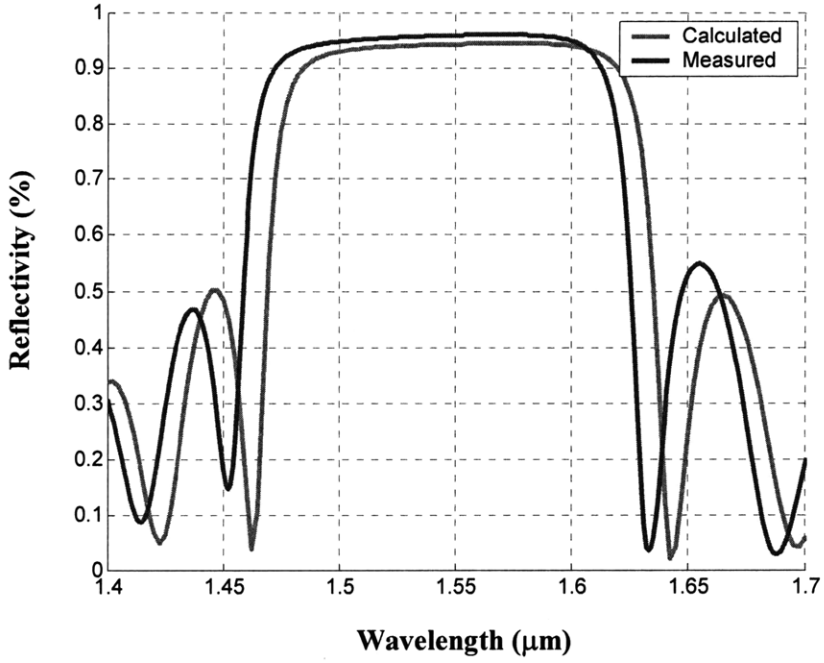

Figure 3.14 Calculated and measured reflectivity profiles of VA86.

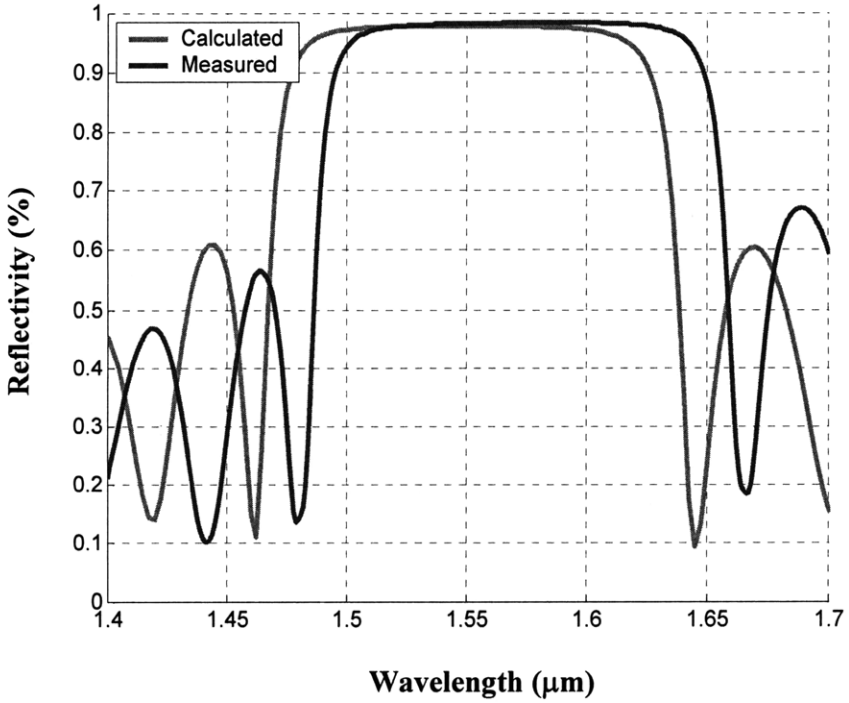

Figure 3.15 Calculated and measured reflectivity profiles of VA87.

Samples of VA86 and VA87 were prepared and sent away for proton bombardment. Proton bombardment was performed by Kroko Incorporated in California. The initial dosing scheme used 40 keV protons at dosage levels of 10^{13}, 10^{14}, and 10^{15} protons/cm^2. Multiple samples were processed for each dosage. At the time of this writing, there were ten sample classes in all that were available for laser testing. These are summarized below in Figure 3.16.

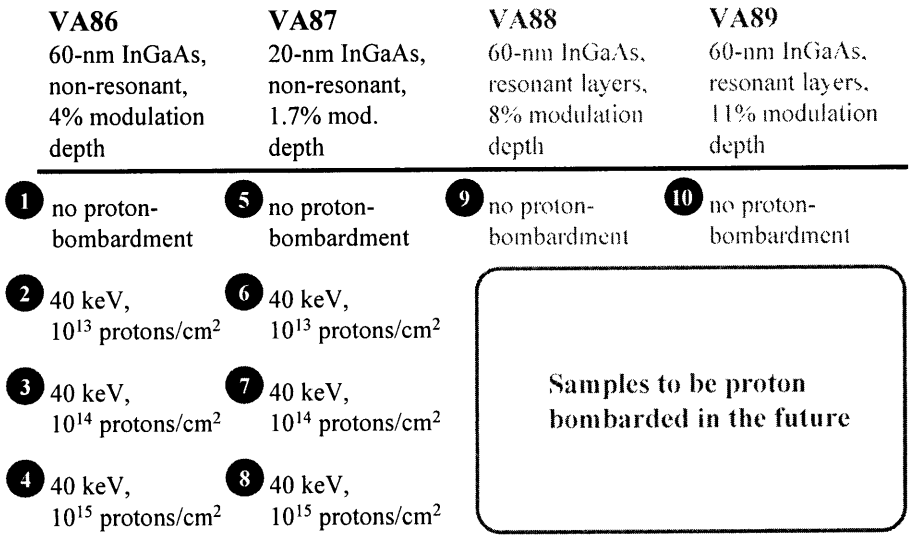

Figure 3.16 Summary of SBR samples fabricated and designed for use in high-repetition-rate lasers. VA88 and VA89 have not yet been proton bombarded, but will be in the future, with the dosage scheme outlined later in Figure 3.24.

3.4.3 Preliminary Experimental Results

The recovery dynamics of proton bombarded samples of VA86 have been measured by Ali Motamedi, who kindly provided the data in the following figures showing preliminary pump-probe results. Pump-probe traces for VA86 samples at a fluence of 40 μJ/cm^2 with no proton bombardment, bombardment with 40 keV protons at 10^{13} protons/cm^2, and bombardment with 40 keV protons at 10^{14} protons/cm^2 dosage are shown in Figure 3.17. The equivalent traces at 160 μJ/cm^2 are shown in Figure 3.18. Both sets of data indicate the effectiveness of the proton bombardment via the reduced recovery times. The falloff in absorption is significantly faster for the 10^{14} protons/cm^2-bombarded sample compared to the non-bombarded sample. Estimates of the fast and slow time constants of the absorber were made by fitting the measured pump-probe traces to a simple model with two exponential time constants. A summary of the results from Ali is shown in Figure 3.19.

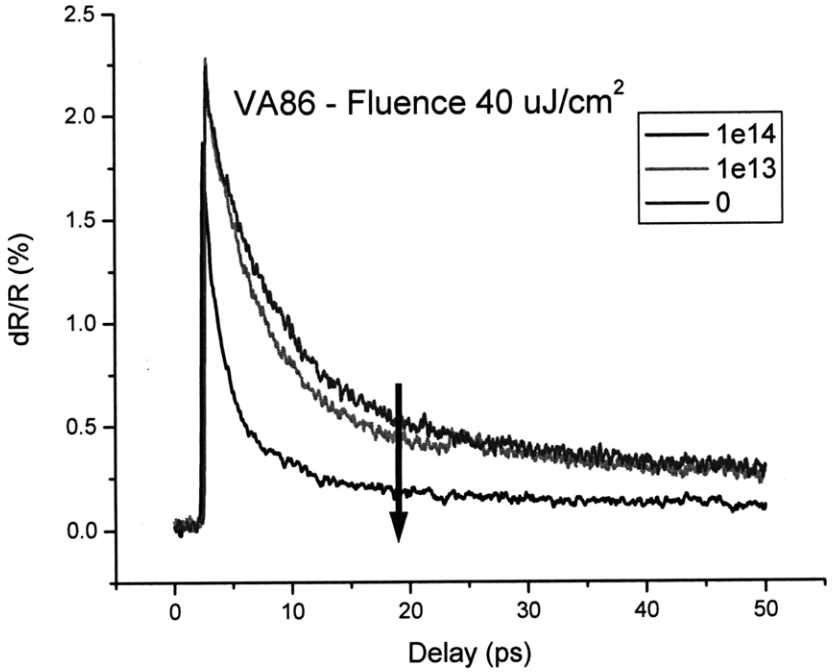

Figure 3.17 Pump-probe traces of VA86 for different proton bombardment levels at a pump fluence of 40 μJ/cm^2. Data courtesy of Ali Motamedi.

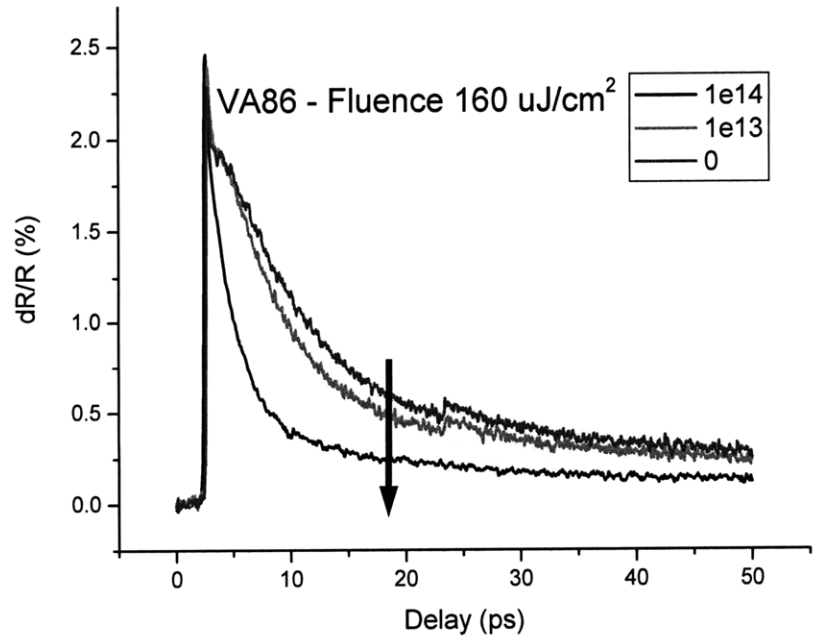

Figure 3.18 Pump-probe traces of VA86 for different proton bombardment levels at a pump fluence of 160 μJ/cm^2. Data courtesy of Ali Motamedi.

	Fluence = 40 μJ/cm²		160 μJ/cm²		640 μJ/cm²	
Units in ps	τ_{fast}	τ_{slow}	τ_{fast}	τ_{slow}	τ_{fast}	τ_{slow}
No proton-bombardment	6.0	6.0	6.5	67	7.8	61
10^{13} protons/cm²	4.3	63	5.1	59	6.1	61
10^{14} protons/cm²	2.1	43	2.4	40	3.6	53

Figure 3.19 Summary of pump-probe measurements and fitted time constants approximating the fast and slow components of the InGaAs saturable absorber recovery dynamics. Units in picoseconds. Data courtesy of Ali Motamedi.

Typical recovery times corresponding to the slow time constant for VA86 samples are ~70 ps for the un-bombarded samples, ~60 ps for the 10^{13} protons/cm^2 samples, and ~50 ps for the 10^{14} protons/cm^2 samples. These recovery times decrease with increasing proton bombardment levels, allowing the absorber to recover from bleaching faster after each successive pulse.

In the short cavity of a multi-gigahertz laser, KLM is not very effective. As a result, the absorber needs to play a significant role in pulse shaping. The fast time constant indicated in the table in Figure 3.19 provides this effect. Not only does the recovery time corresponding to the slow time constant compress with increasing proton bombardment, so too does the fast time constant. This means samples with high proton bombardment levels should also help generate shorter pulses.

Finally, by combining the pump-probe traces for a number of different pump fluences, Ali was able to construct the nonlinear reflectivity curve for VA86 samples bombarded 40 keV protons at 10^{14} protons/cm^2. This is shown below in Figure 3.20. By fitting this curve, Ali determined the saturation fluence to be approximately 18 μJ/cm^2, which is relatively low and ideal for high-repetition-rate lasers given our aversion to Q-switched modelocking.

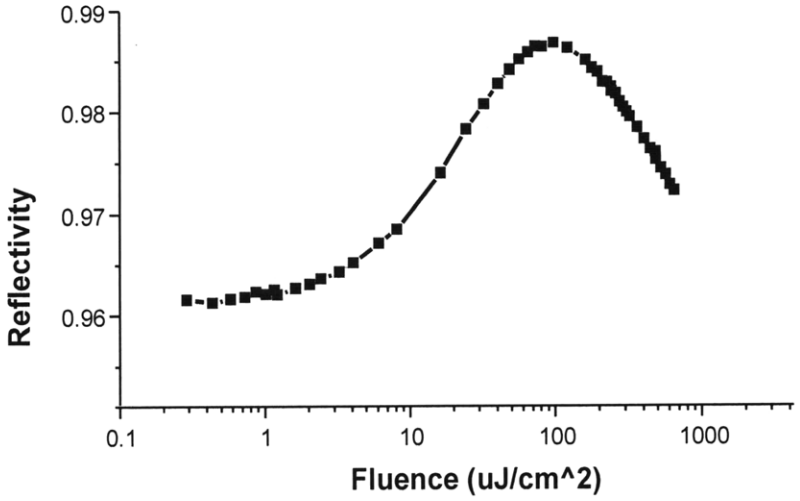

Figure 3.20 Measured nonlinear reflectivity curve of VA86 samples proton bombarded with 40 keV protons at 10^{14} protons/cm^2. Data courtesy of Ali Motamedi.

Initial laser testing of the VA86 and VA87 samples were performed in an erbium-doped fiber laser by Hyunil Byun and Michelle Sander. Passively modelocked Er:-doped fiber lasers represent a straightforward way to directly generate a high repetition rate pulse train in the telecom C-band. The pulse generation is passive, therefore no high frequency electronics are required.

The VA86 and VA87 SBRs were tested in the laser setup shown below in Figure 3.21. The laser cavity consists of erbium-doped fiber spliced to single-mode fiber, the length of which is butt-coupled to the SBR on one end and the output coupler on the other end. The SMF was spliced on so that the heated EDF would not be in contact with the SBR, in hopes of minimizing thermal damage.

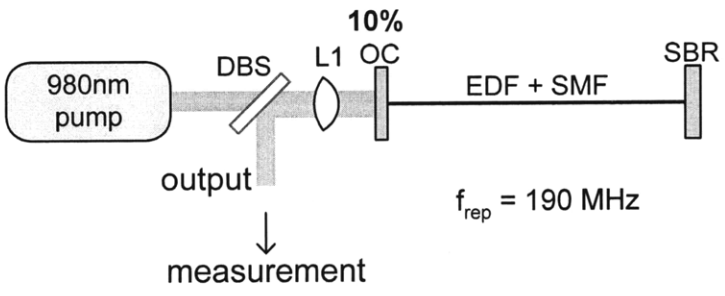

Figure 3.21 Schematic of erbium-doped fiber laser setup. Courtesy of H. Byun.

Modelocked operation was achieved with both VA86 and VA87. However, because of its low modulation depth (1.7%), relatively weak and unstable modelocking was observed with VA87, and the focus of laser testing was turned to VA86. Fundamental modelocking of the EDF laser was achieved with VA86 for all four levels of proton bombardment (classes 1–4 in Figure 3.16 above). Laser performance with VA86 is summarized in Figure 3.22. Hyunil Byun generously provided the chart.

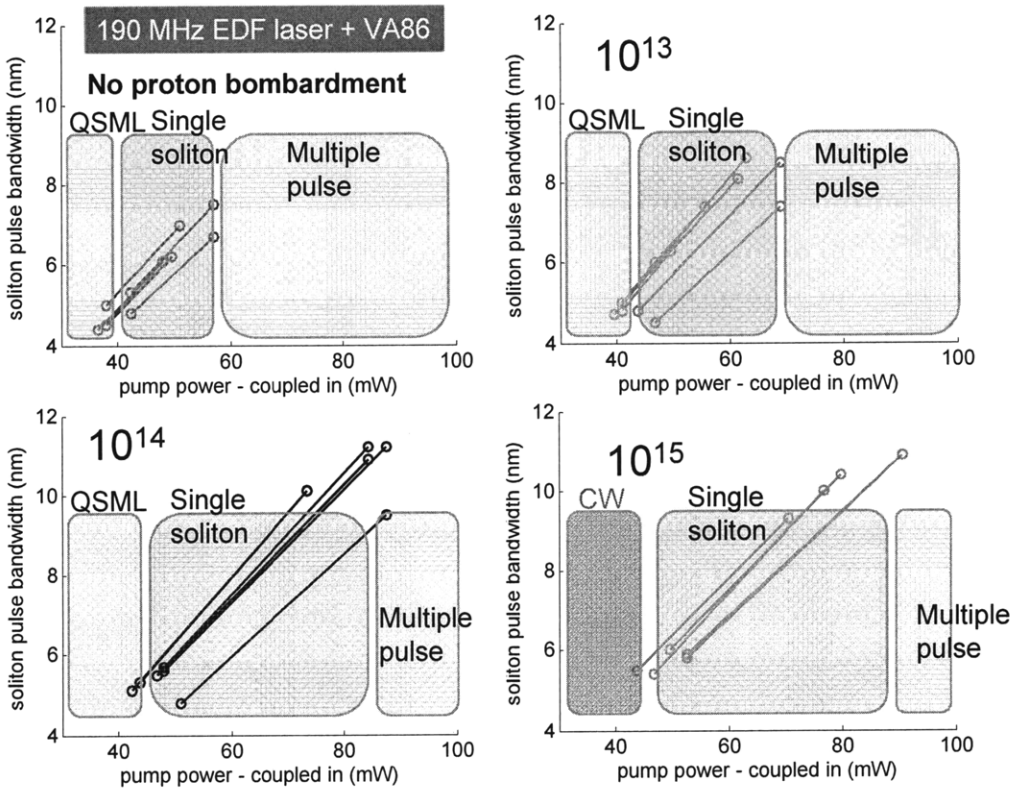

Figure 3.22 Modelocking stability range for the erbium-doped fiber laser using VA86 SBR samples of various proton bombardment levels. Samples bombarded at 10^{14}/cm^2 performed the best. Data courtesy of H. Byun.

Of the four classes, samples bombarded with 40 keV protons at 10^{14} protons/cm^2 performed the best, exhibiting the greatest operating range. Pulse widths of 250 fs were estimated from FWHM bandwidths of ~12 nm at the 10^{14} protons/cm^2 bombardment level. Except for the 10^{15} dosage samples, all the samples went through a clear Q-switched modelocking regime at low pump powers, before fundamental modelocking was achieved. As pump power was increased further, the onset of multiple pulsing was observed. For the

10^{15} dosage samples, no Q-switched modelocking was observed, however, cw lasing continued at relatively high pump powers before fundamental modelocking was achieved.

As expected, performance improved with greater proton bombardment, up to a point. Reduced recovery time, both fast and slow time constants, coupled with operation many times above the saturation fluence led to stable modelocking and shorter pulses. In the case of proton bombardment at the 10^{15} protons/cm^2 dosage, performance was likely hindered by the increased non-saturable loss and reduced modulation depth associated with over-bombardment. As a result, future post-growth processing should likely center around proton bombardment at the 10^{14} protons/cm^2 level.

3.4.4 Proton Bombardment of VA88 and VA89

For thicker absorbing layers, or for absorbers that are deep in a structure where two-photon absorption in the over-layers needs to be taken into consideration, more complex dosage schedules are required to penetrate the additional material and deposit uniform defects throughout the target region. At that point, the TPA lifetime in the otherwise transparent over-layers that precede the absorber can become significant factors with the relatively high intensity light in those sections of the standing wave pattern. (This was part of the rationale for the design of VA87 – to reduce the material on top of the absorber.)

At this point though, it becomes a game of compromise, because significant amounts of proton bombardment also introduce changes in loss – more non-saturable loss as well as less saturable loss, both of which are bad for modelocking. Proton bombardment is a discreet step. With annealing, you can nullify the deleterious effects of proton bombardment slightly. Therefore, annealing is a fine tuning mechanism that should be leveraged. Back to the problem, though, the point is that the SBR designer needs to find a medium between enough proton bombardment so that you achieve the lifetime reduction required for high-repetition-rate operation, and not too much, to the point that the lasing efficiency is impeded, or there is not enough saturable loss for sufficient modelocking force. Ultimately, this will be an empirical exercise, to test different dosage schemes in a laser, and then iterate to find the optimal solution.

In our case, the relevant structures in this discussion are VA88 and VA89 – the SBRs designed with extra resonant layers for enhanced modulation depths. Given the relatively high non-saturable losses of the Er-doped fiber laser and the high gain, SBRs with large modulation depths would be preferred.

In order to deposit a uniform damage profile throughout a thickness, a superposition of suitably weighted proton beams of different energies can be used. The result, termed a spread-out Bragg peak, is illustrated in the Figure 3.23 below.

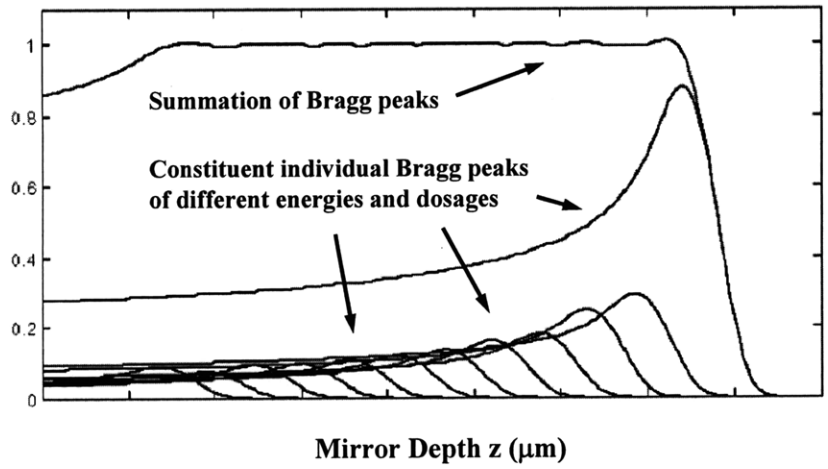

Figure 3.23 Illustrative figure of a spread-out Bragg peak for uniform proton bombardment.

Dosage Schedule	Energy keV	Dose protons/cm^2
1	200	1×10^{13}
	150	4×10^{12}
	100	2×10^{12}
	40	1×10^{12}
2	200	1×10^{14}
	150	4×10^{13}
	100	2×10^{13}
	40	1×10^{13}

Figure 3.24 Recommended proton bombardment schedules for the VA88 and VA89 high-repetition-rate-laser SBRs.

For VA88 and VA89, the proposed dosage schedules are outlined above in Figure 3.24. Given the experience with the 10^{15} dosage in the EDF laser testing, we exclude it from the VA88 and VA89 runs. These schedules were constructed based on empirical data from TRIM, and from consultations with Joe Donnelly and Juliet Gopinath at Lincoln Laboratories.

In addition to the execution of the proton bombardment schedules in Figure 3.24, there are additional investigations that can be performed in terms of optimizing the recovery times of these SBR structures, together with the work on dispersion in the next section. For example, we may want to explore using oxidized base mirrors to minimize light penetration deeper into the SBR structure to minimize TPA lifetime limiting pulse widths. These ideas for future work will be covered in the Conclusion.

3.5 INTEGRATION OF DISPERSION COMPENSATION

Dispersion compensation is a ubiquitous challenge in femtosecond pulse generation in that it always limits advances towards shorter pulse durations. Group delay dispersion (GDD) naturally arises from any optical material in the laser system, including air paths, and tends to significantly lengthen short optical pulses. The goal then is to find a dispersion compensation scheme that can deliver adjustable dispersion over a broad bandwidth, and is simple and compact. Traditionally, this problem has been solved with bulk dispersion compensators or prism or grating sequences. The latter techniques could compensate for large amounts of material dispersion. However, when it comes to really short pulse durations in the sub-100 fs regime, these traditional approaches are limited by higher-order dispersion. Furthermore, bulk and geometrical compensators are difficult to incorporate into compact high-repetition-rate lasers and also cannot be integrated into fiber lasers.

Using optical fibers for dispersion compensation is an alternative approach. Fiber dispersion properties are determined by their material and waveguide dispersion. Material dispersion can be slightly changed by adjusting the fiber composition, whereas waveguide dispersion is determined by the fiber core-cladding geometry. Figure 3.25 shows the characteristic curves for some typical dispersive fibers. Dispersion-shifted fibers behave like standard fibers, except their zero-dispersion wavelength is shifted to 1550 nm. Dispersion-flattened fibers have a low and very constant dispersion over a broad wavelength range. Dispersion-compensating fibers have the opposite slope from that of standard fiber in the dispersion wavelength. As a technique, dispersion compensation

using fibers is very convenient to implement. However rather long fibers are required and significant nonlinear effects can be introduced that limit their application.

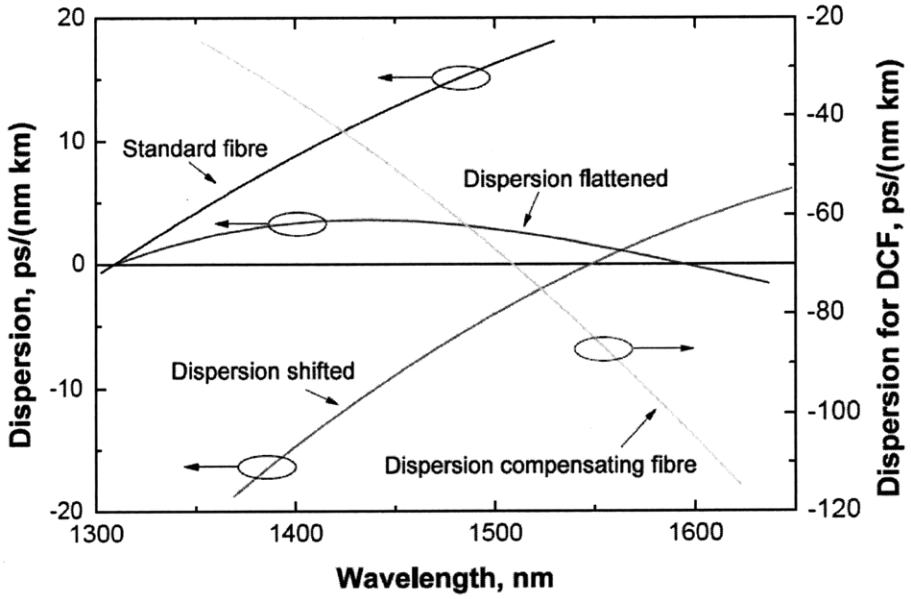

Figure 3.25 Dispersion curves for standard, dispersion-shifted, dispersion-flattened, and dispersion-compensating fibers [28].

With the introduction of chirped mirror technology, progress in the generation of ultrashort pulses was significantly advanced. By progressively varying the Bragg wavelength along the z-dimension of a high- and low-index mirror stack, a structure can be designed to exhibit not only a very broad optical bandwidth, but also a large dispersion compensating bandwidth. A typical structure is illustrated in Figure 3.26. The major benefits of this technology have been low losses, large operating and compensating bandwidth, and a compact integrated configuration. The drawbacks, however, are the complex computer optimization codes required to design the mirrors and the expensive equipment and processes required to fabricate the devices.

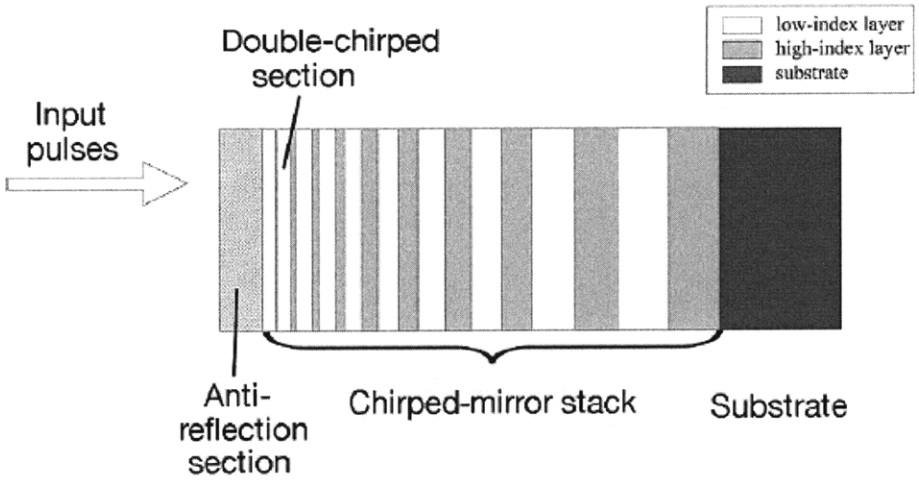

Figure 3.26 Schematic of a double-chirped mirror. The mirror consists of alternating layers of low- and high-index materials, with a variation of the Bragg wavelength along the stack. Longer wavelengths penetrate deeper into the structure relative to shorter wavelengths, hence creating group delay and group delay dispersion. Satellite pulses are suppressed by impedance matching within the mirror stack and at the interface with air.

In addition to dispersion-compensating mirrors, gratings pairs, and prism pairs, reflection from thin-film multilayer interferometers represent yet another technique for femtosecond pulse compression. The utilization of the dispersive properties of interferometers for optical pulse compression was first investigated by Gires and Tournois in 1964 [29]. The striking property of these interferometers is that the optical phase shift is wavelength dependent, while the reflectivity, in contrast to the usual Fabry-Perot interferometer, remains constantly high over a broad spectral bandwidth. The typical interferometric resonant behavior shows up in the phase delay. The thin-film variant of the Gires-Tournois interferometer (GTI) can provide significant group delay dispersion, positive and negative, for bandwidths of tens of nanometers. If only a few nanometers of dispersion compensation bandwidth are required, group delay dispersions of thousands of fs^2 can be produced by these devices.

Such GTI mirrors had been used for intracavity dispersion compensation as early as 1969, decades before the development of chirped mirrors [30]. In more recent work, these GTI devices have been combined with saturable absorber mirrors into one monolithic semiconductor structure capable of providing all-in-one modelocking and dispersion compensation. Such a device was demonstrated for a Cr:LiSAF laser generating 160 fs pulses [31]. The GTI-SBR exhibited –400 fs^2 dispersion compensation over a ~20-nm

bandwidth. More recent designs have demonstrated negative dispersions of several 1000 fs^2 and have incorporated gain into the GTI device [32].

The standard configuration of the Gires-Tournois interferometer (GTI) is similar to the one already used in the previous discussion for resonant coatings, and is re-shown below in Figure 3.27 with slight modifications.

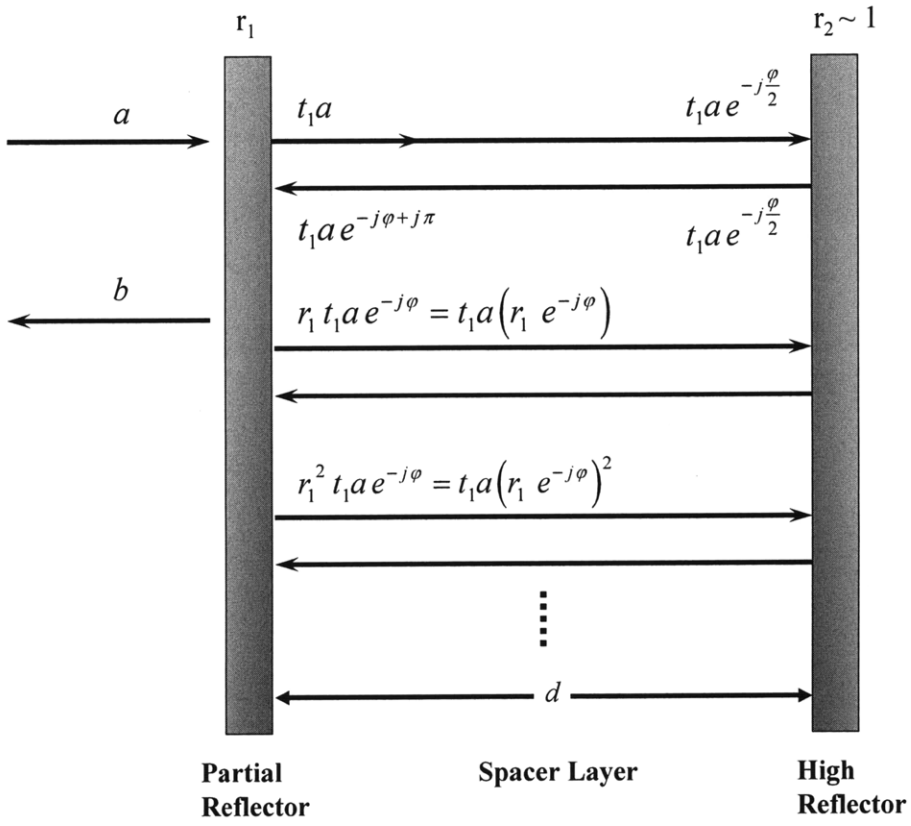

Figure 3.27 Schematic of a GTI-SBR structure. Traveling waves inside the cavity and their equations are depicted to illustrate the basic physics of the structure.

The GTI consists of two plane mirrors, flanking a spacer layer of thickness d. Again, r_2 is a highly reflective mirror (the Bragg stack of the SBR) whose reflectivity we'll simplify and approximate as unity. And the partially reflective mirror on the left has field reflection coefficient r_1, which we'll simply refer to as r. For now, to simplify the discussion, we do not include the effect of the absorber located within the spacer layer, and will wait to incorporate that component later in our treatment. Intuitively, if this SBR were to be used to self-start KLM, this initial simplification makes sense, since it reflects what the situation

would be otherwise. The absorber bleaches under KLM operation and its loss characteristic would not be relevant at steady state. Once we have built our intuition of the lossless GTI, we can then overlay the effect of the absorber and establish the more general solution.

As before, the light incident upon this structure is pulsed, not continuous. We need to keep in mind the conditions for the simplifying assumption of using cw waves to analyze the GTI response – $t_p >> t_{RT}$. That is, the pulse widths are long enough so that successive pulses from the interferometer do temporally overlap and interfere. The response of the interferometer otherwise will just be a train of pulses with rapidly decreasing amplitude. With the condition $t_p >> t_{RT}$ satisfactorily fulfilled, we can proceed with the cw analysis. (Note that the intermediate case where $t_p = t_{RT}$ cannot be treated analytically.)

Again, the incident field with amplitude a approaches the GTI from the left. Note that earlier with the resonant coating layers, the discussion centered on the field inside the spacer layer. For the GTI discussion here, we focus on the reflected field b that comes back out from the device, from right to left. Building on the math we already carried out for resonant coatings, we see that reflected field amplitude b can be represented as:

$$b = \left(-r + \left(1 - r^2\right)^{\frac{1}{2}} \times \left(\frac{1}{1 - re^{-J\varphi}} \right) e^{-J\varphi} \times \left(1 - r^2\right)^{\frac{1}{2}} \right) a = \left(-r + \left(1 - r^2\right) \times \frac{e^{-J\varphi}}{1 - re^{-J\varphi}} \right) a \qquad (3.7)$$

In the expression, we simply account for the first-order reflection from the front surface with $-r$. Then, for the subsequent exiting pulse train, we add onto the expression for the field inside the spacer layer – Equation (3.3): the transmission coefficient for going through the partial reflector, a roundtrip phase accumulation, and then the transmission coefficient coming back out. Here, with r^2 being the reflectivity; and t defined as the field transmission coefficient, we have $r^2 + t^2 = 1$ by energy conservation. And the transmission coefficient t is:

$$t = \left(1 - r^2\right)^{\frac{1}{2}} \qquad (3.8)$$

Multiplying through, we get:

$$b = \frac{-r + e^{-J\varphi}}{1 - re^{-J\varphi}} a \qquad (3.9)$$

The reflection coefficient from the device r_{GTI} is b/a, and you can easily see that device reflectivity $|r_{GTI}|^2 = 1$, independent of the phase φ. Defining the nonlinear phase shift Φ for the device by

$$b \equiv e^{-j\Phi} a \tag{3.10}$$

We multiply through to get:

$$e^{-j\Phi} = \frac{-r + e^{-j\varphi}}{1 - re^{-j\varphi}} \times \frac{1 - re^{+j\varphi}}{1 - re^{+j\varphi}} \tag{3.11}$$

$$= \frac{-2r + e^{-j\varphi} + r^2 e^{+j\varphi}}{1 + r^2 - 2r\cos\varphi}$$

$$= \frac{\left[\left(1 + r^2\right)\cos\varphi - 2r\right] + j\left[\left(-1 + r^2\right)\sin\varphi\right]}{1 + r^2 - 2r\cos\varphi}$$

From Euler's formula, we find the expression for the nonlinear phase shift of the GTI:

$$\tan\Phi = -\frac{imag\left(e^{-j\Phi}\right)}{real\left(e^{-j\Phi}\right)} = \frac{\left(r^2 - 1\right)\sin\varphi}{2r - \left(1 + r^2\right)\cos\varphi} \tag{3.12}$$

Using the standard definitions for group delay, group delay dispersion and the appropriate differentials,

$$T_g \equiv \frac{\partial\varphi}{\partial\omega} \qquad GDD \equiv \frac{\partial^2\varphi}{\partial\omega^2} \qquad \frac{\partial}{\partial\omega} = -\frac{\lambda^2}{2\pi c}\frac{\partial}{\partial\lambda} \tag{3.13}$$

we get:

$$T_g = \frac{1 - r^2}{1 + r^2 - 2r\cos\left(\frac{4\pi n d}{\lambda}\right)} \times \frac{2nd}{c} \tag{3.14}$$

$$GDD = -\frac{\left(1-r^2\right)\times 2r\sin\left(\frac{4\pi nd}{\lambda}\right)}{\left[1+r^2-2r\cos\left(\frac{4\pi nd}{\lambda}\right)\right]^2}\times\left(\frac{2nd}{c}\right)^2 \tag{3.15}$$

As you can see from Equations (3.14) and (3.15), the key design parameters for the lossless GTI are the reflectivity of the top mirror r and the thickness of the spacer layer d. The GDD can be both positive and negative, and the amount can be tuned by changing the length of the GTI cavity d and the reflection coefficient r of the top mirror. For a selected resonance wavelength λ_{GTI}, the thickness d is a multiple of $\lambda_{GTI}/2n$, where n is the refractive index of spacer layer material. The resonance wavelength of the GTI λ_{GTI} should located within the stopband of the highly reflective base mirror (the Bragg stack of the SBR), and need not correspond to the center wavelength λ_c of the base mirror.

Group delay profiles for different orders of the fundamental cavity thickness $d = \lambda_{GTI}/2n$ are plotted in Figure 3.28 (a). As you increase the wavelength, the group delay first increases, indicating negative GDD, and then decreases with wavelength, indicating positive GDD. The corresponding group delay dispersion profiles are plotted and Figure 3.28 (b). The plots show profiles for different GTI cavity thicknesses d of 3 ($\lambda_{GTI}/2$), 4 ($\lambda_{GTI}/2$) and 5 ($\lambda_{GTI}/2$), where λ_{GTI} is the resonance wavelength of the GTI and equals 1.5 μm.

As you can see, the thicker the spacer layer in Figure 3.27, the greater the maximum dispersion value. The effective bandwidth of the designed dispersion changes as well, though primarily, it varies with the amount of dispersion. The greater the dispersion, the more quickly it falls off from the maximum, and hence, the narrower the usable bandwidth for that dispersion. You can also see that for greater dispersions, the peak dispersion also moves closer to the resonance wavelength. We need to keep these effects in mind when designing a GTI – the amount of dispersion, the usable bandwidth, and the location of the usable dispersion are all inter-dependent and move together. Ultimately, the implementation challenge for ultrashort pulse generation will not be the magnitude of the dispersion (most likely, it will be sufficient) but the usable bandwidth over which the dispersion can be maintained. For sub-100-fs pulses, the rate at which the dispersion falls off will play a significant role, and a more thorough investigation through simulation of the temporal dynamics will be required.

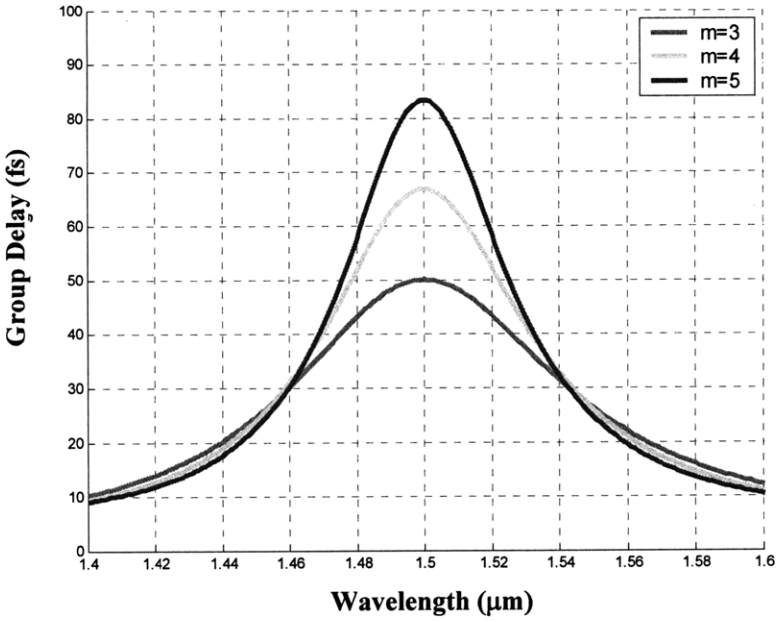

(a)

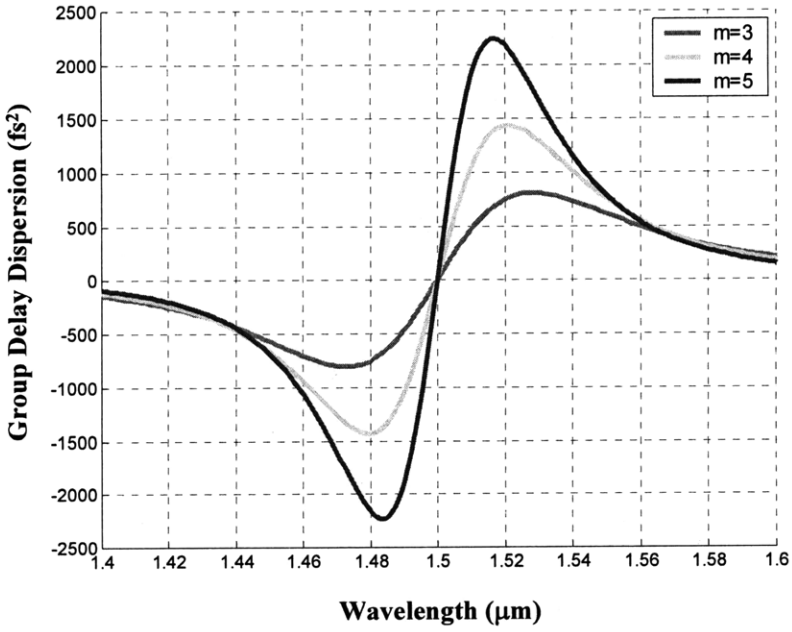

(b)

Figure 3.28 (a) Group delay and (b) group delay dispersion versus wavelength for a Gire Tournois interferometer. Profiles shown for different spacer layer thicknesses of 3 $\lambda_{GTI}/2$, 4 $\lambda_{GTI}/2$ and 5 $\lambda_{GTI}/2$, where λ_{GTI} is the resonance wavelength of the GTI. Here, λ_{GTI} = 1.5 μm. As thickness *d* increases, the dispersion increases.

The other parameter that can influence the group delay dispersion is the reflectivity of the top partially reflecting mirror, which is related to r in Equation (3.15). As you increase the reflectivity, the dispersion increases and the usable bandwidth decreases. The effect of varying the reflectivity is shown in Figures 3.29. Changing r results in a similar trend to Figures 3.28 earlier, implying you have two routes that can produce the same result – either grow a thicker spacer layer, or increase the top mirror reflectivity (e.g. with additional coatings such as the resonant coatings described earlier).

There may be practical limitations that restrict the method used. For example, recalling the earlier condition for using the cw analysis, the spacer layer cannot be overly thick to the point where the roundtrip transit time approaches the pulse width of the laser. Two-photon absorption may become an issue as well in a thick layer of material, inhibiting modelocking. Finally, there may be fabrication issues with growing a very thick layer of material with MBE. The alternative approach of growing additional resonant coatings to enhance the top mirror reflectivity adds complexity to the fabrication process, which may result in delamination and other structural instabilities, and, most certainly, additional non-saturable loss due to the additional material interfaces. A way to avoid this would be to use a higher-index material for the spacer layer and avoid additional top-mirror coatings altogether. All said, these challenges can be overcome, and, compared to chirped mirrors, GTI's are still relatively simple to fabricate.

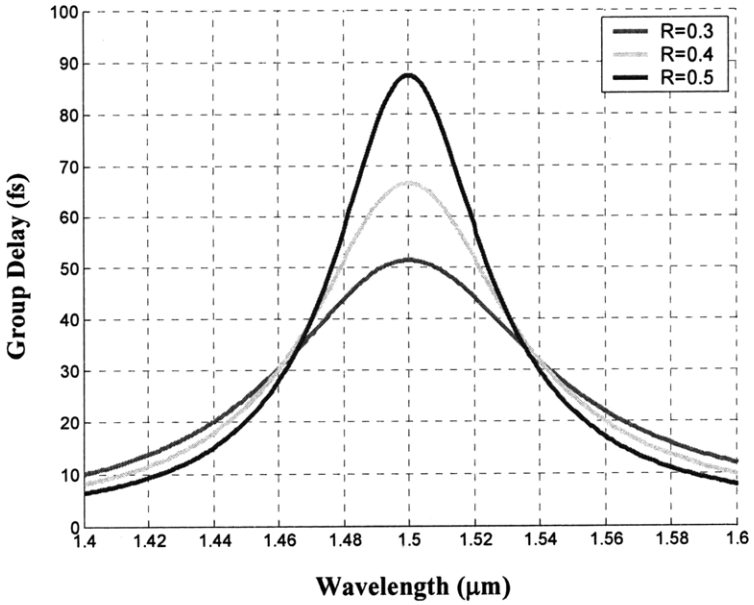

(a)

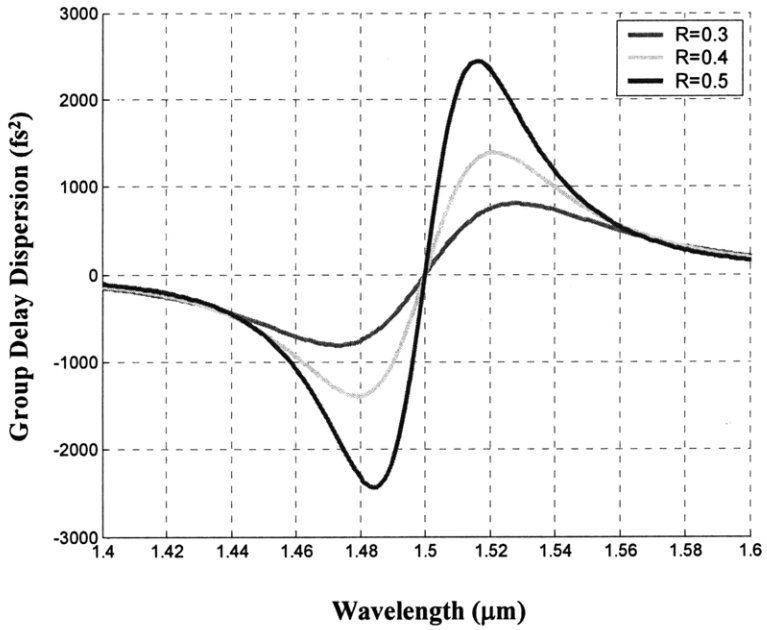

(b)

Figure 3.29 (a) Group delay and (b) group delay dispersion versus wavelength for a GTI, for different top mirror reflectivities R = r^2 of 30%, 40% and 50%. As R increases, the dispersion increases.

The analysis above does not change materially when we incorporate loss into the discussion. When you add a saturable absorber inside the spacer layer, the structure becomes similar to the absorber-cladding section of the SBR designs shown earlier in Chapter 2. The position of the saturable absorber inside the cladding layer in the more general absorptive GTI structure becomes another design parameter that affects the dispersion profile.

The initial intuitive preference would be to place the saturable absorber at a peak in the electric field standing wave pattern, as depicted in Figure 3.30 (a). However, this would effect a pronounced absorption resonance at λ_{GTI}, and the extra loss could push the lasing wavelength away from the desired compensating dispersion wavelength regime, towards one of the reflection maxima, as shown in Figure 3.31. As a result, we prefer placing the absorber layer close to a trough in the standing wave pattern, as in Figure 3.30 (b). The associated dispersion and reflectivity profiles are shown in Figure 3.32. Keep in mind, for structures with low resonance, placing the absorber at a peak may be acceptable. As always, judgment is left to the designer and experimenters in striking the best compromise.

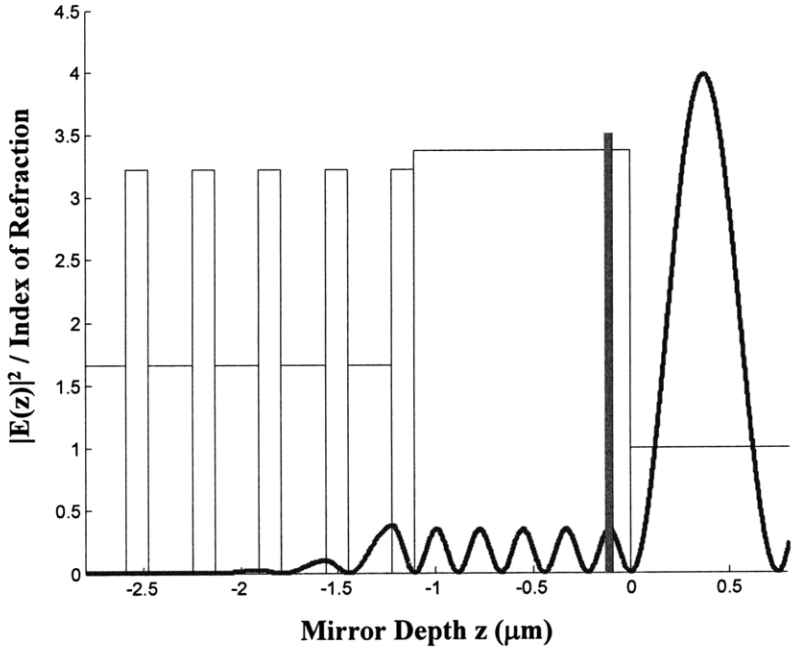

(a)

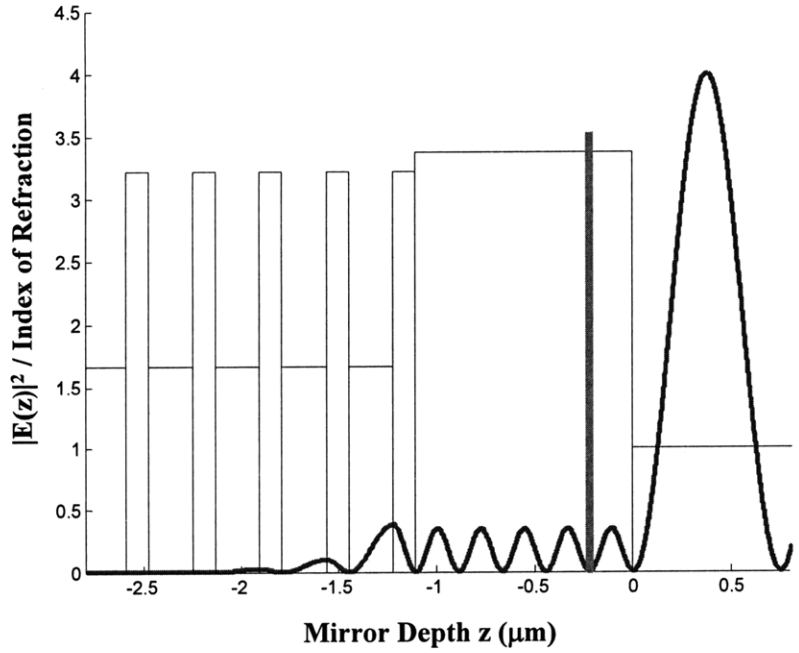

(b)

Figure 3.30 GTI-SBR structure designs with saturable absorber (red highlighted section) placed at a peak (a) and at a trough (b) of the electric field standing wave pattern.

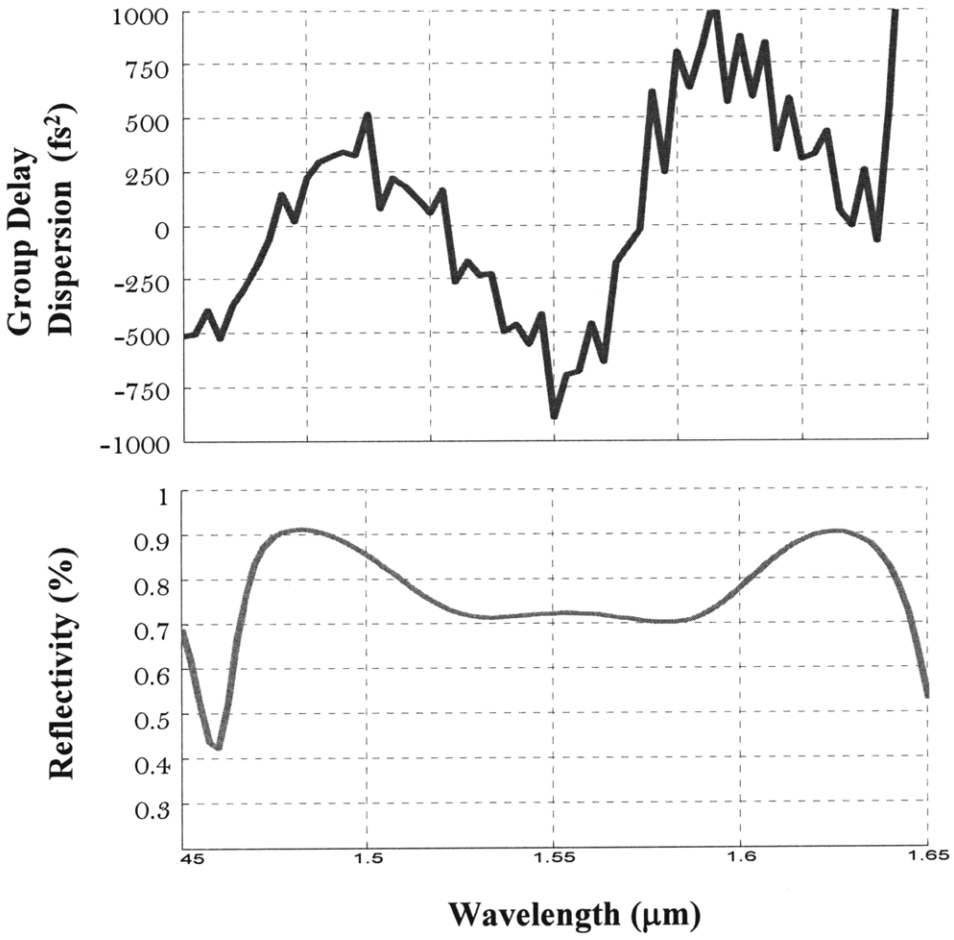

Figure 3.31 Calculated reflectivity and dispersion of a GTI-SBR, corresponding to the structure shown in Figure 3.30 (a) with the saturable absorber placed near a peak in the electric field standing wave pattern.

As you can see in Figure 3.31, the modulation depth at 1.55 μm, which corresponds to the operating wavelength of the erbium-doped fiber laser, is quite high when the absorber is placed in a peak of the electric field standing wave pattern. As a result, lasing will likely trend towards the higher reflectivities on either side of 1.55 μm, away from the desired anomalous dispersion range. When the absorber is shifted, the resulting reflectivity at 1.55 μm is significantly improved from 72% to 91% at 1.55 μm. As a result, lasing is preferred at the intended wavelength, and, in addition, the pulse experiences the designed anomalous dispersion. The dispersion peaking at -750 fs^2 is quite high and has a relatively narrow bandwidth. This bandwidth however does cover the operating range for the erbium-doped fiber laser, which typically achieves 10-15 nm FWHM bandwidth.

The jagged-ness of the calculated dispersion profiles is the result of a limited material data set. Because the refractive indices used are drawn from empirical data, there is a lack of smoothness when the mirror code calculates the group delay dispersion via differentials.

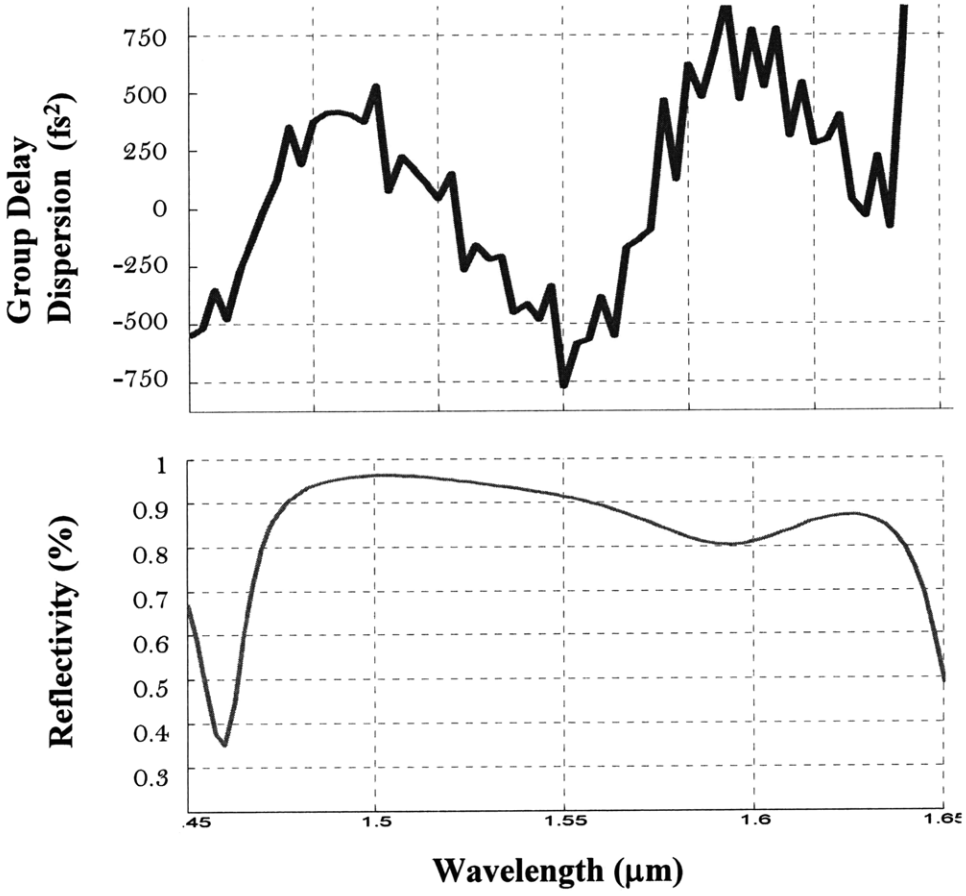

Figure 3.32 Calculated reflectivity and dispersion of GTI-SBR1, corresponding to the structure shown in Figure 3.30 (b) with the saturable absorber placed near a trough in the electric field standing wave pattern.

The structure shown in Figure 3.30 (b) and its corresponding dispersion and reflectivity profiles is our first proposed GTI-SBR design – GTI-SBR1. This design uses a 60-nm $In_{0.537}Ga_{0.463}As$ absorber placed in a $3 \times \lambda/2$-thick GaAs cladding layer to achieve the necessary dispersion for use in our lasers. The base mirror is the same 22-layer-pair $GaAs/Al_{0.95}Ga_{0.05}As$ quarter-wave stack used earlier for the VA86 series of SBRs.

As mentioned before, the alternative route to achieve a desired compensating dispersion would be to increase the top-mirror reflectivity, and that is the basis of the design for GTI-

SBR2. By adding quarter-wave layer pairs on top of the GaAs cladding layer, we can enhance the reflectivity of the partial reflector of the GTI cavity. The GTI-SBR2 structure is shown in Figure 3.33 and its calculated reflectivity and group delay dispersion are shown in Figure 3.34. The structure is analogous to VA88, except the GaAs cladding layer is thicker at $2 \times \lambda/2$. The same 3-layer-pair overgrowth of AlGaAs/GaAs is used, with the top most layer being $Al_{0.50}Ga_{0.50}As$, and the other low-index layers being $Al_{0.95}Ga_{0.05}As$. The thicknesses of these layers are the same as for VA88, as shown in Figure 3.7. The absorber has been shifted in the cladding layer to a trough location in the standing wave pattern for the laser center wavelength at 1.55 μm. The GaAs cladding layers are 130 nm and 280 nm thick.

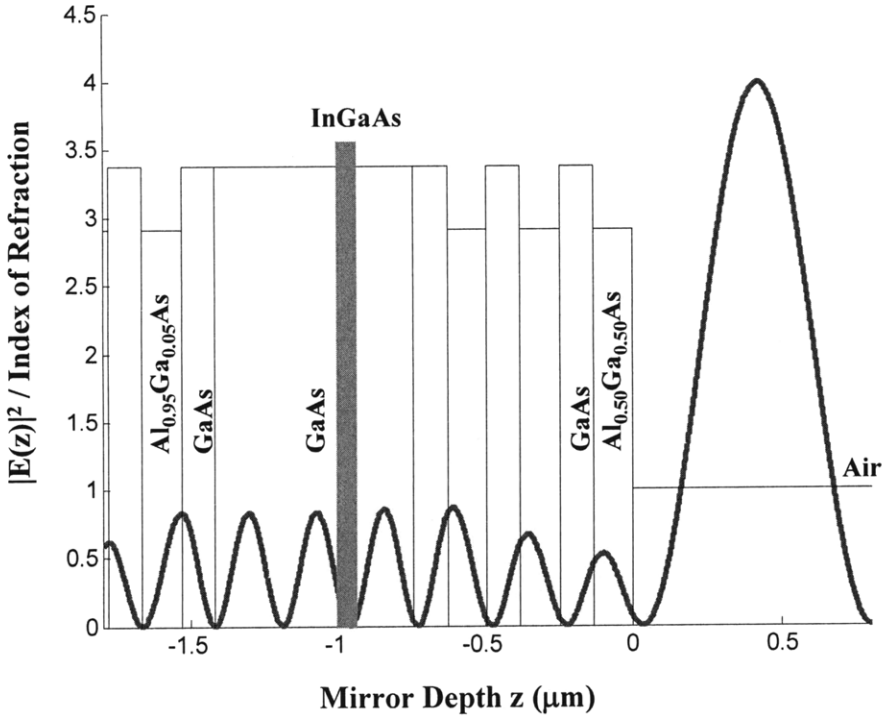

Figure 3.33 Schematic of GTI-SBR2 design structure.

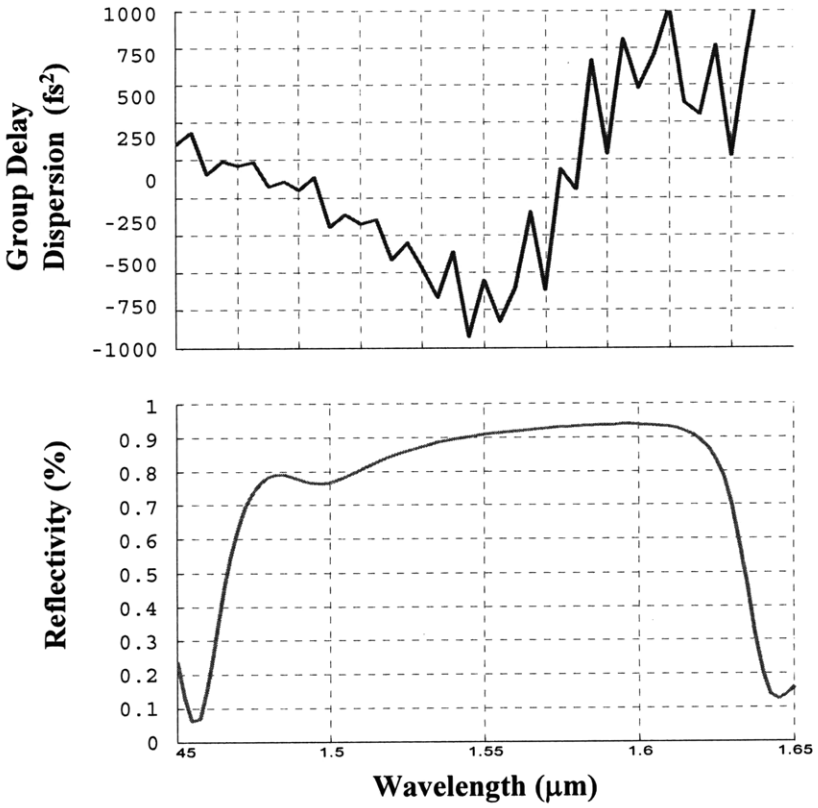

Figure 3.34 Calculated reflectivity and dispersion of GTI-SBR2.

Both of these structures will likely need proton bombardment, given the large amount of material present before incident light reaches the absorber. Lifetime reduction of TPA in the overgrowth layers, as well as in the absorber layer, will be required and could be done with a dosage schedule similar to the ones in Figure 3.24.

Fabrication of these structures and subsequent testing in lasers have not yet occurred at the time of this writing. When these structures are fabricated, care must be taken to protect the surface of the mirror, given the relatively high intensities at the air-semiconductor interface prevalent with these designs. Heat-sinking, as well as additional coating layers to reflect pump light, may be required.

Given the push for high repetition rates *and* femtosecond pulses at MIT, however, it is inevitable that GTI structures will be incorporated into lasers and experimented with extensively. There are in fact several interesting opportunities for analysis that can be further pursued.

In terms of design, three additional structures come to mind that should be explored further. First, as mentioned earlier, oxidized mirrors should be considered. Given their broad bandwidth, there is significant freedom in designing additional overlayers for the GTI or for resonant behavior. Additionally, because of the high-index contrast, light incident on such SBRs will not penetrate deep into the structure, avoiding the loss and long recovery time of TPA. Second, a simple chirped mirror may be interesting to investigate for these lasers. For octave-spanning lasers, the ripples in the dispersion profile prove detrimental to the generation of the shortest possible pulse widths. However, for pulses on the order of 100's of femtoseconds, a simple chirped mirror may prove sufficient. Integrating a saturable absorber on top of such a mirror would create another option for integrated saturable absorption and dispersion compensation. The final design to consider is the placement of multiple absorber layers of different thicknesses and band gaps. For example, one may consider placing one absorber at a trough location and another at a peak location in the electric field standing wave pattern. The absorbers would saturate at different fluences and provide another degree of freedom in designing the modelocking behavior of a laser.

For post-growth processing, there are additional paths to investigate more extensively as well. As discussed already, proton bombardment will largely be an empirical exercise, based on iterative attempts at finding an optimal dosage schedule. Irregardless, proton bombardment will be required for thick SBR structures – VA88, VA89, the GTI structures, as well as some of the other suggested designs above. Balance will always be needed between sufficient recovery time reduction and increases in the non-saturable loss. Along those lines, post-growth annealing should also be explored to fine tune the proton bombardment effects. Finally, the application of transparent dielectric coating on top of the SBR structures should be explored further. Given the possibility of thermal damage to the absorber, extensive heat-sinking and reflection of pump light will likely be required.

Finally, the development of a richer, more holistic simulation model may be needed to better understand laser dynamics when using these SBRs. A model that incorporates the temporal dynamics, as educated by pump-probe, as well as the spatial implications of the SBR structure and laser configuration may yield additional insight that could lead to improved modelocking performance.

REFERENCES

1. M. Saruwatari, "All optical signal processing for terabit/second optical transmission," IEEE Journal of Selected Topics in Quantum Electronics **6**, 1363 (2000).

2. P. W. Juodawlkis, J. C. Twichell, G. E. Betts, J. J. Hargreaves, R. D. Younger, J. L. Wasserman, F. J. O'Donnell, K. G. Ray, and R. C. Williamson, "Optically sampled analog-to-digital converters," IEEE Transactions on Microwave Theory and Techniques **49**, 1840 (2001).

3. S. Arahira, Y. Matsui and Y.Ogawa, "Mode-locking at very high repetition rates more than terahertz in passively mode-locked distributed-Bragg-reflector laser diodes," IEEE Journal of Quantum Electronics **32**, 1211 (1996).

4. R. Haring, R. Paschotta, A. Aschwanden, E. Gini, F. Morier-Genoud and U. Keller, "High-power passively mode-locked semiconductor lasers," IEEE Journal of Quantum Electronics **38**, 1268 (2002).

5. M. F. Becker, K. J. Kuizenga and A. E. Siegman, "Harmonic mode locking of the Nd:YAG laser," IEEE Journal of Quantum Electronics **QE-8**, 687 (1972).

6. L. Krainer, R. Paschotta, M. Moser and U. Keller, "77 GHz soliton modelocked Nd:YVO_4 laser," Electronics Letters **36**, 22 (2000).

7. C. Hönninger, R. Paschotta, F. Morier-Genoud, M. Moser, and U. Keller, "Q-switching stability limits of continuous-wave passive mode locking," JOSA B **16**, 46 (1999).

8. A. Oehler, T. Südmeyer, K. Weingarten and U. Keller, "100 GHz passively mode-locked Er:Yb:glass laser at 1.5 μm with 1.6-ps pulses," Optics Express **16**, 21930 (2008).

9. F. X. Kaertner, L. R. Brovelli, D. Kopf, M. Kamp, I. Calasso and U. Keller, "Control of solid-state laser dynamics by semiconductor devices," Optical Engineering **34**, 2024 (1995).

10. U. Keller, K. J. Weingarten, F. X. Kaertner, D. Kopf, B. Braun, I. D. Jung, R. Fluck, C. Honninger, N. Matuschek and J. Aus der Au, "Semiconductor saturable absorber mirrors (SESAM's) for femtosecond to nanosecond generation in solid state lasers," IEEE Journal of Selected Topics in Quantum Electronics **2**, 435 (1996).

11. M. J. Lederer, B. Luther-Davies, H. H. Tan and C. Jagadish, "An antiresonant Fabry-Perot saturable absorber for passive mode-locking fabricated by metal-organic vapor phase epitaxy and ion implantation design, characterization, and mode-locking," IEEE Journal of Quantum Electronics **34**, 2150 (1998).

12. F. Ganikhanov, G. Lin, W. Chen, C. S. Chang and C. Pan, "Subpicosecond carrier lifetimes in arsenic ion-implanted GaAs," Applied Physics Letters **67**, 3465 (1995).

13. Y. Silberberg, P. W. Smith, D. A. B. Miller, B. Tell, A. C. Gossard, and W. Wiegmann, "Fast nonlinear optical response from proton-bombarded multiple quantum well structures," Applied Physics Letters **46**, 701 (1985).

14. M. J. Lederer, B. Luther-Davies, H. H. Tan, C. Jagadish, M. Haiml, U. Siegner and U. Keller, "Nonlinear optical absorption and temporal response of arsenic- and oxygen-implanted GaAs," Applied Physics Letters **74**, 1993 (1999).

15. S. Collin, J. Ramos, J. Lopez, J. Mangeney and N. Stelmakh, "Optical sampling by ultra-fast high-contrast saturable absorber created by heavy ion irradiation," 1999 CLEO **35**, 1667 (1999).

16. P. M. Downey and B. Schwartz, "Picosecond response in $^{3}He^{+}$ bombarded InP photoconductors," Applied Physics Letters **44**, 207 (1984).

17. E. L. Delpon, J. L. Oudar, N. Bouche, R. Raj, A. Shen, N. Stelmakh and J. M. Lourtioz, "Ultrafast excitonic saturable absorption in ion-implanted InGaAs/InAlAs multiple quantum wells," Applied Physics Letters **72**,759 (1998).

18. J. F. Ziegler, *Ion Implantation Science and Technology*, Academic (1988).

19. J. T. Gopinath, E. R. Thoen, E. M. Koontz, M. E. Grein, L. A. Kolodziejski, and E. P. Ippen, "Recovery dynamics in proton-bombarded semiconductor saturable absorber mirrors," Applied Physics Letters **78**, 3409 (2001).

20. J. T. Gopinath, MS Thesis, MIT (2000).

21. S. M. Gulwadi, M. V. Rao, D. S. Simons. O. W. Holland, W.-P. Hong, C. Caneau, and H. B. Deitrich, Journal of Applied Physics **69**, 162 (1991).

22. F. E. Doany, D. Grischkowsky and C. C. Chi, "Carrier lifetime versus ion-implantation dose in silicon on sapphire," Applied Physics Letters **50**, 460 (1987).

23. M. Lambsdorff, J. Kuhl, J. Rosenzweig, A. Axmann and J. Schneider, "Subpicosecond carrier lifetimes in radiation-damaged GaAs," Applied Physics Letters **58**, 1881 (1991).

24. K. F. Lamprecht, S. Juen, L. Palmetshofer and R. A. Hopfel, "Ultrashort carrier lifetimes in H^{+} bombarded InP," Applied Physics Letters **59**, 926 (1991).

25. J. F. Ziegler, J. P. Biersack, and U. Littmark, *The Stopping and Range of Ions in Solids*, Pergamon Press (1985).

26. H. M. Shen, University of Michigan NERS315 Radiation Detection & Measurement notes.

27. Personal communications with Joe Donnelly at MIT Lincoln Laboratory.

28. H. Toda, K. Hamada, Y. Furukawa, Y. Kodama, and S. Seikai, "Experimental evaluation of Gordon-Haus timing jitter of dispersion managed solitons," ECOC '99 **1**, 406 (1999).

29. F. Gires and P. Tournois, "Interferometre utilizable pour la compression d'impulsions lumineuses modulees en frequence," C. R. Acad. Sci. Paris 258, 6112 (1964).

30. M. A. Duguay and J. W. Hansen, "Compression of pulses from a modelocked He-Ne laser," Applied Physics Letters **14**, 14 (1969).

31. D. Kopf, G. Zhang, R. Fluck, M. Moser and U. Keller, "All-in-one dispersion-compensating saturable absorber mirror for compact femtosecond laser sources," Optics Letters **21**, 486 (1996).

32. M. Moenster, U. Griebner, W. Richter and G. Steinmeyer, "Resonant saturable absorber mirrors for dispersion control in ultrafast lasers," IEEE Journal of Quantum Electronics **43**, 174 (2007).

Chapter 4

HIGHLY NONLINEAR BISMUTH-OXIDE FIBER FOR SUPERCONTINUUM AND ULTRASHORT PULSE GENERATION

4.1 INTRODUCTION

Although the saturable Bragg reflectors (SBR) described in the prior chapters are a viable and demonstrated technology for enabling the generation of broad spectra and ultrashort pulses, they and the laser systems they enable are still at times prohibitively expensive and not readily accessible to all researchers. In this chapter, we discuss an alternative approach via supercontinuum generation.

In contrast to SBRs, which aid in generating broad spectra directly from modelocked lasers, supercontinuum generation relies on relatively narrowband, high peak power seed pulses being broadened extra-cavity in highly nonlinear fiber. If desired or necessary, a subsequent compression, or dispersion compensation, stage can be added after supercontinuum generation to re-form the broad spectra and produce ultrashort pulses in time.

Just with the broad spectra alone, there are a variety of useful applications in medical imaging [1], frequency metrology [2, 3, 4], ultrafast spectroscopy [5], device characterization [6, 7], and telecommunications [8, 9]. For example, in telecommunications, the supercontinuum generated in optical fiber is a convenient source

because it provides a very broad bandwidth that can be sliced, as required, into short pulses for individual WDM channels. The pulse trains in each channel have the repetition rate of the source laser, and, when properly adjusted, are chirp-free and have transform-limited pulse widths. These features make the continuum source an attractive alternative to numerous discrete laser diodes, particularly for high-bit-rate communications. These numerous applications have sparked advances in the development of novel fiber systems, such as photonic crystal fibers [10, 11], microstructure fibers [12], and other highly nonlinear solid-core fibers [13, 14, 15, 16].

Producing broad spectra directly from a modelocked ultrafast laser or with additional extra-cavity techniques, such as subsequent compression stages, is complex and expensive. To illustrate and to highlight the impetus for the work in this chapter, consider two examples. First, in our earlier work, ultrashort 20-fs pulses at 1.5 μm, corresponding to a spectral bandwidth of 190 nm, were generated directly from a Cr^{4+}:YAG laser [17]. This experiment used custom-designed double-chirped mirrors for dispersion compensation, as well as a scarce gain crystal that could not be consistently grown at high quality. Modelocking of the laser was not turn-key and required custom-made SBRs to start and enable pulsing [18]. In the second example, 20-fs pulses, also at 1.5-μm, were demonstrated when a semiconductor laser, producing 1-ps pulses, was followed by four successive stages of soliton compression. This system was not only complex and expensive, it also had a large footprint [19]. While these systems were able to produce extremely short pulses along with broad spectra, they also required costly, bulky, and, in the case of the Cr:YAG laser, unique, state-of-the-art components. An alternative that is less complex and more accessible is supercontinuum generation in highly nonlinear fiber.

Large investments in the research of new nonlinear fibers have been made as a result of the advantages outlined above. As mentioned before, photonic crystal fibers, microstructure fibers, and other novel highly nonlinear solid-core fibers, such as chalcogenide glass and bismuth-oxide glass fibers, have been developed and explored extensively. The high nonlinearity of these fibers are a result of small core sizes enabled by high index contrasts, as well as from novel material compositions. In contrast to standard single-mode fibers, where the total dispersion is dominated by the material component, these new fibers have significant waveguide dispersion effects that result in unique total dispersion profiles.

In this chapter, we present the results of supercontinuum generation and pulse compression in a novel solid-core, normally dispersive, highly nonlinear bismuth-oxide fiber [14, 15, 16, 20, 21]. Short lengths of this fiber were used to generate broadband spectra at

telecommunications wavelengths. Using only a 2-cm length of the fiber, we were able to produce spectra from 1200 nm to 1800 nm with a FWHM of 170 nm. Subsequent compression with a simple grating pair yielded 25-fs pulses. For applications requiring only broad spectra, smooth, unstructured, Gaussian-shaped supercontinuum spanning 1200 nm to 1800 nm was generated with a 1-m length of this fiber.

The work presented in this chapter was a collaborative effort. The novel bismuth-oxide fiber was developed and provided to us by the Asahi Glass Company in Japan. The experiments at MIT were performed together with Juliet Gopinath.

4.2 Background and Theory

There are primarily two approaches for supercontinuum generation in optical fiber – with anomalous dispersion fiber or with normal dispersion fiber.

As a quick review, in the anomalous dispersion regime, where group velocity dispersion (GVD) is negative, shorter wavelengths, or blue components, travel faster than longer wavelengths, or red components. While in the normal dispersion regime, where GVD is positive, red spectral components travel faster than blue components. The effect of dispersion is such that a transform-limited input pulse will become temporally dispersed during propagation. Thus, upon passing through an anomalous dispersion material, for example, blue components will arrive in the leading edge of the pulse and red components in the trailing edge.

As a pulse propagates through fiber, the other effect at play is self-phase modulation (SPM), which originates from the Kerr nonlinearity. SPM is the source of the spectral broadening in fiber. As a pulse travels through a Kerr medium, SPM generates new frequency components, which are red-shifted near the leading edge of the pulse and blue-shifted near the trailing edge. The higher the nonlinearity of the fiber, the greater the SPM and the spectral broadening it induces.

When dispersion is coupled with SPM in the anomalous dispersion regime, the interplay between the two effects causes compression of the input pulse. Frequency components in the leading edge of the pulse, which are blue compared to those in the trailing edge as a result of the negative dispersion, are red-shifted by SPM, and the red frequency components of the trailing edge are blue-shifted. The leading edge slows down and the

trailing edge speeds up, resulting in the pulse compressing. The soliton-like interactions under such conditions can lead to both short pulses and broad spectra. In fact, the broadest spectra are observed using anomalous dispersion fiber for supercontinuum generation. However, pulse break-up, modulation instability, and a variety of subsequent nonlinear effects that occur in this regime often produce structured and noisy spectra [22].

On the other hand, in normally dispersive fiber, the pulse lengthens as it propagates, while at the same time, still accumulating additional frequency components from SPM. Under these conditions, with a longer pulse, modulation instability and other nonlinear effects associated with soliton interactions are avoided. Thus, broadening in normally dispersive fiber results in less spectral structure and noise [22, 23]. In addition, because normal dispersion acts to linearize the frequency chirp produced by SPM, the accumulated chirp of a pulse propagating through normal dispersion fiber can be more easily compensated at the output. Consequently, supercontinuum generation in normally dispersive fiber is also more appropriate for pulse compression.

Pulse propagation in single-mode fiber is described by and can be modeled with the nonlinear Schrodinger equation. From this formalism, it can be shown that the spectral broadening in normal dispersion fiber is proportional to $\sqrt{L_d/L_{nl}}$ [24, 25]. Here, the variables L_d and L_{nl}, defined as the dispersion length and the nonlinear length, respectively, provide the length scales over which dispersive or nonlinear effects become important for pulse evolution. Their definitions are:

$$L_d = \frac{\tau_0^2}{\beta_{ave}} \qquad L_{nl} = \frac{1}{\gamma P_0} \tag{4.1}$$

, where τ_0 is the input pulse width, β_{ave} is the average group velocity dispersion of the fiber, γ is the nonlinear parameter of the fiber, and P_0 is the peak power of the input pulse. Using these definitions, we can expand the spectral broadening factor to get

$$\text{Spectral Broadening} \propto \sqrt{L_d/L_{nl}} = \sqrt{\frac{\tau_0^2 \gamma P}{\beta_{ave}}} \tag{4.2}$$

For reference, the nonlinear fiber parameter γ is defined as:

$$\gamma = \frac{2\pi n_2}{\lambda A_{eff}} \tag{4.3}$$

, where n_2 is the material nonlinear refractive index, λ is the wavelength, and A_{eff} is the effective core area of the fiber.

So, the amount of spectral broadening is determined by two exclusive sets of variables – fiber parameters, β_{ave} and γ, and the parameters of your input light, τ_0 and P_0. We can maximize the spectral broadening by using fiber with very high nonlinearity and/or by using input pulses with high peak power. Dispersion ultimately limits the amount of spectral broadening that is possible, but the supercontinuum that is generated is still smooth and controlled.

4.3 BISMUTH-OXIDE FIBER

The bismuth-oxide fiber we used in our experiment has a conventional step-index solid-core structure with a nonlinearity of 1100 ± 15% $(\text{W-km})^{-1}$, approximately 400 times greater than that of standard dispersion-shifted single-mode fiber and on par with that of photonic crystal fibers and microstructure fibers. Here, however, the nonlinearity was achieved with a solid core form. Figure 4.1 below shows a cross section of the bismuth-oxide fiber.

This very high nonlinearity is a result of the high material nonlinear refractive index coefficient of the bismuth-oxide glass – 1.1×10^{-18} m^2/W – and the small effective area of the fiber. The fiber has a core diameter of 1.7 μm and an effective area of 3.3 μm^2. This small core size was made possible by the relatively high index contract of the core and cladding materials. The refractive indices of the core and cladding were 2.22 and 2.13, respectively. Without a high index contrast, the propagating light mode would otherwise leak out of the very small core and into cladding.

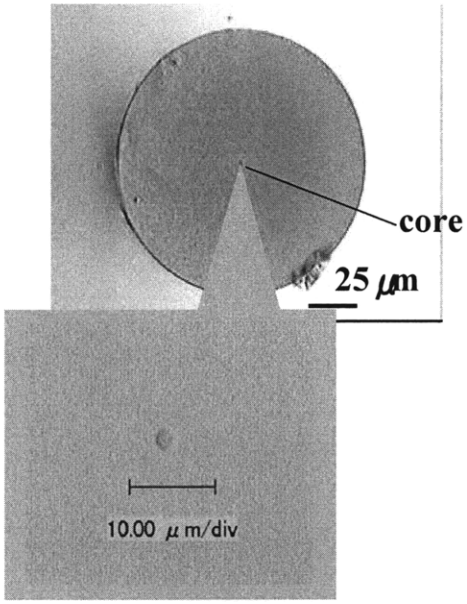

Figure 4.1 Cross-section of the highly nonlinear bismuth-oxide glass fiber [21]. Courtesy of Asahi Glass Company.

By doping the core with In_2O_3, the refractive index of the bismuth-oxide glass can be increased. Another beneficial effect of adding In_2O_3 is that it also increases the difference between the glass transition temperature T_g and the crystallization temperature T_x, This parameter, $(T_x - T_g)$, is characteristic of the thermal stability of the glass, and is an important factor in the production of these fibers, with higher values being more favorable for drawing fiber. The refractive index of the bismuth-oxide core can be approximated using a Sellmeier equation of the following form:

$$n = \sqrt{a + \frac{b\lambda^2}{\lambda^2 - c} + d\lambda^2} \tag{4.4}$$

, with a = 1.0, b = 3.93225, c = 0.04652, and d = -0.00796 for our fiber samples. The refractive index as a function of wavelength is shown in Figure 4.2.

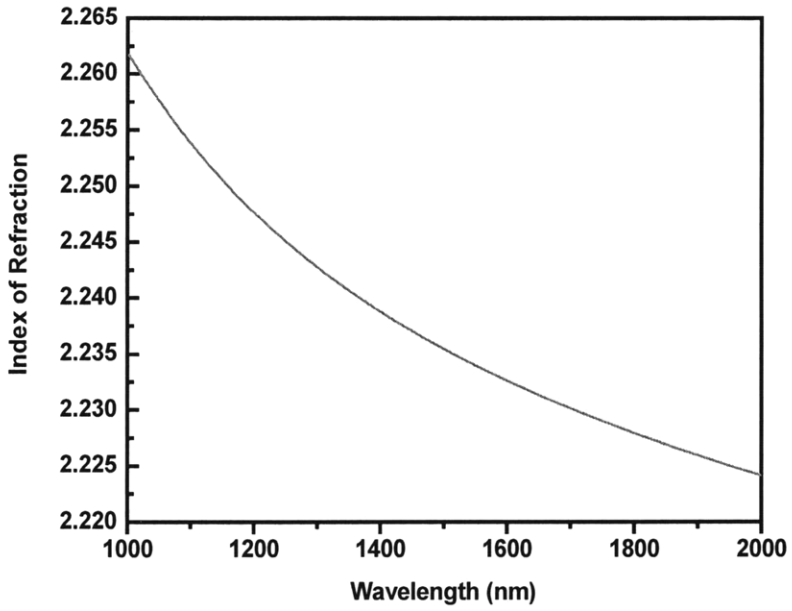

Figure 4.2 Refractive index of the bismuth-oxide glass as a function of wavelength.

As mentioned before, the waveguide dispersion plays a more prominent role in this bismuth-oxide fiber, due to the small core size and high index contrast. The total dispersion of the bismuth-oxide fiber as a function of wavelength is plotted in Figure 4.3, together with the material and waveguide components that it is comprised of. The waveguide dispersion was calculated for the lowest order HE mode in a step-index fiber. The mode propagation constant was solved on an iterative basis, and the mode index and dispersion of the fiber were calculated in turn [26].

We see that the slope of the waveguide dispersion component offsets that of the material dispersion, resulting in a relatively flat total dispersion profile over the large wavelength range of 1200 nm to 1800 nm. The calculated result matched well to the measured dispersion value of –250 ps/nm/km of the bismuth-oxide fiber sample at 1550 nm [15].

A simulation of the supercontinuum generation in the bismuth-oxide fiber was done, assuming a fiber length of 2 cm, and 150-fs input pulse widths centered at 1540 nm with 2.6 kW peak powers. These parameters correspond to the input pulses used in our experiments, and, together with the fiber parameters, yield dispersion length L_d and nonlinear length L_{nl} values of 2.58×10^{-2} m and 3.9×10^{-4} m, respectively. The resulting output spectrum is shown in Figure 4.4 below.

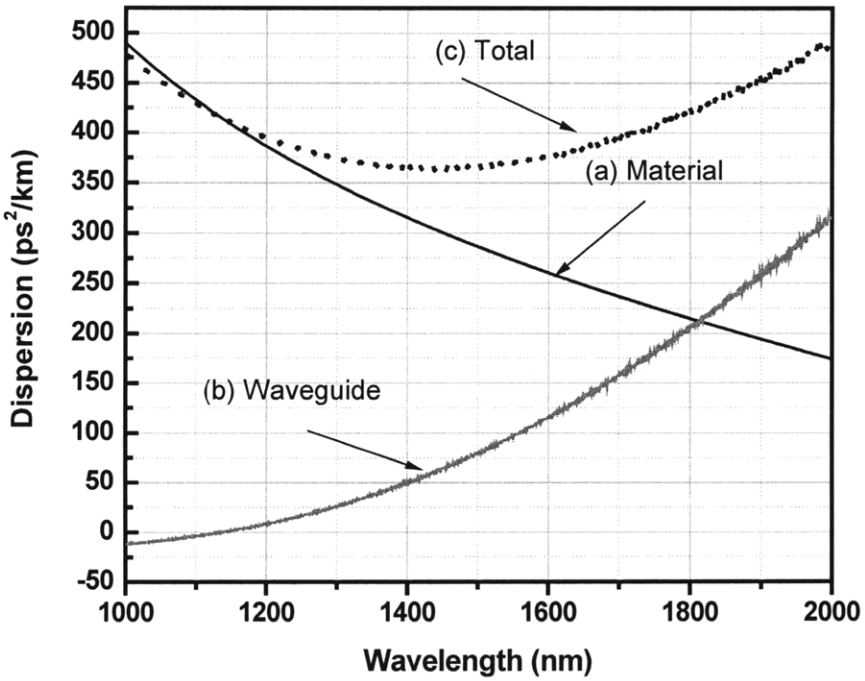

Figure 4.3 Calculated total dispersion profile of the highly nonlinear bismuth-oxide glass fiber as a function of wavelength, along with its component parts – the material dispersion and the waveguide dispersion.

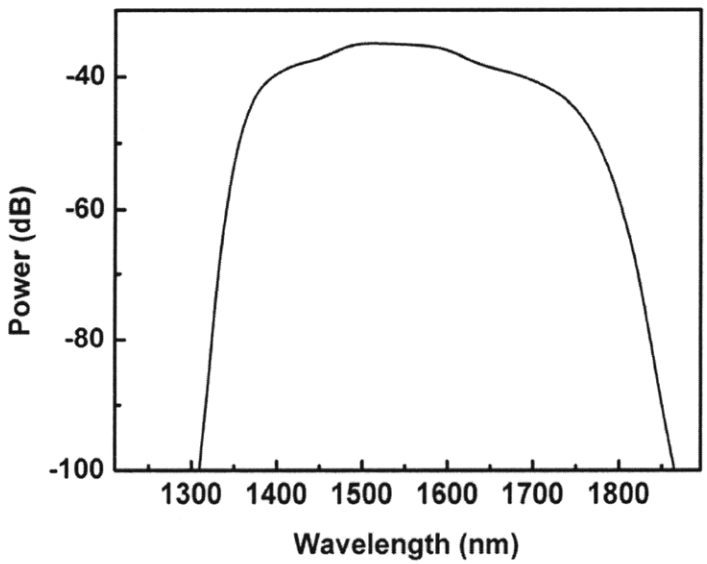

Figure 4.4 Simulation result of supercontinuum generation in a 2-cm length of highly nonlinear bismuth-oxide glass fiber, with 150-fs input pulses at 1540 nm and 2.6 kW peak powers.

Because the nonlinear length is so short, 2 cm is sufficient length for the spectral broadening to occur. The resulting 3-dB spectral width of the output is 200 nm. The spectral shape is smooth and flat, and is suitable for pulse compression.

4.4 EXPERIMENTAL SETUP

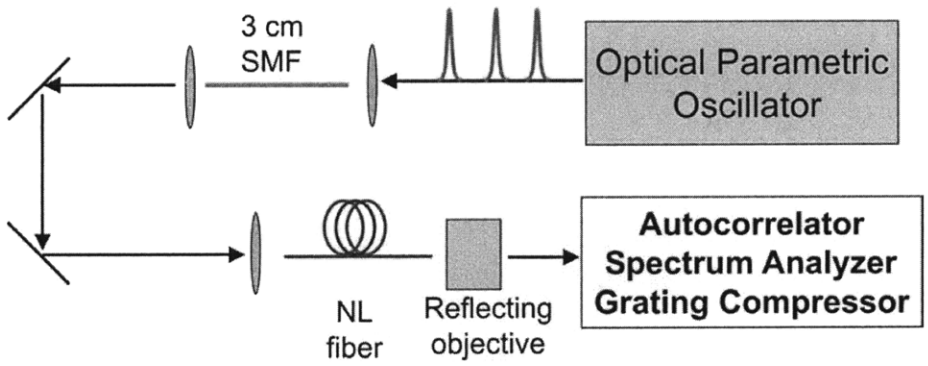

Figure 4.5 Experimental setup for supercontinuum generation in the bismuth-oxide glass fiber.

The experimental setup for supercontinuum generation is shown above in Figure 4.5. A Spectra-Physics optical parametric oscillator (OPO), synchronously pumped at 82 MHz by a Ti:sapphire laser, supplies the input seed pulses, which have 150-fs pulse widths and are tunable from 1400 nm to 1600 nm. Note that similar pulse characteristics are also available from more compact modelocked fiber lasers. The OPO pulses pass through an isolator, and are then spatially filtered with a 3-cm length of single-mode fiber. Because of its short length, the pulses were not significantly chirped and distorted. An aspheric lens, with an NA of 0.5, is then used to couple the light into a length of the highly nonlinear bismuth-oxide glass fiber. The output is collimated with a reflecting objective and subsequently directed to an optical spectrum analyzer, autocorrelator, or grating compressor, for characterization or pulse compression. The reflecting objective had approximately 30% loss, but its use eliminated additional material dispersion effects that would otherwise accompany another lens after the nonlinear fiber.

Two lengths of the highly nonlinear bismuth-oxide glass fiber, 2 cm and 1 m, were extensively investigated in our experiments. The 1-m length of fiber was prepared using a standard fiber cleaver at low tension (80 g). With the 2-cm length, however, clean and even cuts of the end facets could not be achieved with a standard cleaver due to the short length. As a result, the fiber had to be manually prepared and polished.

First, the fiber was stripped of its protective coating, and then placed into two connected 1-cm ceramic ferrules and embedded in a thin layer of wax for stability. A photo of this mount is shown in Figure 4.6.

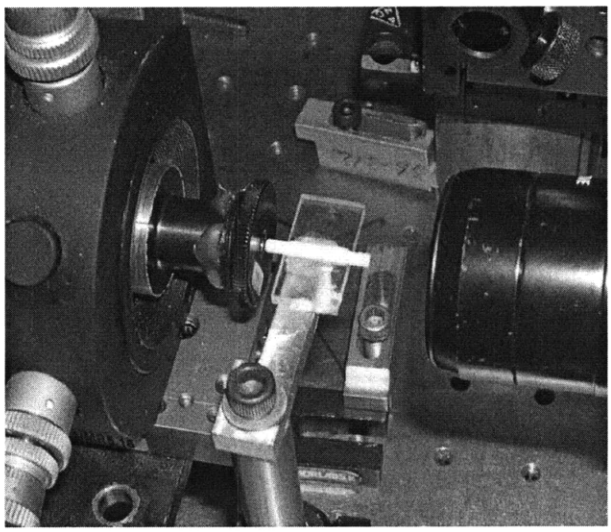

Figure 4.6 A manually polished 2-cm length of the highly nonlinear bismuth-oxide fiber in its custom ceramic ferrule mount.

The ends of the fiber were then cut and manually polished with an Ultra Tec polishing machine. Polishing was a multi-step process using gradually finer and finer grades of silicon carbide and diamond polishing films. Excessively aggressive films and polishing times destroyed or disrupted beyond repair the bismuth-oxide fiber facets. Examples of such defects are shown below in Figure 4.7.

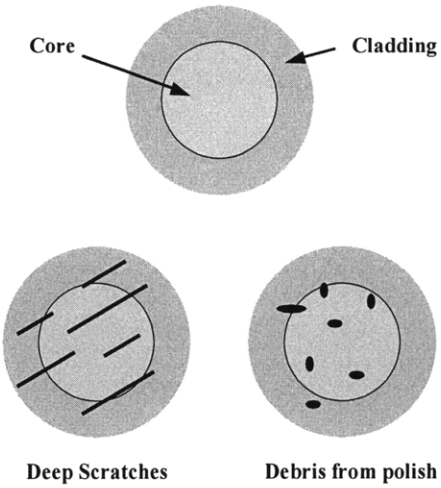

(a)

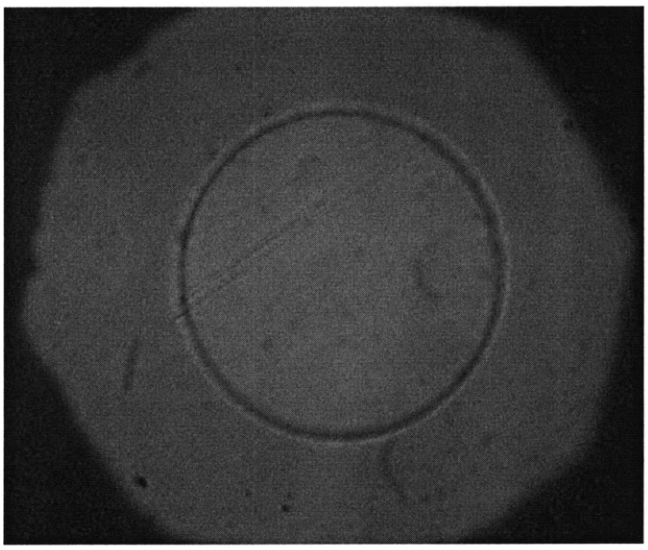

(b)

Figure 4.7 (a) Illustrative examples of defects on the fiber end facets created by polishing. (b) Photo of a mis-polished end facet with line defects as well as debris.

Several polishing "recipes" were experimented with before finally finding one that yielded end facets that were free of defects. The recipe is shown in Figure 4.8. The dimensions indicated refer to the size of the abrasive agent used for polishing the end faces. All steps were performed with a constant polishing speed of 60-100 RPM. Too high a polishing speed, as well as overly long exposure to the polishing agent, could both impart irreparable damage. It is essential to use clean water to prevent foreign particles from destroying the

polish. Tap water and other water sources, contain particles (dirt) that can be as large as 15 μm. Debris of this size will destroy a polished end facet. De-ionized or filtered water eliminates this possibility.

Step	Polishing Agent	Time	Lubrication
1	9 μm silicon carbide polishing film	30 seconds	Filtered water
2	3 μm silicon carbide polishing film	60 seconds	Filtered water
3	1 μm diamond polishing film	90 seconds	Filtered water
4	0.5 μm diamond polishing film	90 seconds	Filtered water
5	ULTRAFILM B	60 seconds	ULTRAPOL B polishing suspension

Figure 4.8 Polishing recipe for the 2-cm length of highly nonlinear bismuth-oxide fiber.

4.5 Experimental Results

4.5.1 Supercontinuum Generation

Spectra from the 2-cm length of fiber are shown in Figure 4.9. The OPO input was centered at 1540 nm, and the coupling loss was 6 dB. Supercontinuum is produced from 1200 nm to > 1700 nm, with an average output power of 32 mW and a 3 dB width of 170 nm. The optical spectrum analyzer had a wavelength range limited to <1700 nm. For an average power of 32 mW exiting the nonlinear fiber, the measured pulse width was 865 fs. For an output power of 21.4 mW, the pulse width was 759 fs. For an output power of 14 mW, the pulse width was 724 fs. For an output power of 7 mW, a 488 fs pulse width was measured. The spectral widths and shapes match well with simulation results. As expected, the greater the input power, the broader the spectral widths.

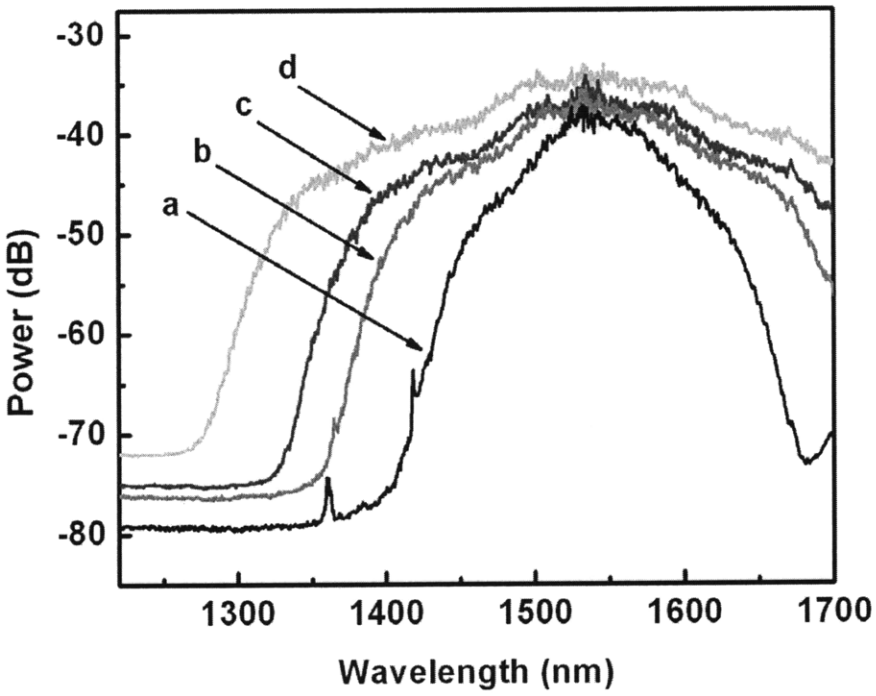

Figure 4.9 Variation with input pulse power of supercontinuum spectra generated in a 2-cm length of highly nonlinear bismuth-oxide glass fiber for an incident wavelength of 1540 nm. Average powers exiting the nonlinear fiber were (a) 7 mW, (b) 14 mW, (c) 21 mW, and (d) 32 mW.

Insufficient attenuation of cladding modes causes the interference seen in the center of the spectra. Optical wave breaking is responsible for the shoulders apparent in the spectra [25]. In the normal dispersion regime, this happens when the effects of self-phase modulation (SPM) are much greater than the effects of group-velocity dispersion (GVD). Both GVD and SPM impose a frequency chirp on the pulse as it travels down the fiber. The frequency chirp resulting from GVD, however, is linear in time, whereas that from SPM is not. Because of the nonlinear nature of the composite chirp, different parts of the pulse propagate at different speeds. Red-shifted light near the leading edge of the pulse overtake un-shifted light there. The opposite occurs for blue-shifted light near the trailing edge. In both cases, the leading and trailing regions of the pulse contain light at different frequencies that interfere. It is this interference that is the origin of the oscillations near the pulse edges and the shoulders seen in the spectra.

Figure 4.10 shows typical supercontinuum spectra obtained for input wavelengths of 1450 nm, 1500 nm, and 1540 nm, with the 2-cm length of bismuth-oxide fiber. Note that the

spectra have been vertically offset for ease of viewing. The power was kept constant for all three measurements. As expected, spectra generated at the three different wavelengths look very similar. This result was indicative of the relatively flat dispersion profile of the fiber shown in Figure 4.3. A more complete investigation of the long-wavelength end of the spectrum was attained by using a tunable spectrometer, in addition to the optical spectrum analyzer. Peter Rakich kindly provided and assisted us with the spectrometer. In the case of the 1540 nm incident wavelength, the supercontinuum generated extends to about 1800 nm.

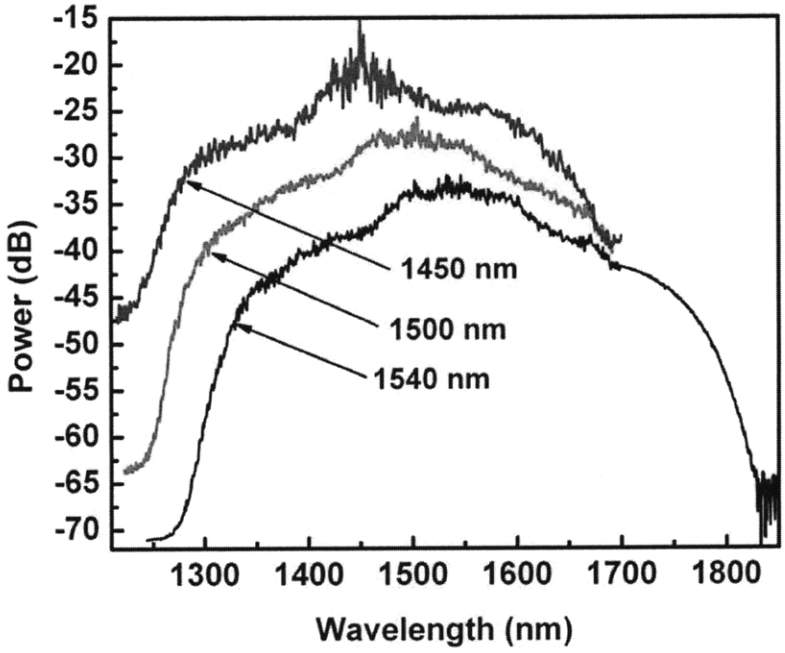

Figure 4.10 Variation with input wavelength of supercontinuum spectra generated in a 2-cm length of highly nonlinear bismuth-oxide glass fiber. The spectra were generated with comparable input powers and have been vertically offset for ease of viewing. Measurements up to 1700 nm were taken with an optical spectrum analyzer, and measurements beyond 1700 nm were taken with a spectrometer.

Now, if ultrashort pulses are the goal, then we need to augment the experimental setup with an additional pulse compression stage, which will be the subject of the next section.

For those applications that require only broad spectra, a longer length of the highly nonlinear bismuth-oxide fiber may be used. In this case, an aspheric lens was used to collimate the output from the nonlinear fiber. Figure 4.11 shows spectra produced from a 1-m length of the bismuth-oxide fiber as a function of input power. The wavelength of the

incident light for these spectra was 1540 nm. The maximum average output power was 34 mW, and the corresponding pulse energy was 0.41 nJ. At this power, we estimate the output pulse width to be 80 ps, using an analytical expression for chirped pulse propagation derived from the nonlinear Schrodinger equation. The spectrum that was generated with the 1-m length of nonlinear fiber was very similar to that produced in the 2-cm length. However, the key here is that the cladding modes have been effectively suppressed with the longer 1-m length. After propagating through the first 2 cm of the bismuth-oxide fiber, the pulse broadens to 800 fs and the effects of SPM are greatly reduced. The result is a smoother, more Gaussian-shaped output spectrum.

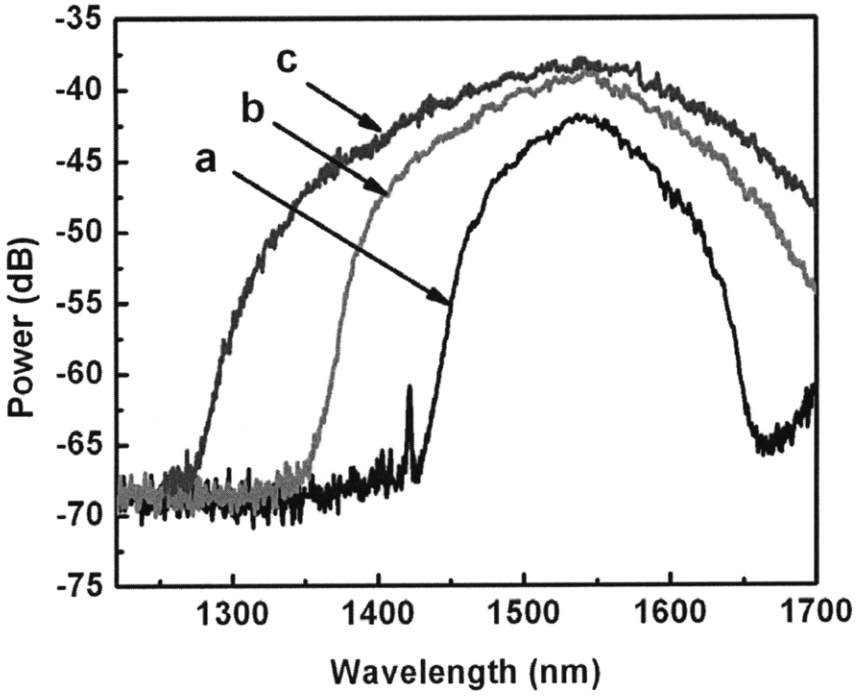

Figure 4.11 Variation with input pulse power of supercontinuum spectra generated in a 1-m length of highly nonlinear bismuth-oxide glass fiber for an incident wavelength of 1540 nm. Average incident powers and pulse energies were (a) 10 mW (0.12 nJ), (b) 20 mW (0.24 nJ), and (c) 34 mW (0.41 nJ). Smoother, Gaussian-shaped spectra are produced in the longer length of fiber.

4.5.2 FEMTOSECOND PULSE COMPRESSION

In order to produce short pulses from the broad spectra we've generated, the pulses need to be re-formed and compressed through the introduction of negative, or anomalous, dispersion to compensate the positive dispersion accumulated while traveling through the bismuth-oxide fiber. As a reminder, in the anomalous dispersion regime, blue spectral components travel faster, hence arrive earlier, than red spectral components.

Two commonly used techniques – grating pairs and Brewster-cut prism pairs – can be used to introduce this compensating negative dispersion for pulse compression. A third alternative exists with the use of chirped mirrors, however, the total dispersive delay produced by chirped mirrors is very limited. Chirped fiber Bragg gratings are yet another compact and elegant possibility.

We give a quick review of the grating pair and prism pair techniques below for reference.

PULSE COMPRESSION WITH A GRATING PAIR

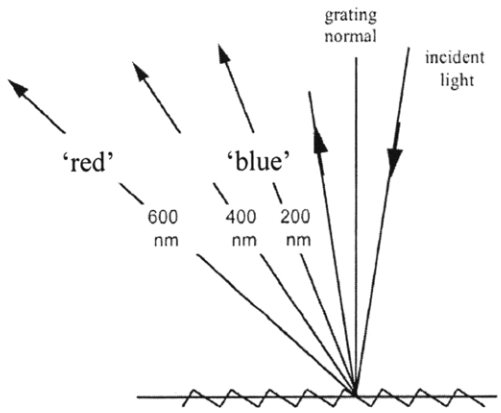

Figure 4.12 Diffraction by a reflection grating.

Gratings work similarly to mirrors. The maxima and minima of the reflected light depend on constructive and destructive interference. A longer wavelength means a greater vertex angle from the incident beam to the reflected and diffracted beam, in order to provide the length needed to constructively interfere. Hence, for gratings, the longer the wavelength, the greater the diffraction. This is expressed by the grating equation

$$m\lambda = d\left(\sin\alpha + \sin\beta\right) \tag{4.5}$$

, where m is the diffraction order, which is an integer; d is the groove spacing of the grating; α is the angle of incidence; and β is the diffracted angle.

It is intuitive to see why a grating pair introduces negative group delay dispersion. In the configuration of a pair of gratings as in Figure 4.13 below, the longer wavelengths (reds) are forced to travel a longer distance than the shorter wavelengths (blues), since they are diffracted at a larger angle. Hence, blue components arrive before the red components, and we get negative dispersion.

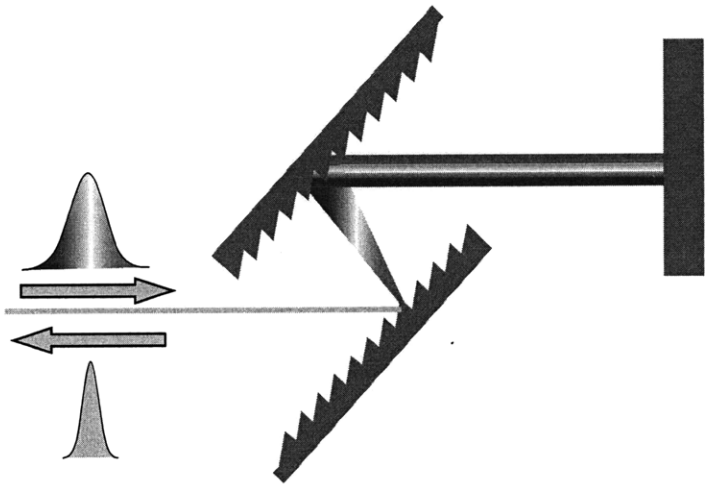

Figure 4.13 Configuration of a grating pair used for pulse compression.

The expression for the group delay dispersion (GDD) introduced by a grating pair is:

$$\mathrm{GDD}_{\textit{grating pair}} = -\frac{\lambda^3}{(2\pi c)^2}\frac{2\pi L}{d^2} \times \frac{1}{\left[1-\left(\sin\alpha - \frac{\lambda}{d}\right)^2\right]^{3/2}} \tag{4.6}$$

where L is the perpendicular distance between the gratings [27, 28].

Pulse Compression with a Prism Pair

While gratings work by diffraction, prisms introduce dispersion through refraction. Recall from any introductory physics textbook the classic graphic of a prism dispersing white light – blue is bent the most and red the least in the rainbow that emerges (Figure 4.14). For prisms, the longer the wavelength, the smaller the refraction, that is, the lesser the angular deviation – a behavior opposite from that of gratings.

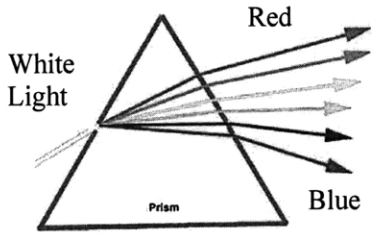

Figure 4.14 Prisms bend shorter wavelengths (blue) more than longer wavelengths (red).

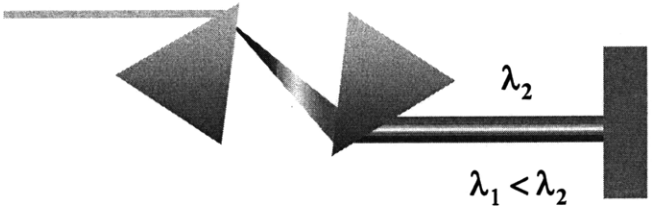

(a)

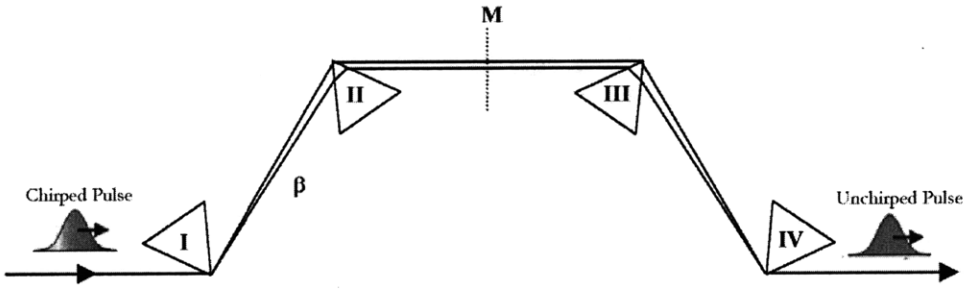

(b)

Figure 4.15 (a) Configuration of a Brewster-cut prism pair used for pulse compression. (b) The effective expansion of the configuration in (a), where M represents the mirror.

Similar to a grating pair, the group delay from a prism pair is geometrical and angular in nature [29, 30]. However, the manner in which a prism pair is able to produce negative dispersion is not as clear and not as intuitive, because now, the angular dispersion is 'flipped' from that of the gratings, and optical path lengths are involved. The math however confirms this, and, in the end, after traversing a prism pair, red spectral components do travel a greater optical length (presumably through the glass material) than blue components. The geometric contribution of the prism pair provides negative group delay. The expression for this group delay dispersion is:

$$\mathrm{GDD}_{geometric} = -2\frac{\lambda^3}{\pi c^2}\left(\frac{dn}{d\lambda}\right)^2 \times l \tag{4.7}$$

where l is the apex-to-apex prism separation distance [30].

Insertion of the second prism in the configuration shown in Figure 4.15(a) adds an adjustable amount of positive material dispersion. The expression for this component of the GDD is the standard material dispersion GDD:

$$\mathrm{GDD}_{material} = \frac{\lambda^3}{2\pi c^2}\frac{d^2n}{d\lambda^2} \times L \tag{4.8}$$

where L is the insertion path length in the second prism.

Together, the geometrical and material dispersion determine the overall dispersion of the prism pair. This way, the dispersion of a prism pair is tunable. Altogether, the group delay dispersion introduced by a prism pair is:

$$\mathrm{GDD}_{prism\ pair} = -2\frac{\lambda^3}{\pi c^2}\left(\frac{dn}{d\lambda}\right)^2 \times l + \frac{\lambda^3}{2\pi c^2}\frac{d^2n}{d\lambda^2} \times L \tag{4.9}$$

Note that the prisms are Brewster cut to minimize loss. The expressions above take this into account.

Both techniques have their inherent advantages and disadvantages. Diffraction gratings have greater resolving power, however, relative to prisms, they introduce more loss.

Prisms can handle higher intensities, have lower loss, and can provide adjustable dispersion compensation, from negative through positive values.

Experimental Setup and Results

We investigated both prism pairs and grating pairs for compressing the broad spectra we generated from the 2-cm piece of the nonlinear bismuth-oxide fiber. Pulse compression experiments were performed for the spectra generated with the 1540-nm incident wavelength.

We first attempted pulse compression with silicon prisms, which we believed were ideal for our spectra given their low material loss and high dispersion. For the silicon prisms in our setup, the group-velocity dispersion was –1781 fs^2/cm of prism separation. We tried to avoid the positive material dispersion component, and the third-order dispersion, as much as possible by minimizing the insertion of the second prism. Third-order dispersion was -1350 fs^3/cm of insertion path length. However, complete dispersion compensation, and hence pulse compression, could not be achieved, due to geometric limitations of the setup and the residual third-order dispersion originating from the material dispersion component of the prism pair. CaF_2 and BaF_2 prism pairs were also investigated. The CaF_2 prisms were unable to provide sufficient dispersion, and the BaF_2 prisms had deteriorated with water content and did not work for us.

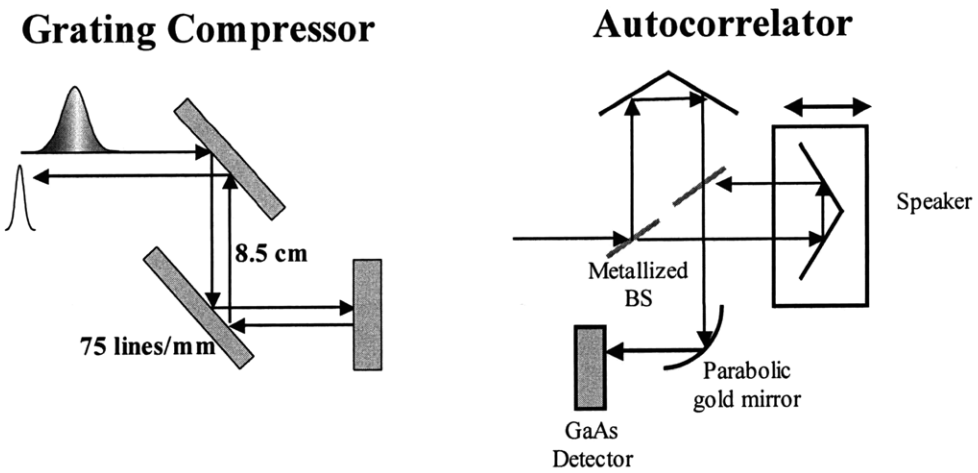

Figure 4.16 Grating compressor and low-dispersion broadband autocorrelator setups used to compress and measure the spectrally broadened pulses from the nonlinear bismuth-oxide fiber.

A grating pair, providing –6400 fs^2 of dispersion, was ultimately used to compress our pulses. Two gold 75-lines/mm gratings, separated by 8.5 cm, were used in an experimental setup like that shown in Figure 4.16 above. The compressor had 5 dB of loss, with 6 mW of average power exiting the grating pair. The broadband interferometric autocorrelator used to measure the compressed pulses consisted of two metallic inconel beamsplitters, a speaker to dither the delay, and an off-axis parabolic mirror to focus light onto a GaAs LED, which was used as a two-photon-absorption detector. An autocorrelation trace of the compressed pulse from the nonlinear bismuth-oxide fiber and grating pair is shown in Figure 4.17 below, along with the corresponding spectrum.

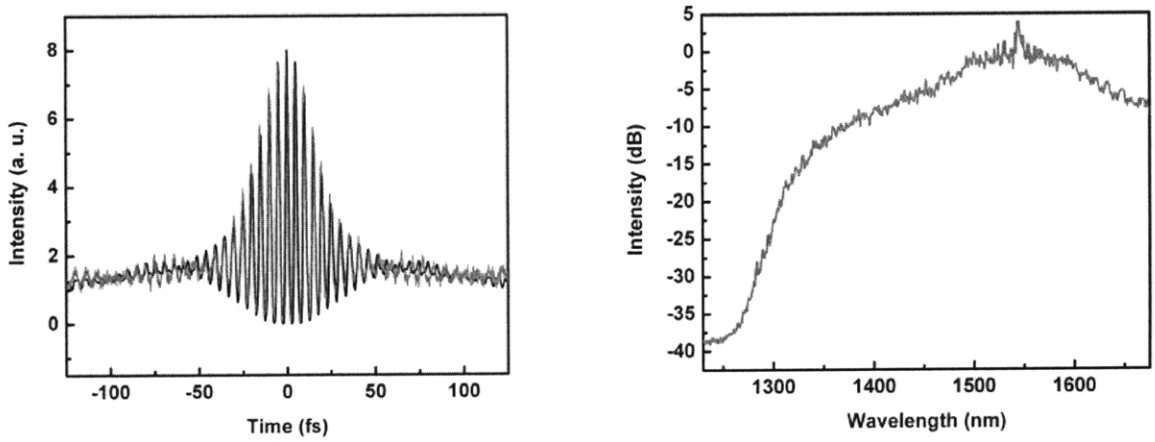

Figure 4.17 Measured interferometric autocorrelation and spectrum of compressed pulses from a 2-cm length of highly nonlinear bismuth oxide fiber. A pulse width of 25 fs was extracted from the PICASO phase retrieval algorithm fit of the measured data.

Using the PICASO phase retrieval algorithm to fit the measured autocorrelation and spectrum, the resulting compressed pulse width was calculated to be 25 fs, more than 5-fold reduced from the starting pulse width of 150 fs from the OPO [31]. Assuming a sech pulse envelope shape, the time-bandwidth product of our compressed pulses was 0.49. The transform limit of the measured spectrum was 16 fs. Higher-order chirp, as well as the roll-off in spectral efficiency of the gratings for wavelengths shorter than 1500 nm, likely limited the compressed pulse width.

4.6 CONCLUSION

Very short lengths of highly nonlinear bismuth-oxide fiber have been used to generate smooth broadband spectra at telecommunications wavelengths. Using only a 2-cm length of this fiber, we were able to produce broadband spectra spanning 1200 nm to 1800 nm, corresponding to a spectral broadening factor of 10. For applications that require only a broad spectrum, we demonstrated smooth, Gaussian-shaped spectra of the same bandwidth with a 1-m length of the fiber. With the 2-cm piece of bismuth-oxide fiber, and a grating pair, compression of 150-fs seed pulses down to 25 fs was achieved. These results show that highly nonlinear, step-index bismuth-oxide fiber is a promising tool for applications requiring broad spectra and/or short pulses in the 1.5 μm wavelength region.

REFERENCES

1. W. Drexler, U. Morgner, F. X. Kaertner, C. Pitris, S. A. Boppart, X. D. Li, E. P. Ippen, and J. G. Fujimoto, "In vivo ultrahigh-resolution optical coherence tomography," Optics Letters **24**, 1221 (1999).

2. D. J. Jones, S. A. Diddams, J. K. Ranka, A. Stentz, R. S. Windeler, J. L. Hall, and S. T. Cundiff, "Carrier-envelope phase control of femtosecond mode-locked lasers and direct optical frequency synthesis," Science **288**, 635 (2000).

3. S. A. Diddams, D. J. Jones, J. Ye, S. T. Cundiff, J. L. Hall, J. K. Ranka, R. S. Windeler, R. Holzwarth, T. Udem, and T. W. Hansch, "Direct link between microwave and optical frequencies with a 300 THz femtosecond laser comb," Physical Review Letters **84**, 5102 (2000).

4. B. R. Washburn, S. A. Diddams, N. R. Newbury, J. W. Nicholson, M. F. Yan, and C. G. Jorgenson, "Phase-locked, erbium-fiber-laser-based frequency comb in the near infrared," Optics Letters **29**, 250 (2004).

5. J. Shah, "Ultrafast spectroscopy of semiconductors and semiconductor nanostructures," Springer Series in Solid-State Sciences **115**, (Springer, New York, New York, 1999).

6. P. T. Rakich, J. T. Gopinath, H. Sotobayashi, C. W. Wong, S. G. Johnson, J. D. Joannopoulos, and E. P. Ippen, "Broadband supercontinuum-based measurements of high-index contrast photonic bandgap devices from 1 to 2 μm," **Th13**, presented at the LEOS Annual Meeting (2004).

7. R. T. Neal, M. D. C. Charlton, G. J. Parker, C. E. Finlayson, M. C. Netti, and J. J. Baumberg, "Ultrabroadband transmission measurements on waveguides of silicon-rich silicon dioxide," Applied Physics Letters **83**, 4598 (2003).

8. L. Boivin, M. C. Nuss, W. H. Knox, and J. B. Stark, "206-channel chirped-pulse wavelength-division multiplexed transmitter," Electronics Letters **33**, 827 (1997).

9. B. Mikulla, L. Leng, S. Sears, B. C. Collings, M. Arend, and K. Bergman, "Broad-band high-repetition-rate source for spectrally sliced WDM," IEEE Photonics Technology Letters **11**, 418 (1999).

10. J. C. Knight, J. Arriaga, T. A. Birks, A. Blanch-Ortigosa, W. J. Wadsworth, and P. St. J. Russell, "Anomalous dispersion in photonic crystal fiber," IEEE Photonics Technology Letters **12**, 807 (2000).

11. H. Ebendorff-Heidepriem, P. Petropoulos, S. Asimakis, V. Finazzi, R. C. Moore, K. Frampton, F. Koizumi, D. J. Richardson, and T. M. Monro, "Bismuth glass fibers with high nonlinearity," Optics Express **12**, 5082 (2004).

12. J. K. Ranka, R. S. Windeler, and A. J. Stentz, "Optical properties of high-delta air-silica microstructure optical fibers," Optics Letters **25**, 796 (2000).

13. R. E. Slusher, G. Lenz, J. Hodelin, J. Sanghera, L. B. Shaw and I. D. Aggarwal, "Large Raman gain and nonlinear phase shifts in high-purity As_2Se_3 chalcogenide fibers, " Journal of the Optical Society of America B **21**, 1146 (2004).

14. K. Kikuchi, K. Taira, and N. Sugimoto, "Highly nonlinear bismuth oxide-based glass fibres for all-optical signal processing," Electronics Letters **38**, 156 (2002).

15. N. Sugimoto, T. Nagashima, T. Hasegawa, S. Ohara, K. Taira, and K. Kikuchi, "Bismuth-based optical fiber with nonlinear coefficient of 1360 $W^{-1}km^{-1}$," **PDP26**, presented at Optical Fiber Communication Conference (2004).

16. J. T. Gopinath, H. M. Shen, H. Sotobayashi, and E. P. Ippen, "Smooth supercontinuum generation with highly nonlinear bismuth-oxide fiber," **WD2**, presented at LEOS Annual Meeting (2004).

17. D. J. Ripin, C. Chudoba, J. T. Gopinath, J. G. Fujimoto, E. P. Ippen, U. Morgner, F. X. Kartner, V. Scheuer, G. Angelow, and T. Tschudi, "Generation of 20-fs pulses by a prismless Cr^{4+}:YAG laser," Optics Letters 27, 61 (2002).

18. D. J. Ripin, J. T. Gopinath, H. M. Shen, A. A. Erchak, G. S. Petrich, L. A. Kolodziejski, F. X. Kartner, and E. P. Ippen, "Oxidized GaAs/AlAs mirror with a quantum-well saturable absorber for ultrashort-pulse Cr^{4+}:YAG laser," Optics Communications **214**, 285 (2002).

19. Y. Matsui, M. D. Pelusi, and A. Suzuki, "Generation of 20-fs optical pulses from a gain-switched laser diode by a four-stage soliton compression technique," IEEE Photonics Technology Letter **11**, 1217 (1999).

20. J. T. Gopinath, H. M. Shen, H. Sotobayashi, E. P. Ippen, T. Hasegawa, T. Nagashima, and N. Sugimoto, "Highly nonlinear bismuth-oxide fiber for smooth supercontinuum generation at 1.5 μm," Optics Express **12**, 5697 (2004).

21. J. T. Gopinath, H. M. Shen, H. Sotobayashi, E. P. Ippen, T. Hasegawa, T. Nagashima, and N. Sugimoto, "Highly nonlinear bismuth-oxide fiber for supercontinuum generation and femtosecond pulse compression," Journal of Lightwave Technology **23**, 3591 (2005).

22. K. L. Corwin, N. R. Newbury, J. M. Dudley, S. Coen, S. A. Diddams, B. R. Washburn, K. Weber and R. S. Windeler, "Fundamental amplitude noise limitations to supercontinuum spectra generated in a microstructured fiber," Applied Physics B **B77**, 269 (2003).

23. S. Taccheo and L. Boivin, "Investigation and design rules of supercontinuum sources for WDM applications," Optical Fiber Communication Conference **ThA1**, (2000).

24. W. J. Tomlinson, R. H. Stolen, and C. V. Shank, "Compression of optical pulses chirped by self-phase modulation in fibers," Journal of Optical Society of America B **1**, 139 (1984).

25. G. P. Agrawal, *Nonlinear Fiber Optics*, Academic Press (2001).

26. A. Yariv, *Optical Electronics in Modern Communications*, Oxford University Press (1997)

27. E. B. Treacy, "Optical pulse compression with diffraction gratings," IEEE Journal of Quantum Electronics **QE-5**, 454 (1969).

28. H. M. Shen, MIT 6.631 Optics and Photonics notes.

29. R. L. Fork, O. E. Martinez, and J. P. Gordon, "Negative dispersion using pairs of prisms," Optics Letters **9**, 150 (1984).

30. O. E. Martinez, J. P. Gordon, and R. L. Fork, "Negative group-velocity dispersion using refraction," JOSA A **1**, 1003 (1984).

31. W. Nicholson, J. Jasapara, W. Rudolph, F. G. Omenetto and A. J. Taylor, "Full-field characterization of femtosecond pulses by spectrum and cross-correlation measurements," Optics Letters **24**, 1774 (1999).

Chapter 5

CONCLUSION

The theme of this thesis – broadband light sources at 1.5 μm – was presented through three primary research efforts.

First, oxidized broadband III/V-based semiconductor saturable absorber mirrors were developed for and implemented in a variety of ultrafast solid-state and fiber lasers. The III/V SBR structures were fabricated with an improved AlAs oxidation process that yielded stable large-area mirrors that were implemented in a number of lasers spanning the visible to near-infrared wavelengths. Self-starting femtosecond modelocked operation was achieved in Cr^{4+}:YAG, Cr:forsterite, Ti:sapphire, Er:glass and bismuth-oxide erbium-doped fiber lasers. Compact, reliable and capable of enabling turnkey operation, these devices improve the accessibility of ultrafast lasers for the numerous applications outlined in the Introduction. In addition, a silicon/germanium saturable Bragg reflector fabricated with a CMOS compatible process was also demonstrated. Its nonlinear response was characterized with femtosecond pump-probe measurements, which showed surprisingly fast saturable absorption on a femtosecond scale and strong inverse saturable absorption at large fluence values. The device was used to attain self-starting modelocked operation of a Er:Yb:glass laser with an optical spectrum covering the entire C-band of optical communications.

Second, SBR structures were developed and fabricated for use in short-cavity, high-repetition rate lasers. Structure design was modified to optimize the saturation behavior in such environments through the addition of resonant coating layers to enhance the modulation depth, thereby reducing the saturation fluence, and also by proton bombardment to reduce recovery times. Devices with modulation depths ranging from 1.7% to 11% have been fabricated. Fast and slow recovery times as low as 2 ps and 40 ps, respectively, have also been measured. Preliminary testing of these designs in gigahertz lasers have yielded promising results, and subsequent design iterations should continue improving performance. In addition, novel SBR structures have been designed that integrate dispersion compensation together with saturable absorption. These structures still await fabrication, but their potential performance capability looks promising, especially for generating short pulses together with achieving high repetition rates.

Third, and finally, controlled supercontinuum generation was demonstrated with a novel highly nonlinear bismuth-oxide glass fiber. Fibers with some of the highest nonlinearities reported, 1100 $(W\text{-}km)^{-1}$ have been fabricated and supplied by the Asahi Glass Company for our experiments. Compared to even more nonlinear chalcogenide glasses, bismuth-oxide glass represents a pragmatic compromise that achieves high nonlinearity without the need to handle toxic material. A short 2-cm length of nonlinear bismuth-oxide fiber was used to spectrally broaden a 20-nm FWHM spectra to a 200-nm FWHM. Subsequent pulse compression yielded 25-fs pulse widths, comparable to what was previously achieved in an ultrafast Cr^{4+}:YAG laser.

In summary, a variety of broadband optical sources at 1.5 μm and devices that enable those sources have been studied in this thesis. Saturable Bragg reflectors designed for ultra-broadband operation and ultrashort pulse generation have been demonstrated in a variety of self-starting laser systems producing femtosecond pulses. SBRs have also been designed for high-repetition rate systems, and have undergone initial testing with promising results. Controlled supercontinuum generation and femtosecond pulse compression was demonstrated with highly nonlinear bismuth-oxide fiber.

APPENDIX A

MIRROR DESIGN CODE – ANALYSIS FORMALISM

A summary of the formalism and guiding equations utilized in the mirror design code is provided here. More extensive coverage and elegant explanations can be found in *Electromagnetic Wave Theory* by Kong [1].

The highly reflective broadband mirrors discussed in this these are composed of alternating quarter-wave-thick layers of high and low refractive index materials. The reflectivity and phase shift of such multilayer mirrors can be calculated by the matrix propagation method described in Kong. With reflections occurring at the material interfaces, there are multiple forward-propagating and backward-propagating in each layer. The beauty of Kong's analysis is to assume a solution form and incorporate all the forward-propagating fields into one amplitude coefficient and all the backward-propagating fields into another amplitude coefficient, rather than keep track of all the secondary, tertiary, etc. reflections in a layer. Electric fields in adjacent layers are governed by the following relation:

$$\begin{bmatrix} A_2 e^{-\imath k_{z,2} d_2} \\ B_2 e^{\imath k_{z,2} d_2} \end{bmatrix} = V_{21} \begin{bmatrix} A_1 e^{-\imath k_{z,1} d_1} \\ B_1 e^{\imath k_{z,1} d_1} \end{bmatrix} \tag{A.1}$$

where A and B are the forward-propagating and backward-propagating tangential electric fields for TE and tangential magnetic fields for TM, respectively. The propagation matrix V_{21} transfers the fields between adjacent layers, and is dependent on wavelength.

$$V_{21}(l) = \frac{1}{2}(1 + p_{21}) \begin{bmatrix} e^{-\imath k_{z,2}(d_2 - d_1)} & R_{21} e^{-\imath k_{z,2}(d_2 - d_1)} \\ R_{21} e^{\imath k_{z,2}(d_2 - d_1)} & e^{\imath k_{z,2}(d_2 - d_1)} \end{bmatrix} \tag{A.2}$$

Here, d_1 and d_2 are the thicknesses of Layer 1 and Layer 2. The other variables are defined as follows:

$$k_{z,m} = \frac{2\pi n_m}{\lambda} \cos\theta \tag{A.3}$$

$$R_{21} = \frac{1 - p_{21}}{1 + p_{21}} \tag{A.4}$$

The normal component of the wavenumber k_z is dependent on the angle of incident θ and the index of refraction n. The Fresnel reflection coefficient R_{21} depends on the material properties of the adjacent layers, and changes for non-normal angles of incidence.

For TE, it is

$$p_{21,\mathrm{TE}} = \frac{\mu_2 k_{z,1}}{\mu_1 k_{z,2}} \tag{A.5}$$

For TM, it is

$$p_{21,\mathrm{TM}} = \frac{\varepsilon_2 k_{z,1}}{\varepsilon_1 k_{z,2}} \tag{A.6}$$

For normal incidence, $p_{21} = n_1/n_2$.

For a structure with multiple layers, such as our mirrors, one can determine the total effect the structure has on incident light by propagating the V matrix all the way through the structure, from the air to the substrate. The propagation matrix is given by

$$V_{total} = \prod V_{lm} \tag{A.7}$$

The total effective propagation matrix V_{total} of the structure then yields the complex reflection coefficient of the whole multilayer structure, given by

$$r_{mirror}\, e^{-i\Phi} = -\frac{V_{total}(2,1)}{V_{total}(2,2)} \tag{A.8}$$

The reflectivity is the amplitude squared of the field coefficient r_{mirror}. And the phase shift is given by Φ. The group delay dispersion introduced by the mirror can then be calculated from the phase shift by

$$GDD = -\frac{\partial^2 \Phi}{\partial^2 \omega} \tag{A.9}$$

REFERENCES

1. J. A. Kong, *Electromagnetic Wave Theory*, EMW Publishing (2000).

APPENDIX B

MIRROR DESIGN CODE

Copies of the key Matlab functions in the mirror design code package are attached here. Functions and their purpose are summarized below. Typing 'help <name of function>' in the Matlab command window will also display the necessary syntax for the input variables, and what is calculated for the output.

Matlab m-files and functions

Main.m	Used as the root program to run the reflectivity and group delay calculations. Plotting commands and chart manipulations are performed here as well. This is not a function.
R971.m	The R***.m files, in general, contain mirror structures, as designated by their growth numbers in the LAK lab. They perform the matrix analysis required to generate reflectivity as a function of wavelength. They also output the phase of the reflected light. These functions are called by Main.m. This particular file shows a standard SBR mirror structure.
Rnew_HMS3b.m	See above above. This particular file shows a resonantly-coated SBR mirror structure
CalcGDD.m	Calculates the group delay dispersion given inputs of wavelength and phase, using numerical differentials.
GenV.m	The basic building block for the matrix analysis used to calculate the reflectivity and phase profiles of the SBRs. Called by the R***.m files.
n_InGaAs.m	This and other n_***.m files provide the Sellmeier equation-based refractive indices for the relevant III-V material systems. n_AlGaAs.m and n_InGaAsP.m are similar functions. Later generations of the R***.m files used empirical data on material refractive indices, provided by Gale Petrich. These are referred to in the code lines with *.mat.
FieldProfile_SBR.m	Generates the square of the electric field standing wave pattern for a given structure. Cannot directly transfer code from the R***.m to here, primarily due to the graphical nature of the output.

```
%MAIN  Plot reflection spectrum of the TE, TM, and combined mode
%components.
%   MAIN is the controller program of the Mirror Code package.  It can plot the
%   reflection spectrum of the TE, TM and combined mode components of the called
%   mirror structure.
%
%   In addition, it can also generate the respective phase, or dispersion, of the
%   mirror.
%
%   Functions called:
%      R*
%      CalcGDD
%
%   HMS '03
%   @Mirror Code


lambda = 1.200 : 0.0025 : 1.900;        % wavelengths in micron (for Cr:YAG)
%lambda = 0.850 : 0.001 : 2.000;        % wavelengths in micron (for Cr:forsterite)
%lambda = 0.550 : 0.001 : 1.100;        % wavelengths in micron (for Ti:Sapphire)
n_max = length(lambda);

theta = 0;                          % angle of incidence, degrees (FTIR 35 degrees)
theta = theta*pi/180;               % convert to radians

R_TE = Rnew_HMS4b(lambda,theta,1);                  % reflection for TE mode
%R_TM = Rnew_HMS4b(lambda,theta,2);                 % reflection for TM mode

%R_TE2 = Rnew_HMS4b(lambda,theta,1);                % reflection for TE mode
%R_TM2 = Rnew_HMS4b(lambda,theta,2);                % reflection for TM mode


%Reflectivity and Phase Calculations (recall R is a complex number)
Rmag_TE = (abs(R_TE)).^2;                           % reflectivity
Rphase_TE = unwrap(angle(R_TE));                    % phase

%Rmag_TM = (abs(R_TM)).^2;
%Rphase_TM = unwrap(angle(R_TM));

%Rtotal = Rmag_TM + Rmag_TE;

%Rmag_TE2 = (abs(R_TE2)).^2;                        % reflectivity
%Rmag_TM2 = (abs(R_TM2)).^2;
%Rphase_TM2 = unwrap(angle(R_TM2));
%Rtotal2 = Rmag_TM2 + Rmag_TE2;

rGDD_TM = CalcGDD(lambda,Rphase_TM);
%rGDD_TM2 = CalcGDD(lambda,Rphase_TM2);

%Generate plots

figure;
hold on;
plot(lambda,Rmag_TE,'r','LineWidth',[3.0]);
% plot(lambda,Rmag_TE2,'b','LineWidth',[3.0]);
% plot(lambda,Rmag_TM,lambda,temp,'b');
% plot(lambda,Rtotal/2,'r','LineWidth',[2.0]);
% plot(lambda,Rtotal/2,'r',lambda,temp,'LineWidth',[2.0]);
% axis([lambda(1) lambda(n_max) 0 1.05]);
axis([1.45 1.65 0 1.00]);
xlabel('Incident Wavelength (\mum)');
ylabel('Reflectivity')
% title('R1000 Oxidized - Design, FTIR Simulation');
```

```
title('Reflectivity vs. Wavelength, R_n_e_w HMS3, Normal Incidence');
% legend('TE + TM Theory w/ Loss','TE + TM Theory w/o Loss','R970a');
% legend('Design','R971a','R971c');
% legend('Design','Measurement');
% legend('HMS1','HMS2');
grid on;
% hold off;

figure;
hold on;
plot(lambda,rGDD_TE,lambda,rGDD_TM,'r');
%plot(lambda,rGDD_TM,'r','LineWidth',[3.0]);
%plot(lambda,rGDD_TM2,'b','LineWidth',[2.0]);
%axis([lambda(1) lambda(n_max) -5000 5000]);
axis([1.45 1.65 -2000 2000]);
xlabel('Incident Wavelength (\mum)');
ylabel('GDD (fs^2)');
title('Group Delay Dispersion Profile, HMS_n_e_w, Normal Incidence');
%legend('HMS3','HMS4');
grid on;
%hold off;
```

```
function  R = R971(lambda,theta,mode)

%R971  Complex reflection coefficient of the unoxidized R970 mirror structure.
%  R = R971(LAMBDA,THETA,MODE) calculates the complex reflection coefficient R of
%  the R971 mirror structure designed for Cr:YAG, for a particular range of
%  wavelengths LAMBDA, angle of incidence THETA (relative to normal), and MODE
%  (either TE or TM).
%
%  The reflectivity R^2 and the associated phase can then be extracted from the
%  output R.
%
%     Mode = 1 ----------> TE
%     Mode = 2 ----------> TM
%
%  SBR structure:   109 nm InP / 10 nm InGaAs / 109 nm InP         Quantum Well
%                   7x  111 nm AlGaAs / 240*(0.90) nm AlxOy        Mirror
%                   111 nm AlGaAs
%                   GaAs                                          Substrate
%
%
%  Functions called:
%            GenV
%            n_InGaAsP
%            n_InGaAs
%            n_AlGaAs
%
%  HMS '03
%  $Orig: 11/17/2003
%  @Mirror Code

num = length(lambda);                                  % number of data points

c = 0.90;          % AlAs-to-AlxOy contraction (10% or 0.90 originally) ****

%Initialize variables
R = zeros(1,num);                                % reflection coefficient
V = zeros(2,2);                                  % propagation matrix
V1 = zeros(2,2);                                 % temporary holders, scaffolding
V2 = zeros(2,2);
V3 = zeros(2,2);

%Define constants for reflectivity problem
n0 = 1;                                  % index of incident medium (air)
N = 7;                                   % number of layer pairs in the mirror

%Calculate reflection coefficient R
for m = 1 : num                          % cycle through for each wavelength

    k0 = 2*pi*n0/lambda(m);              % wavenumber in air/vacuum
    kx = k0*sin(theta);    % transverse component constant due to phase-matching

    %First the GaAs/InGaAs/GaAs QW
    n1 = n_InGaAsP(0,0,lambda(m));       % InP
    %n2 = 3.6;                           % Turn off loss
    n2 = n_InGaAs(0.5,lambda(m));        % InGaAs
    n3 = n1;                             % InP

    d1 = 0.109;                          % in um
    d2 = 0.010;
    d3 = 0.109;

    V1 = GenV(n0,n1,0,d1,k0,kx,mode);          % manually do the quantum well
    V2 = GenV(n1,n2,d1,d1+d2,k0,kx,mode);
```

```
        V3 = GenV(n2,n3,d1+d2,d1+d2+d3,k0,kx,mode);

        V = V3*V2*V1;

        %Now do the mirror
        nh = n_AlGaAs(0.3,lambda(m));     % high-index AlGaAs layer
        %nl = 1.66;                       % low-index AlxOy layer at 1.5 um ****
        nl = 1.66;
        ns = n_AlGaAs(0.0,lambda(m));     % GaAs substrate
        dh = 0.111;
        dl = 0.240*c;

        %Note to self: I start cheating with the depths here.
        %Remember it's only the difference in d that matters. Future fix.

        V1 = GenV(n3,nh,0,dh,k0,kx,mode);       % manually do the first layer pair
        V2 = GenV(nh,nl,dh,dh+dl,k0,kx,mode);

        V = V2*V1*V;

        for n = 1 : (N-1)

               V1 = GenV(nl,nh,dl,dl+dh,k0,kx,mode);
               V2 = GenV(nh,nl,dh,dl+dh,k0,kx,mode);

               V = V2*V1*V;

        end

        V1 = GenV(nl,nh,dl,dl+dh,k0,kx,mode);   % into last AlGaAs layer

        V2 = GenV(nh,ns,d1+d2+d3+N*(dh+dl)+dh,0,k0,kx,mode); % into substrate

        Vtotal = V2*V1*V;

        R(m) = -Vtotal(1,2)/Vtotal(1,1);        % reflection coefficient

end
```

```
function  R = Rnew_HMS3b(lambda,theta,mode)

%RNEW_HMS3B  Complex reflection coefficient of the resonantly coated VA88 structure.
%  R = RNEW_HMS3B(LAMBDA,THETA,MODE) calculates the complex reflection coefficient
%  R of the VA88 mirror structure designed for 1.5 um operation, for a particular
%  range of wavelengths LAMBDA, angle of incidence THETA (relative to normal), and
%  MODE (either TE or TM).
%
%  The reflectivity R^2 and the associated phase can then be extracted from the
%  output R.
%
%      Mode = 1 ----------> TE
%      Mode = 2 ----------> TM
%
%  Designed for lambda_c = 1550 nm
%
%  Functions called:
%             GenV
%             n_InGaAs
%             n_AlGaAs
%
%  HMS '03
%  $Orig: 07/26/2008
%  @Mirror Code

num = length(lambda);                    % number of data points

load InGaAsData.mat;                     % Gale empirical refractive indices
load GaAsData.mat;

%lambda = lambda_GaAs;                   % already done in Main.m


%Initialize variables
R = zeros(1,num);                        % reflection coefficient
V = zeros(2,2);                          % propagation matrix
V1 = zeros(2,2);                         % temporary holders, scaffolding
V2 = zeros(2,2);
V3 = zeros(2,2);

%Define constants for reflectivity problem
n0 = 1;                                  % index of incident medium (air)
N = 22;                                  % number of layer pairs in the mirror
N_res = 5;                         % number of resonant layer pairs on top of mirror

%Calculate reflection coefficient R
for m = 1 : num                          % cycle through for each wavelength

    k0 = 2*pi*n0/lambda(m);              % wavenumber in air/vacuum
    kx = k0*sin(theta);                  % transverse component constant due to
                                         % phase-matching

      %First0 the resonant layers - GaAs/AlGaAs
      nl_res0 = n_AlGaAs(0.50,lambda(m));      % higher Al content AlGaAs cap layer
      nl_res = n_AlGaAs(0.95,lambda(m));       % low-index AlGaAs layer
      nh_res = nr_GaAs(m);
       %nh_res = n_AlGaAs(0.0,lambda(m));       % high-index GaAs layer
      dl_res0 = 0.1239;                        % in um
      dl_res = 0.1329;
      dh_res = 0.1147;

%     V1 = GenV(n0,nh_res,0,dh_res,k0,kx,mode);% manually do the first layer pair
%     V2 = GenV(nh_res,nl_res,dh_res,dh_res+dl_res,k0,kx,mode);
```

```
        V1 = GenV(n0,nl_res0,0,dl_res0,k0,kx,mode);% manually do the first layer pair
        V2 = GenV(nl_res0,nh_res,0,dh_res,k0,kx,mode);

        V = V2*V1;

        for n = 1 : (N_res-1)

                V1 = GenV(nh_res,nl_res,dh_res,dl_res+dh_res,k0,kx,mode);
                V2 = GenV(nl_res,nh_res,dl_res,dl_res+dh_res,k0,kx,mode);

                V = V2*V1*V;

        end

    %First the GaAs/InGaAs/GaAs QW
    n1 = nr_GaAs(m);
    %n1 = n_AlGaAs(0.0,lambda(m));                % GaAs
    n2 = nr_InGaAs(m) + i*ni_InGaAs(m);          % n2 = nr_InGaAs(m);
    %n2 = n_InGaAs(0.537,lambda(m));             % InGaAs
    %n2 = real(n_InGaAs(0.537,lambda(m)));       % use to turn off absorption loss
    n3 = n1;                                     % GaAs

%   d1 = 0.1095;                                 % in um
%   d2 = 0.010;
%   d3 = 0.1095;

    d1 = 0.0832;                                 % in um
    d2 = 0.060;
    d3 = 0.0832;

%   d1 = 0.1042;                                 % in um
%   d2 = 0.020;
%   d3 = 0.1042;

        V1 = GenV(nh_res,n1,0,d1,k0,kx,mode);    % manually do the quantum well (n_low
                                                 % of resonant coating to n1)
        V2 = GenV(n1,n2,0,d2,k0,kx,mode);
        V3 = GenV(n2,n3,0,d3,k0,kx,mode);

        V = V3*V2*V1*V;

        %Now do the mirror
        nh = nr_GaAs(m);
        %nh = n_AlGaAs(0.0,lambda(m));           % high-index GaAs layer
        nl = n_AlGaAs(0.95,lambda(m));           % low-index AlGaAs layer
        ns = nr_GaAs(m);
        %ns = n_AlGaAs(0.0,lambda(m));           % GaAs substrate
        dh = 0.1147;                             % in um
        dl = 0.1329;

        %Note to self: I start cheating with the depths here.
        %Remember it's only the difference in d that matters. Future fix.

        V1 = GenV(n3,nh,0,dh,k0,kx,mode);        % manually do the first layer pair
        V2 = GenV(nh,nl,0,dl,k0,kx,mode);

        V = V2*V1*V;

        for n = 1 : (N-1)

                V1 = GenV(nl,nh,0,dh,k0,kx,mode);
                V2 = GenV(nh,nl,0,dl,k0,kx,mode);
```

```
            V = V2*V1*V;

        end

        V1 = GenV(nl,ns,dl_res0+dh_res+(N_res-
1)*(dh_res+dl_res)+d1+d2+d3+N*(dh+dl),0,k0,kx,mode); % into substrate

        Vtotal = V1*V;

        R(m) = -Vtotal(1,2)/Vtotal(1,1);              % reflection coefficient

end
```

```
function  rGDD = CalcGDD(lambda,phase)

%CALCGDD  Group delay dispersion, given the wavelength and phase.
%  RGDD = CALCGDD(LAMBDA,PHASE) calculates the reflected group delay dispersion
%  RGDD given the wavelength LAMBDA and the corresponding phase delay PHASE.  Note
%  that the physics convention is used here.  That is, the exponential in a field
%  is i(k*x - w*t).
%
%  GDD = d2(Phase)/dw2 = function below of d2(Phase)/dLambda2 and d(Phase)/dLambda
%
%
%  HMS '03
%  $Orig: 10/20/2003
%  @Mirror Code


n_max = length(lambda);
dlambda = lambda(2) - lambda(1);
c = 0.30;     % speed of light, in units of um/fs

dphase_dlambda = diff(phase)/dlambda;                % in units of rad/um
dphase_dlambda(n_max) = dphase_dlambda(n_max-1);

d2phase_dlambda2 = diff(dphase_dlambda)/dlambda;     % in units of rad/um^2
d2phase_dlambda2(n_max) = d2phase_dlambda2(n_max-1);

rGDD = (lambda.^3).*dphase_dlambda/(2*pi^2*c^2) + ...       % in units of fs^2
          (lambda.^4).*d2phase_dlambda2/(4*pi^2*c^2);
```

```
function  V = GenV(n1,n2,d1,d2,k0,kx,mode)

%GENV  Forward propagation matrix for TE or TM mode.
%  V = GENV_TE(N1,N2,D1,D2,K0,KX,MODE) generates the propagation matrix V from
%  Region 1 to Region 2, whose refractive indices are given by inputs N1 and N2.
%  The inputs D1 and D2 bound the region of interest, whose thickness is the
%  quarter wavelength of the center wavelength for which the mirror was designed
%  (1500 nm default).
%
%  Source:  J.A. Kong Electromagnetic Wave Theory, Chapter 3 Section 4.
%
%  HMS '03
%  $Orig: 10/11/2000
%  $Mod:  04/25/2003
%  @Mirror Code


V = zeros(2,2);

kz1 = sqrt((k0*n1)^2 - kx^2);
kz2 = sqrt((k0*n2)^2 - kx^2);

if mode == 1                                        % TE mode

      p21 = kz1/kz2;
      R21 = (1-p21)/(1+p21);                        % Fresnel reflection coefficient

      V(1,1) = exp(-i*kz2*(d2-d1));                 % fill in propagation matrix
      V(1,2) = R21 * exp(-i*kz2*(d2-d1));
      V(2,1) = R21 * exp(+i*kz2*(d2-d1));
      V(2,2) = exp(+i*kz2*(d2-d1));

      V = (1/2)*(1+p21)*V;

else                                                % TM mode

      p21 = ( (n2^2)*kz1 ) / ( (n1^2)*kz2 );
      R21 = (1-p21)/(1+p21);                        % Fresnel reflection coefficient

      V(1,1) = exp(-i*kz2*(d2-d1));                 % fill in propagation matrix
      V(1,2) = R21 * exp(-i*kz2*(d2-d1));
      V(2,1) = R21 * exp(+i*kz2*(d2-d1));
      V(2,2) = exp(+i*kz2*(d2-d1));

      V = (1/2)*(1+p21)*V;

end
```

```
function  n = n_InGaAs(x,rlambda)

%N_INGAAS  Index of refraction as a function of wavelength for InGaAs.
%  N = N_INGAAS(X,RLAMBDA) calculates the complex index of refraction N given the
%  wavelength RLAMBDA and composition X.
%
%      In(x)Ga(1-x)As:
%      --------------
%      x=1 for InAs
%      x=0 for GaAs
%
%  RLAMBDA in micron.
%
%  Source:  Multilayer program files
%
%  HMS '03
%  $Orig: 10/03/2003
%  @Mirror Code


eo = 3.65 - 2.15*x;
ed = 36.1 - 19.9*x;
eg = 1.425 - 1.337*x + 0.27*x^2;
lamg = 1.24/eg;
eta = pi*ed / (2*eo^3*(eo^2 - eg^2));
ef = sqrt(2*eo^2 - eg^2);
m1 = (ef^4 - eg^4)*eta/(2*pi);
m3 = (ef^2 - eg^2)*eta/pi;

n = sqrt(1 + m1 + m3*(1.2398/rlambda)^2 + ...
    eta/pi*(1.2398/rlambda)^4*log((ef^2-(1.2398/rlambda)^2)/(eg^2-
(1.2398/rlambda)^2)));
```

```
function  [z,I,z_index,index] = FieldProfile_Rnew_HMS3(flambda)

%FIELDPROFILE_RNEW_HMS3  Field intensity profile for VA88 mirror structure.
%  [Z,E,Z_INDEX,INDEX] = FIELDPROFILE_RNEW_HMS3(FLAMBDA) calculates the field
%  "intensity" I as a function of depth into the mirror Z for cw wavelengths LAMBDA,
%  as specified by the input.
%
%  Note that I is merely |E(z)|^2, hence it is not properly normalized and cannot
%  be called the intensity.
%
%  FIELDPROFILE_RNEW_HMS1 graphs the field intensity profile I and the index map
%  INDEX as a function of depth Z.
%
%
%
%  Functions called:
%            GenV
%            n_InGaAs
%            n_AlGaAs
%
%  HMS '03
%  $Orig: 05/26/2008
%  @Mirror Code


%flambda = [1.5 1.55 1.6];              % cw wavelengths for field profiles ****
flambda = 1.55;
fnum = length(flambda);

n0 = 1;
theta = 0;

%Mirror structure design
dl_res = 0.1329;                                                              %
in um
dh_res = 0.1147;
d1 = 0.200;
d2 = 0.060;
d3 = 0.415;
dh = 0.1147;
dl = 0.1329;


%Initialize field information matrices
znum = 100000;                          % number of field profile data points
z_min = 1.000;                          % minimum position for profile (um)
z_max = -(3*(dh_res+dl_res)+d1+d2+d3+7*(dl+dh));% maximum position for profile (um)
z = z_min : (z_max-z_min)/(znum-1) : z_max;

%Mirror is calculated all the way through, because we need the overall reflection
%coefficients.  However, the 'z' variable is used to plot the field profile, so it
%doesn't have to be all the way through the mirror.

A = zeros(znum,fnum);                           % backward propagating E-field
B = zeros(znum,fnum);                           % forward propagating E-field
E = zeros(znum,fnum);                           % total E-field

d = zeros(54,1);                                % boundary depths
d(1) = 0;
d(2) = d(1)-dl_res;
d(3) = d(2)-dh_res;
d(4) = d(3)-dl_res;
d(5) = d(4)-dh_res;
```

```
d(6) = d(5)-dl_res;
d(7) = d(6)-dh_res;
d(8) = d(7)-dl;
d(9) = d(8)-d2;
d(10) = d(9)-d3;
d(11) = d(10)-dh;
d(12) = d(11)-dl;
d(13) = d(12)-dh;
d(14) = d(13)-dl;
d(15) = d(14)-dh;
d(16) = d(15)-dl;
d(17) = d(16)-dh;
d(18) = d(17)-dl;
d(19) = d(18)-dh;
d(20) = d(19)-dl;
d(21) = d(20)-dh;
d(22) = d(21)-dl;
d(23) = d(22)-dh;
d(24) = d(23)-dl;
d(25) = d(24)-dh;
d(26) = d(25)-dl;
d(27) = d(26)-dh;
d(28) = d(27)-dl;
d(29) = d(28)-dh;
d(30) = d(29)-dl;
d(31) = d(30)-dh;
d(32) = d(31)-dl;
d(33) = d(32)-dh;
d(34) = d(33)-dl;
d(35) = d(34)-dh;
d(36) = d(35)-dl;
d(37) = d(36)-dh;
d(38) = d(37)-dl;
d(39) = d(38)-dh;
d(40) = d(39)-dl;
d(41) = d(40)-dh;
d(42) = d(41)-dl;
d(43) = d(42)-dh;
d(44) = d(43)-dl;
d(45) = d(44)-dh;
d(46) = d(45)-dl;
d(47) = d(46)-dh;
d(48) = d(47)-dl;
d(49) = d(48)-dh;
d(50) = d(49)-dl;
d(51) = d(50)-dh;
d(52) = d(51)-dl;
d(53) = d(52)-dh;
d(54) = d(53)-dl;


for l = 1 : fnum                          % cycle through each field wavelength

       k0 = 2*pi*n0/flambda(l);           % spatial frequency
       kx = k0*sin(theta);                % transverse beta component

      %Define indices of refraction of layers
       nl_res = n_AlGaAs(0.95,flambda(l)); % low-index AlGaAs resonant coating layer
       nh_res = n_AlGaAs(0.0,flambda(l));  % high-index GaAs resonant coating layer
        n1 = n_AlGaAs(0.0,flambda(l));      % GaAs
       n2 = n_InGaAs(0.537,flambda(l));    % InGaAs - turn on loss
       %n2 = real(n_InGaAs(0.537,flambda(l)));       % InGaAs - turn off loss
       n3 = n1;                                      % GaAs
```

```
nh = n_AlGaAs(0.0,flambda(1));                    % high-index GaAs layer
nl = n_AlGaAs(0.95,flambda(1));                   % low-index AlGaAs layer
ns = n_AlGaAs(0.0,flambda(1));                    % GaAs substrate

V10 = GenV(n0,nl_res,0,dl_res,k0,kx,1);
V20 = GenV(nl_res,nh_res,0,dh_res,k0,kx,1)*V10;
V30 = GenV(nh_res,nl_res,0,dl_res,k0,kx,1)*V20;
V40 = GenV(nl_res,nh_res,0,dh_res,k0,kx,1)*V30;
V50 = GenV(nh_res,nl_res,0,dl_res,k0,kx,1)*V40;
V60 = GenV(nl_res,nh_res,0,dh_res,k0,kx,1)*V50;

V70 = GenV(nh_res,n1,0,d1,k0,kx,1)*V60;
V80 = GenV(n1,n2,0,d2,k0,kx,1)*V70;
V90 = GenV(n2,n3,0,d3,k0,kx,1)*V80;

V100 = GenV(n3,nh,0,dh,k0,kx,1)*V90;
V110 = GenV(nh,nl,0,dl,k0,kx,1)*V100;
V120 = GenV(nl,nh,0,dh,k0,kx,1)*V110;
V130 = GenV(nh,nl,0,dl,k0,kx,1)*V120;
V140 = GenV(nl,nh,0,dh,k0,kx,1)*V130;
V150 = GenV(nh,nl,0,dl,k0,kx,1)*V140;
V160 = GenV(nl,nh,0,dh,k0,kx,1)*V150;
V170 = GenV(nh,nl,0,dl,k0,kx,1)*V160;
V180 = GenV(nl,nh,0,dh,k0,kx,1)*V170;
V190 = GenV(nh,nl,0,dl,k0,kx,1)*V180;
V200 = GenV(nl,nh,0,dh,k0,kx,1)*V190;
V210 = GenV(nh,nl,0,dl,k0,kx,1)*V200;
V220 = GenV(nl,nh,0,dh,k0,kx,1)*V210;
V230 = GenV(nh,nl,0,dl,k0,kx,1)*V220;

V240 = GenV(nl,nh,0,dh,k0,kx,1)*V230;
V250 = GenV(nh,nl,0,dl,k0,kx,1)*V240;
V260 = GenV(nl,nh,0,dh,k0,kx,1)*V250;
V270 = GenV(nh,nl,0,dl,k0,kx,1)*V260;
V280 = GenV(nl,nh,0,dh,k0,kx,1)*V270;
V290 = GenV(nh,nl,0,dl,k0,kx,1)*V280;
V300 = GenV(nl,nh,0,dh,k0,kx,1)*V290;
V310 = GenV(nh,nl,0,dl,k0,kx,1)*V300;
V320 = GenV(nl,nh,0,dh,k0,kx,1)*V310;
V330 = GenV(nh,nl,0,dl,k0,kx,1)*V320;
V340 = GenV(nl,nh,0,dh,k0,kx,1)*V330;
V350 = GenV(nh,nl,0,dl,k0,kx,1)*V340;
V360 = GenV(nl,nh,0,dh,k0,kx,1)*V350;
V370 = GenV(nh,nl,0,dl,k0,kx,1)*V360;

V380 = GenV(nl,nh,0,dh,k0,kx,1)*V370;
V390 = GenV(nh,nl,0,dl,k0,kx,1)*V380;
V400 = GenV(nl,nh,0,dh,k0,kx,1)*V390;
V410 = GenV(nh,nl,0,dl,k0,kx,1)*V400;
V420 = GenV(nl,nh,0,dh,k0,kx,1)*V410;
V430 = GenV(nh,nl,0,dl,k0,kx,1)*V420;
V440 = GenV(nl,nh,0,dh,k0,kx,1)*V430;
V450 = GenV(nh,nl,0,dl,k0,kx,1)*V440;
V460 = GenV(nl,nh,0,dh,k0,kx,1)*V450;
V470 = GenV(nh,nl,0,dl,k0,kx,1)*V460;
V480 = GenV(nl,nh,0,dh,k0,kx,1)*V470;
V490 = GenV(nh,nl,0,dl,k0,kx,1)*V480;
V500 = GenV(nl,nh,0,dh,k0,kx,1)*V490;
V510 = GenV(nh,nl,0,dl,k0,kx,1)*V500;
V520 = GenV(nl,nh,0,dh,k0,kx,1)*V510;
V530 = GenV(nh,nl,0,dl,k0,kx,1)*V520;

V540 = GenV(nl,ns,3*(dh_res+dl_res)+d1+d2+d3+22*(dl+dh),0,k0,kx,1)*V530;
```

```
R(1) = -V540(1,2)/V540(1,1);                    % reflection coefficient

for m = 1 : znum

      if z(m)>=0          % run through the cases (can go as deep as wanted)

            A(m,1) = R(1)*exp(+i*k0*z(m));
            B(m,1) = exp(-i*k0*z(m));          % input amplitude = 1

      elseif (z(m)<d(1)) & (z(m)>=d(2))

            % Recall sign convention in GenV, d is the absolute depth
            V = GenV(n0,nl_res,-d(1),-z(m),k0,kx,1);
            A(m,1) = (R(1)*V(1,1) + V(1,2));
            B(m,1) = (R(1)*V(2,1) + V(2,2));

      elseif (z(m)<d(2)) & (z(m)>=d(3))

            V = GenV(nl_res,nh_res,-d(2),-z(m),k0,kx,1)*V10;
            A(m,1) = (R(1)*V(1,1) + V(1,2));
            B(m,1) = (R(1)*V(2,1) + V(2,2));

      elseif (z(m)<d(3)) & (z(m)>=d(4))

            V = GenV(nh_res,nl_res,-d(3),-z(m),k0,kx,1)*V20;
            A(m,1) = (R(1)*V(1,1) + V(1,2));
            B(m,1) = (R(1)*V(2,1) + V(2,2));

      elseif (z(m)<d(4)) & (z(m)>=d(5))

            V = GenV(nl_res,nh_res,-d(4),-z(m),k0,kx,1)*V30;
            A(m,1) = (R(1)*V(1,1) + V(1,2));
            B(m,1) = (R(1)*V(2,1) + V(2,2));

      elseif (z(m)<d(5)) & (z(m)>=d(6))

            V = GenV(nh_res,nl_res,-d(5),-z(m),k0,kx,1)*V40;
            A(m,1) = (R(1)*V(1,1) + V(1,2));
            B(m,1) = (R(1)*V(2,1) + V(2,2));

      elseif (z(m)<d(6)) & (z(m)>=d(7))

            V = GenV(nl_res,nh_res,-d(6),-z(m),k0,kx,1)*V50;
            A(m,1) = (R(1)*V(1,1) + V(1,2));
            B(m,1) = (R(1)*V(2,1) + V(2,2));

      elseif (z(m)<d(7)) & (z(m)>=d(8))

            V = GenV(nh_res,n1,-d(7),-z(m),k0,kx,1)*V60;
            A(m,1) = (R(1)*V(1,1) + V(1,2));
            B(m,1) = (R(1)*V(2,1) + V(2,2));

      elseif (z(m)<d(8)) & (z(m)>=d(9))

            V = GenV(n1,n2,-d(8),-z(m),k0,kx,1)*V70;
            A(m,1) = (R(1)*V(1,1) + V(1,2));
            B(m,1) = (R(1)*V(2,1) + V(2,2));

      elseif (z(m)<d(9)) & (z(m)>=d(10))

            V = GenV(n2,n3,-d(9),-z(m),k0,kx,1)*V80;
```

```
        A(m,1) = (R(1)*V(1,1) + V(1,2));
        B(m,1) = (R(1)*V(2,1) + V(2,2));

elseif (z(m)<d(10)) & (z(m)>=d(11))

        V = GenV(n3,nh,-d(10),-z(m),k0,kx,1)*V90;
        A(m,1) = (R(1)*V(1,1) + V(1,2));
        B(m,1) = (R(1)*V(2,1) + V(2,2));

elseif (z(m)<d(11)) & (z(m)>=d(12))

        V = GenV(nh,nl,-d(11),-z(m),k0,kx,1)*V100;
        A(m,1) = (R(1)*V(1,1) + V(1,2));
        B(m,1) = (R(1)*V(2,1) + V(2,2));

elseif (z(m)<d(12)) & (z(m)>=d(13))

        V = GenV(nl,nh,-d(12),-z(m),k0,kx,1)*V110;
        A(m,1) = (R(1)*V(1,1) + V(1,2));
        B(m,1) = (R(1)*V(2,1) + V(2,2));

elseif (z(m)<d(13)) & (z(m)>=d(14))

        V = GenV(nh,nl,-d(13),-z(m),k0,kx,1)*V120;
        A(m,1) = (R(1)*V(1,1) + V(1,2));
        B(m,1) = (R(1)*V(2,1) + V(2,2));

elseif (z(m)<d(14)) & (z(m)>=d(15))

        V = GenV(nl,nh,-d(14),-z(m),k0,kx,1)*V130;
        A(m,1) = (R(1)*V(1,1) + V(1,2));
        B(m,1) = (R(1)*V(2,1) + V(2,2));

elseif (z(m)<d(15)) & (z(m)>=d(16))

        V = GenV(nh,nl,-d(15),-z(m),k0,kx,1)*V140;
        A(m,1) = (R(1)*V(1,1) + V(1,2));
        B(m,1) = (R(1)*V(2,1) + V(2,2));

elseif (z(m)<d(16)) & (z(m)>=d(17))

        V = GenV(nl,nh,-d(16),-z(m),k0,kx,1)*V150;
        A(m,1) = (R(1)*V(1,1) + V(1,2));
        B(m,1) = (R(1)*V(2,1) + V(2,2));

elseif (z(m)<d(17)) & (z(m)>=d(18))

        V = GenV(nh,nl,-d(17),-z(m),k0,kx,1)*V160;
        A(m,1) = (R(1)*V(1,1) + V(1,2));
        B(m,1) = (R(1)*V(2,1) + V(2,2));

elseif (z(m)<d(18)) & (z(m)>=d(19))

        V = GenV(nl,nh,-d(18),-z(m),k0,kx,1)*V170;
        A(m,1) = (R(1)*V(1,1) + V(1,2));
        B(m,1) = (R(1)*V(2,1) + V(2,2));

elseif (z(m)<d(19)) & (z(m)>=d(20))

        V = GenV(nh,nl,-d(19),-z(m),k0,kx,1)*V180;
        A(m,1) = (R(1)*V(1,1) + V(1,2));
        B(m,1) = (R(1)*V(2,1) + V(2,2));
```

```
            elseif (z(m)<d(20)) & (z(m)>=d(21))

                  V = GenV(nl,nh,-d(20),-z(m),k0,kx,1)*V190;
                  A(m,1) = (R(1)*V(1,1) + V(1,2));
                  B(m,1) = (R(1)*V(2,1) + V(2,2));

            elseif (z(m)<d(21)) & (z(m)>=d(22))

                  V = GenV(nh,nl,-d(21),-z(m),k0,kx,1)*V200;
                  A(m,1) = (R(1)*V(1,1) + V(1,2));
                  B(m,1) = (R(1)*V(2,1) + V(2,2));

            elseif (z(m)<d(22)) & (z(m)>=d(23))

                  V = GenV(nl,nh,-d(22),-z(m),k0,kx,1)*V210;
                  A(m,1) = (R(1)*V(1,1) + V(1,2));
                  B(m,1) = (R(1)*V(2,1) + V(2,2));

            elseif z(m)<d(23)

                  V = GenV(nh,nl,-d(23),-z(m),k0,kx,1)*V220;
                  A(m,1) = (R(1)*V(1,1) + V(1,2));
                  B(m,1) = (R(1)*V(2,1) + V(2,2));

            end                           % end-if

      end                                 % end-for, all z values for a wavelength

end                                       % end-for, all field profile wavelengths


E = A + B;                                      % total field
I = (abs(E)).^2;                                % intensity

z_index = [z_min d(1) d(1) d(1) d(2) d(2) d(2) d(3) d(3) d(3) d(4) d(4) d(4) d(5)...
d(5) d(5) d(6) d(6) d(6) d(7) d(7) d(7) d(8) d(8) d(8) d(9) d(9) d(9) d(10) d(10)...
d(10) d(11) d(11) d(11) d(12) d(12) d(12) d(13) d(13) d(13) d(14) d(14) d(14)...
d(15)  d(15) d(15) d(16) d(16) d(16) d(17) d(17) d(17) d(18) d(18) d(18) d(19)...
d(19) d(19)d(20) d(20) d(20) d(21) d(21) d(21) d(22) d(22) d(22) d(23) d(23)...
d(23) d(24)];

index = [n0 n0 0 nl_res nl_res 0 nh_res nh_res 0 nl_res nl_res 0 nh_res nh_res 0
nl_res nl_res...0 nh_res nh_res 0 nl nl 0 n2 n2 0 n3 n3 0 nh nh 0 nl nl 0 nh nh 0 nl
nl 0 nh nh 0 nl nl...0 nh nh 0 nl nl 0 nh nh 0 nl nl 0 nh nh 0 nl nl 0 nh nh 0 nl
nl];

% just get rid of any absorption effects, makes the plot look nice
index = real(index);

%Plots and formatting
figure;
hold on;
%plot(z,I(:,1),z,I(:,2),z,I(:,3),'LineWidth',2);
plot(z,I(:,1),'LineWidth',2);
plot(z_index,index,'k');
xlabel('Mirror Depth z (\mum)');
ylabel('|E(z)|^2 / Index of Refraction');
title('E-Field Profile in HMS_n_e_w SBR');
%legend('\lambda = 1.50','\lambda = 1.55','\lambda = 1.60');
legend('\lambda = 1.55');
%axis([z_max z_min 0 4.5]);
axis([-1.8 0.8 0 4.5]);
```